universität wien

MASTERARBEIT / MASTER'S THESIS

Titel der Masterarbeit / Title of the Master's Thesis

„Modelling of the optical properties of internally-mixed dust particles“

verfasst von / submitted by

Andreas Gattringer, BSc

angestrebter akademischer Grad / in partial fulfilment of the requirements for the degree of

Master of Science (MSc)

Wien, 2020 / Vienna, 2020

Studienkennzahl lt. Studienblatt / degree programme code as it appears on the student record sheet:	UA 066 876
Studienrichtung lt. Studienblatt / degree programme as it appears on the student record sheet:	Masterstudium Physik UG2002
Betreut von / Supervisor:	Univ.-Prof. Dr. Bernadett Weinzierl

Acknowledgements

I would like to acknowledge the valuable support given to me during the course of my master's degree, and in particular, those who have contributed to the production of this thesis.

Firstly, I would like to thank my supervisors Bernadett Weinzierl and Josef Gasteiger, whose knowledge, patience and availability have been greatly appreciated. Josef's advice and guidance throughout the development of this thesis and his detailed input at every stage is gratefully acknowledged. Bernadett's oversight and guidance to me have likewise been much valued. Moreover, her leadership of the group, has made for a very pleasant climate.

I would also like to thank Stefan Dullinger for not only providing a supportive work environment, but also the computational resources, without which this thesis would not have been possible.

I would express my appreciation of colleagues and fellow students within both the Aerosol Physics and Environmental Physics group and the Department for Botany and Biodiversity Research. Without their encouragement and conversation, undertaking this degree would have not only been more difficult, but also less enjoyable.

Finally, to my wife, Sophy Le Masurier, just two words: thank you.

Abstract

Aerosols have an important effect on Earth's climate, both indirect and direct, i.e. via interaction with solar radiation. Most of the atmospheric aerosol by mass is mineral dust. Simulations of the optical properties of mineral dust often assume spherical, homogeneous particles. This has changed in recent years. In this thesis, the optical properties of heterogeneous mineral dust particles containing iron oxides (haematite and goethite) have been modelled to gain further insight into the internal structure's role on optical properties and to extend the MOPSMAP software package. The optical properties of particles that are mixed homogeneously are compared to particles that have an internal structure. This has been done for multiple particle shapes and refractive indices for one of the two iron oxides for a wide range of particles sizes. Additionally, the effect of the mixture type on the optical properties has been studied for particle ensembles.

For this purpose, heterogeneous particles have been created based on six reference shapes. This was done by partitioning the particle into cubic volumes. Each subvolume was assigned a refractive index based on its material. Inclusions of iron oxides were modelled by replacing multiple sphere-shaped regions of cubic volumes, with a volume each of one percent of the whole particle's volume. Subsequently, the optical properties of the generated particles were calculated using the direct dipole approximation (DDA).

The effect of the inhomogeneous mixture was shown to be clearly visible for all optical properties. Particles with an internal structure showed less absorption, compared to their homogeneously mixed counterparts. For smaller size parameters (i.e. up to size parameters 5–10), the changes in optical property values could not be simply summarized. Absorption efficiency and asymmetry factor showed both change in magnitude and a size-shift for the first maximum. Depending on refractive index their values could be higher or lower. In general, there was a stronger size-dependent variation in optical properties than for homogeneously mixed particles. For larger particles, it was shown that the absorption efficiency could be up to 4–5 times greater than for the homogeneous particle. A skin effect was observed for large ($\gtrsim 15$) size parameters, where the optical property no longer depends on the size parameter. This was shown for the absorption efficiency, single scattering albedo and asymmetry factor. This effect occurred at smaller size parameters for higher imaginary parts of the refractive index.

The effect of the mixture type for particle ensembles was pronounced for the single scattering albedo, asymmetry factor and absorption coefficient, while the internal structure had very little effect on the extinction coefficient. At short wavelengths ($<$ 490 nm) the absorption shown by inhomogeneous particles was weaker by a factor of two, compared to their homogeneous counterparts.

Kurzfassung

Aerosole haben einen wichtigen Effekt auf das Klima der Erde, sowohl indirekt, als auch direkt, durch Interaktion mit der Sonnenstrahlung. Der Großteil der Masse des atmosphärischen Aerosols ist mineralischen Ursprungs. Die Simulation der optischen Eigenschaften von Mineralstaub geht oft von sphärischen, homogenen Teilchen aus. Das hat sich in den letzten Jahren geändert. In dieser Arbeit werden die optischen Eigenschaften von heterogenen Mineralstaubpartikeln, die Eisenoxide (Hämatit und Goethit) enthalten, modelliert, um den Einfluss der internen Strukute auf die optischen Eigenschaften zu untersuchen, und das MOSMAP Softwarepaket zu erweitern. Die optischen Eigenschaften homogen gemischer Teilchen werden mit denen von Teilchen mit interner Struktur verglichen. Das wurde für mehrere Teilchenformen und mehrere Brechungsindizes für eines der beiden Eisenoxide über eine großen Größenbereich durchgeführt. Zusätzlich wurde der Effekt der internen Struktur auf die optischen Eigenschaften auch für Teichenensembles untersucht.

Zu diesem Zweck wurden heterogene Teilchen basierend auf sechs Referenzformen erstellt. Dies wurde durch Unterteilung der Teilchen in kubische Subvolumina erreicht. Jedem Subvolumen wurde ein materialbasierter Brechungsindex zugeteilt. Eisenoxideinlagerungen wurden modelliert, indem mehrere sphärische Region bestehend aus kubischen Volumen, mit einem Volumen von je einem Prozent des Gesamtvolumens, ersetzt wurden. Die optischen Eigenschaften der generierten Teilchen wurden mittels der diskreten Dipolnäherung (discrete dipole approximation, DDA) berechnet.

Es wurde gezeigt, dass der Effekt der inhomogenen Mischung für alle optischen Eigenschaften sichtbar ist. Teilchen mit interner Struktur zeigen, verglichen mit ihren homogen gemischten Gegenstücken, eine geringere Absorption. Für kleinere Größenparameter (bis zu Größenparameter 5–10) können die Änderungen der optischen Eigenschaften nicht einfach zusammengefasst werden. Absorptionseffizienz und Asymmetriefaktor zeigten Änderung in Größe und eine größenabhängige Verlagerung des ersten Maximums. Je nach Brechungsindex können die Werte der Eigenschaften größer oder kleiner sein. Im Allgemeinen war die Veränderung der optischen Eigenschaften stärker von Änderungen der Teilchengröße abhängig, als für homogen gemischte Teilchen. Für größere Teilchen konnte gezeigt werden, dass die Absorptionseffizienz bis um einen Faktor von 4–5 größer als im homogenen Fall sein kann. Für große Teilchen (Größenparameter $\gtrsim$ 15) konnte ein Oberflächeneffekt beobachtet werden, bei dem die optischen Eigenschaften nicht mehr vom Größenparameter abhängig sind. Dieser Effekt trifft für einen höheren Imaginärteil des Brechungsindex bereits bei kleineren Teilchen auf.

Der Effekt des Mischungstypes für Teilchenensembles war für die Einfachstreu-Albdeo, den Asymmetriefaktor und den Absorptionskoeffizienten sichtbar, während die interne Struktur für den Extinktionskoeffizienten einen vernachlässigbaren Effekt hatte. Für

kurze Wellenlängen (<490 nm) ist die Absorption durch Teilchenensembles für inhomogene Teilchen um bis zu einem Faktor zwei schwächer als im homogenen Fall.

Contents

1. Introduction

Aerosols are a suspension of particles in a carrier gas. Atmospheric aerosols have an critical effect on Earth's energy budget. They interact with solar radiation, either directly (aerosol-radiation interactions), or indirectly (aerosol-cloud interactions) [1]. Energy from incoming solar radiation can be removed from the incident beam by aerosol particles. This is known as extinction, which is caused by scattering and absorption. One relevant property of aerosol particles is the single scattering albedo (SSA), the ratio of scattering to extinction. The single scattering albedo is an important property with regards to the aerosol's effect on radiative forcing – the change in Earth's radiative energy budget: a small change in SSA can lead to a change in the radiative forcing's sign. The critical threshold between cooling and heating is between 0.6 and 0.76 [2]. The aerosols' effective radiative forcing magnitude shows large uncertainties [3].

By mass, most of the atmospheric aerosol is mineral dust [4]. Mineral dust aerosol has an important effect on Earth's climate, as it can both scatter and absorb sunlight, influencing the Earth's radiation budget [5, 6]. The exact magnitude of the mineral dust's radiative forcing still shows uncertainties [4, 7].

Analysis of dust particles has shown that such particles are inhomogeneous [8] and these inhomogeneities influence a particle's single scattering albedo [9] and the radiative forcing of dust.

Iron oxides play a significant role in mineral dust's single-scattering properties [10]. Haematite and goethite are the major iron oxides contained in natural dust particles [11].

For the optical modelling of dust, homogeneous spherical dust particles are often assumed, but the use of more realistic non-spherical dust particle shapes has increased in recent years [12–15].

The freely-available MOPSMAP (Modeled optical properties of ensembles of aerosol particles) package [16], which was developed by Josef Gasteiger at the University of Vienna in cooperation with Matthias Wiegner from the Ludwig Maximilian University of Munich, offers the possibility to calculate the optical properties of user-defined mixtures of spheroidal and irregular dust shapes. However, this package is still limited to homogeneous particles. First studies using more realistic inhomogeneous dust particles derived from stereogrammetric scanning-electron microscope images have been performed [17]. However these results often cannot be applied to specific problems (e.g. when a certain size distribution is known). Previous studies of non-spherical particles and particles with internal structure where either based on randomly orientated spheroids [14], spherical particles with spherical inclusions [9] or few realistic particles at different size parameters [11, 17]. In this thesis, a comprehensive set of simplified particles with realistic shapes will be used to study the effect of the internal structure on optical properties across a

wide range of size parameters and inclusion volumes. The goals of this master thesis are

1. the systematic expansion of MOPSMAP to include inhomogeneous dust particles, such that the haematite and goethite fractions as well as the size distribution can be varied, and

2. the analysis of inhomogeneities' influence on the optical properties of dust, compared with homogeneous particles, especially focusing on absorption.

This analysis will allow an estimation of the impact of the inhomogeneities on the radiative effects of dust aerosols and the extended MOPSMAP data set is intended to enable the dust community to apply more realistic dust optical properties in their calculations and models.

It is anticipated that internally-mixed dust particles absorb less than their homogeneous counterparts. Therefore, the consideration of internal mixing in aerosol models should have a considerable effect and will result in more realistic optical properties. An improved dust model will in addition help to achieve consistency between different measurement methods (tested in so-called 'closure studies').

This thesis is structured in 6 parts. Initially an introduction to the theory of the optical properties of aerosol particles is given (Chapter 2). In Chapter 3 the generation of inhomogeneously mixed aerosol particle models and the calculation of the optical properties are described. Finally, the results (Chapter 4) and further steps are discussed (Chapters 5 and 6).

2. Theory

The material found in this chapter can be found in many textbooks. If not noted otherwise the information is summarised from [18–21].

2.1. Aerosols

Aerosols are a suspension of particles – either solid or liquid – in a gas. Atmospheric aerosols are those that occur in earth's atmosphere, either from natural or anthropogenic sources. In this usage the term aerosol refers to the particles themselves, the carrier gas being the atmosphere's air.

Mineral dust is an aerosol created by wind erosion, with an estimated annual atmospheric emission of 500 – 2000 Tg [22, 23]. There are large uncertainties in the optical properties of mineral dust [24]. Mineral dust can be either natural in source, or anthropogenic, where land-use changes and climate modifications contribute to dust particle emissions [20]. It effects earth climate, both directly and indirectly. While the net radiative forcing effect of mineral dust on Earth's atmosphere is assumed to be cooling [25], the magnitude and sign of the effect is uncertain, and might even be warming [4], depending on abundance, size distribution and composition. The composition and chemistry of mineral dust depends on origin and transport processes [26, 27].

2.2. Microphysics of aerosol particles

For optical modelling the relevant attributes of aerosols are shape, size and material. The size is usually expressed in relation to the wavelength of the incident radiation. For non-spherical particles there are several ways to define this size parameter, see Section 2.3.5.

The material defines the refractive index, which is also dependent on the incident radiation's wavelength. Aerosols may be homogeneous in material, but for mineral dust particles, this is often not the case [10].

2.3. Interaction of light with particulate matter

Electro-magnetic radiation propagates as transverse waves. Light is the visible part of the electro-magnetic radiation with wavelengths λ in the range of approximately 400 nm

– 700 nm [19]. When a beam of light passes through a volume with aerosol particles, some of its energy is attenuated, i.e. energy is removed from the beam. This effect is called extinction, for which two mechanisms are responsible: scattering and absorption. The light wave's oscillating electric field excites electric charges in the aerosol's particles into oscillation, which is either re-emitted (scattering) or converted into thermal energy (absorption).

2.3.1. Refractive index

Propagation of electromagnetic waves in a medium can be described using the refractive index $m(\lambda) = n(\lambda) + ik(\lambda)$. The real part n describes the propagation and change of phase velocity $v = \frac{c}{n}$ in the medium. The imaginary part, k, describes the electromagnetic wave's attenuation, i.e. the absorptive properties of the medium. The refractive index of materials, both the real and imaginary part, is dependent on the light's wavelength.

2.3.2. Extinction

Extinction describes the removal of the incident beam's energy. Two mechanisms are responsible for extinction:

Scattering changes the trajectory of incoming radiation by electrical excitement and re-radiation. In the context of this thesis only elastic scattering will be considered, i.e. the frequency of the re-emitted (i.e. scattered) light is the same as that of the incident photon.

Absorption is the conversion of incoming radiation via electric excitement of charges into another form, e.g. thermal energy.

2.3.3. Cross sections, efficiencies and coefficients

Energy is removed from the beam by absorption and scattering by a particle. To quantify these effects the concept of cross sections is needed. We define the absorption and scattering cross-sections C_{abs} and C_{sca}. These correspond to the areas which have to be removed from the beam so that the removed energy is equal to the losses caused by absorption and scattering. The extinction cross-section C_{ext} is the sum of the two:

$$C_{\text{ext}} = C_{\text{abs}} + C_{\text{sca}} \tag{2.1}$$

It is important to note that these cross sections can be larger than the geometric cross section of the particle: a particle can remove more energy from the beam via scattering and absorption, than if only the area corresponding to the particles geometric cross section had been removed from the beam.

The absorption and scattering efficiencies Q_{sca} and Q_{ext} are the respective cross sections divided by the geometric cross section C_{geo} of the particle.

$$Q_{\text{abs}} = C_{\text{abs}}/C_{\text{geo}} \qquad Q_{\text{sca}} = C_{\text{sca}}/C_{\text{geo}} \tag{2.2}$$

They can also be described as the radiant power that is scattered or absorbed divided by the geometrically incident radiant power [19].

A particle's extinction efficiency is the sum of the particle's absorption efficiency and scattering efficiency.

$$Q_{\text{ext}} = Q_{\text{abs}} + Q_{\text{sca}} \tag{2.3}$$

Because the absorption and scattering cross sections can be greater than the geometric cross section, efficiencies can take on values greater than unity. This is reflected in the extinction paradox: for large sizes (size $\gg$ wavelength) the extinction efficiency Q_{ext} approaches 2, i.e. twice as much energy is removed from the incident beam compared to removing an area the size of the particle's geometric cross section [18].

Coefficients

The absorption, scattering and extinction efficiencies are single particle properties. For a volume containing particles with a number concentration of N, i.e. the number of particles divided by that volume, the corresponding coefficients are defined as

$$\sigma_{\text{sca, abs, ext}} = ANQ_{\text{sca, abs, ext}} \tag{2.4}$$

where A is the is the cross-sectional area of the individual particles and Q the corresponding efficiency. Equation (2.4) is only valid for monodisperse aerosols, i.e. an aerosol composed of identical particles. The coefficients of a polydisperse aerosol is the sum of the coefficients of the individual particle species.

Similar to the efficiencies, the extinction coefficient is the sum of the absorption and scattering coefficient:

$$\sigma_{\text{ext}} = \sigma_{\text{abs}} + \sigma_{\text{sca}} \tag{2.5}$$

With the extinction coefficient, the loss of intensity of light passing through a volume containing an aerosol can be calculated using the Beer-Lambert law:

$$I = I_0 \mathrm{e}^{-\sigma_{\text{ext}} L} \tag{2.6}$$

where I_0 is the original intensity, I the resulting intensity and L the travelled length through the aerosol.

2.3.4. Angular distribution of scattered light

Phase function

The phase function $P(\theta)$ describes the scattered light intensity I_{sca} depending on the (zenith) scattering angle θ. The phase function is normalised to unity.

$$P(\theta) = \frac{I_{sca}(\theta)}{\int_0^\pi I_{sca}(\theta) \sin\theta \, \mathrm{d}\theta} \tag{2.7}$$

Asymmetry factor

The asymmetry factor g is defined as the average of the cosine of the scattering angle, weighted by intensity [28].

$$g = \frac{1}{2}\frac{\int_0^\pi \cos\theta I_{sca}(\theta)\sin\theta\,\mathrm{d}\theta}{\int_0^\pi I_{sca}(\theta)\sin\theta\,\mathrm{d}\theta} = \frac{1}{2}\int_0^\pi \cos\theta P(\theta)\sin\theta\,\mathrm{d}\theta \tag{2.8}$$

Where $I_{sca}(\theta)$ is the intensity of the scattered light, θ is the scattering angle and $P(\theta)$ is the phase function, see Equation (2.7). A positive asymmetry factor indicates that more light is scattered in the forward direction, with a maximum of 1 for light that is completely scattered at 0°. A negative value indicates that scattering is more prominent in the back direction with a minimum of -1 for light that is completely scattered at 180°. For isotropic scattering (and scattering that is symmetric around the 90° angle), g equals 0.

2.3.5. Size parameter

The size parameter is used to characterise the size of particle in relation to the wavelength of the incident light:

$$x = \frac{\pi D_p}{\lambda} \tag{2.9}$$

where x is the dimensionless size parameter, D_p is the diameter of the particle and λ is the wavelength of the (monochromatic) incident radiation. This is strictly only true for spherical particles. For non-spherical particles a replacement for the diameter has to be used, e.g. the diameter of a sphere with the same volume or the same averaged geometric cross-section as the non-spherical particle. In this thesis only volume-equivalent size parameters are used.

Different regimes of scattering exist depending on the size parameter: for $x \ll 1$ Rayleigh scattering, for $x \approx 1$ Mie scattering, and for $x \gg 1$ geometrical optics is generally used to describe the scattering process.

In this thesis, particles with size parameters ranging from 0.001 to 30.2, spanning all three scattering regimes, have been used. All calculations have been done using the discrete dipole approximation, solving Maxwell's equations, see Section 2.4.

2.3.6. Absorption and single scattering albedo

Light only gets absorbed by matter for negative values of the refractive index's imaginary part κi. The single scattering albedo (SSA) ω_0 is a measure of how much of the light extinction is due to scattering. It ranges from 0 – extinction solely due to absorption – to 1 – extinction solely through scattering.

$$\omega_0 = \frac{\sigma_{\mathrm{sca}}}{\sigma_{\mathrm{ext}}} = \frac{Q_{\mathrm{sca}}}{Q_{\mathrm{ext}}} = \frac{Q_{\mathrm{ext}} - Q_{\mathrm{abs}}}{Q_{\mathrm{ext}}} \tag{2.10}$$

From this follows that the absorption efficiency Q_{abs} and the absorption coefficient σ_{abs} can be expressed as a function of the SSA ω_0.

$$Q_{abs} = Q_{ext}(1 - \omega_0) \tag{2.11}$$

$$\sigma_{abs} = \sigma_{ext}(1 - \omega_0) \tag{2.12}$$

2.4. Modelling of light-matter interactions

To model light-matter interactions Maxwell's equations need to be solved. For spherical, homogeneous particles, exact solutions for the scattering process, first published by Mie [29], can be derived [18]. For simple shapes analytical solutions exist. This is not the case for arbitrary shapes [30, 31]. The T-matrix method can be used to solve Maxwell's equations for axially symmetric shapes [32–34]. Implementations of the T-matrix methods are available on-line [35].

The scattering of light by arbitrary shapes can be approximated by modelling the scatterer as collection of spatially resolved points, called dipoles [36]. The interaction of these dipoles with the incident field and each other can be described using a system of linear equations [36–38].

To derive the optical properties of a particle using discrete dipole approximation (DDA), the dipole moments P and polarisability α of all dipoles has to be calculated. The polarisability is the coupling factor between induced dipole moment P and incident electric field E.

$$\alpha E = P \tag{2.13}$$

The polarisability is a tensor, but for isotropic media the polarisability is a scalar multiple of the identity matrix [37]. There are different methods to calculate the polarisability tensor, see [38]. The refractive index of a material is related to the polarisability tensor. For this thesis the Filtered Coupled Dipoles (FCD) method, as implemented in ADDA, has been used, as this method offers advantages both in required computational time and accuracy over other DDA formulations [16, 39].

The DDA formulation for the dipole moments as given by [38] is:

$$E_{inc,i} = \bar{\alpha}_i P_i - \sum_{j \neq i} \bar{G}_{ij} P_j \tag{2.14}$$

where i and j are the indices used to enumerate the dipoles, $E_{inc,i}$ is the incident electric field, $\bar{\alpha}_i$ is the polarisability and $\bar{G}_{ij}$ is the interaction term, which describes the electric field's contribution of the j^{th} dipole on the i^{th}. There are multiple methods to solve this system of linear equations [38]. The optical properties, like absorption and scattering, can finally be derived from the dipole polarisations P_i.

3. Methods

This chapter describes how the 3D models of the particles were generated from reference shapes, how the inclusions were modelled and the optical properties were calculated and averaged over different orientations.

To calculate and compare the optical properties of internally mixed dust particles, several steps were necessary:

1. Reference particles were generated based on reference geometries (shapes), see Section 3.3.1.
2. Internally mixed particles were generated by selecting subvolumes and assigning them a different material, see Section 3.3.2.
3. The optical properties of these particles were calculated using ADDA for different spatial orientations, see Section 3.4.
4. The optical properties were averaged over all orientations, see Section 3.5.

3.1. Terminology

Reference shape A surface mesh describing a particle's surface geometry. In this thesis six different reference shapes, A–F from [6], were used. See Figure 3.1.

Reference particle A 3D model of the reference shape, consisting of cubic volume elements arranged on a lattice. For each size parameter ≥ 10.0 an individual reference particle was used. See Figure 3.2.

Internally-mixed particle A 3D model based on a reference particle, where volume elements in (spherical) regions have been marked as having different refractive indices. See Figure 3.3.

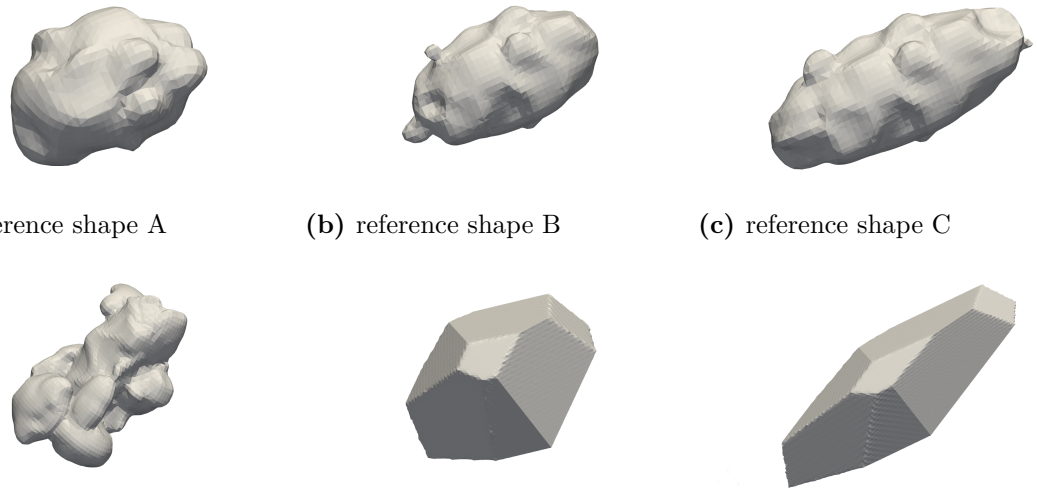

(a) reference shape A **(b)** reference shape B **(c)** reference shape C

(d) reference shape D **(e)** reference shape E **(f)** reference shape F

Figure 3.1: Reference shapes A–F.

3.2. Particle composition

Iron oxides are an important part of mineral dust. They strongly absorb at visible wavelengths [40]. The most common iron oxides in mineral dust by mass are haematite and goethite, with goethite being more abundant [41]. They can be found scattered in small grains throughout the mineral dust particles [10], but also as a surface coatings [42].

In this thesis heterogeneous mineral dust particles with iron oxide inclusions were studied. This was achieved by taking a particle using a base material and inserting spherical inclusions of haematite and goethite. The volumes taken by the iron oxides were varied.

3.2.1. Refractive indices

In the visible spectrum, especially between 460 and 700 nm, the haematite's imaginary part of the refractive index, which is responsible for the absorptive properties, is up to 3 times greater than that of goethite [40]. For visible and larger wavelengths of light the imaginary part of haematite decreases with increasing wavelength [43]. In the visible range, the difference in the refractive indices' imaginary part is largest at smaller wavelengths [44].

There are large uncertainties in the refractive index of haematite [40]. For these reasons two values for the refractive index of haematite were arbitrarily chosen for wavelengths in the visible spectrum [43], while the refractive indices of goethite and the base material were kept fixed.

The particles were composed of three materials: a base material, which is a place-

holder for a non-absorbing material like quartz, inclusions of haematite, for two different refractive indices and additional inclusions of an absorbing material represented by goethite, the refractive index of which was kept constant. For the simulation of particle ensembles the two refractive indices of haematite were interpreted as to belonging to two different wavelengths of light, allowing interpolation over a wider range of wavelengths. See Table 3.1 for details.

Table 3.1. Simulation parameters

Parameter	**Values**
Particle shape	A, B, C, D, E, F
Size parameter x	111 values between 0.001 and 30.2, with a ratio $\frac{x_{i+1}}{x_i} \approx 1.10$ between consecutive values
Inclusions, by percent of volume	
- haematite	0, 2, 6
- goethite	0, 3, 9
Refractive indices m	
- base material	$1.5 + 0.0i$
- haematite	$3.0 + 0.2i$, $3.0 + 1.162i$
- goethite	$2.2 + 0.1i$

3.3. Particle generation

This section describes how the 3D models of the particles were generated for use with ADDA.

Particles were modelled based on six reference shapes, shape A–F from [6]. They were provided as meshes describing the particle's surface. See Figure 3.1.

For each particle shape, particles for all combinations of each three inclusion volumes of haematite and goethite were generated. This was done for multiple size parameters and two different sets of refractive indices for haematite, as it is the dominant iron oxide with respect to absorption [41].

3.3.1. Reference particles

For each shape and size parameter a 3D particle was created for later use with ADDA. The particles consisted of cubic volume elements, called *dipoles* in the ADDA terminology. Each dipole is described by its position on a cubic lattice and its refractive index. The particles can be thought of as an arrangement of small, equally sized cubes on such an integer lattice. A reference particle is the blueprint for the dust particle we want to create. The reference particles created differed only in shape (six shapes, A-F) and size parameter. Each particle was created such that the number of dipoles per wavelength λ is at least 11. The number of dipoles per wavelength increases the simulation accuracy,

but also computation time, so the value of 11 was taken following recommendations of [31, 38]. For a wavelength $\lambda = 550\,\text{nm}$ this corresponds to a spatial resolution (dipole side length) of (at maximum) 50 nm. For particles of size parameter < 10 (which at 550 nm corresponds to a particle of diameter $d \approx 1750\,\text{nm}$) the generated reference particle for size parameter 10 was used and scaled to the correct size in ADDA, resulting in a resolution higher than 11 dipoles per wavelength.

The conversion from reference shape to reference particle was done with the `pip` utility, which is included in the ADDA suite. The results were a single reference particle for each particle shape and size parameter ≥ 10.

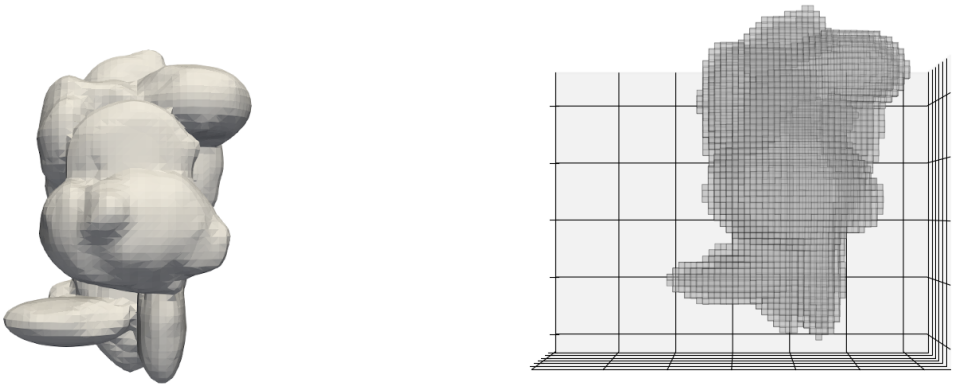

(a) Reference shape **(b)** Reference particle

Figure 3.2: Reference shape D and resulting reference particle. The reference shape (a) is only described by the surface geometry, without any associated absolute size information. The reference particle (b) is the result of a discretisation process, where the geometry and interior volume of the reference shape is approximated by cubes arranged on a lattice. The pictured shape corresponds to a particle with size parameter of 30.2 at 11 dipoles per wavelength for a total of 626123 cubic volume elements.

3.3.2. Spherical inclusions

To generate internally-mixed dust particles, the reference particle's base material was replaced with multiple spherical inclusions of haematite and goethite, each of 1% of the reference particle's volume.

Sphere generation

Initially, a model of a sphere of 1% reference particle volume was built on a cubic (integer) lattice. The first approach, which was to model the inclusions as spheres with integer radius on an integer lattice, resulted in a too granular approach. Spheres on an integer lattice with integer radii are restricted to discrete numbers of contained lattice points (i.e. volume): 1, 7, 33, 123, 257, 515, …[45]. This approach resulted in large deviations from the target of 1% volume of the reference particle. To resolve this problem, the inclusion method was modified:

1. Initially, an integer lattice was generated. Then the radius r of a sphere of 1% of the base particles volume (of N dipoles) was calculated and rounded to the nearest integer[1]: $r = \left\lfloor \sqrt[3]{\frac{3}{4}\frac{\lfloor N \cdot 0.01 \rceil}{\pi}} \right\rceil$

2. The sphere with radius r was placed at the origin of the lattice. All lattice points with euclidean distance $d \leq r$ to the centre of the sphere were counted and marked as part of the sphere.

3. If the number of points was smaller than the number of desired points $M = N \cdot 0.01$, the radius was increased by one and step 2 was repeated, until the number of points M' within the sphere exceeded the number of desired points M.

4. The number of lattice points marked as being inside the sphere were grouped by euclidean distance to the centre of the sphere.

5. At this step the generated sphere was too large, so the number of points had to be reduced, until the desired volume was reached: Starting from the group with the largest distance to the centre, sphere points were removed (unmarked), until the number of points belonging to the sphere was equal to the number of desired points, M. If the number of supernumerary points was larger than the group with the largest remaining distance to the centre, the whole group was removed, otherwise points of the same distance were removed randomly until the target number of remaining points was reached.

Using this procedure, nearly spherical reference inclusions of the right volumes were generated.

Sphere placement

The base particle was built using a integer lattice large enough to enclose it with the lattice points representing the particle's dipole positions. The values of the lattice points were initially set to zero, representing unoccupied volume. Then, the base particle was

[1] Rounding of the radius is not strictly necessary, but simplified the generation algorithm implementation.

read from the file describing the reference particle, which contained the positions of the dipoles. Lattice points of occupied volume were set to 1, representing the base material.

To generate the internally-mixed dust particles, the volume percentage (limited to integers) of haematite and goethite were read from the command line. For each volume percent of inclusion, a new sphere was generated, as described in Section 3.3.2. The lattices on which the spheres were generated were distinct from the lattice of the particle.

For each sphere, a lattice point of the reference particle was chosen randomly and overlaid with the generated sphere centred on that selected point. The values of lattice points overlapping with the sphere were inspected. A new location for the sphere was randomly chosen, if one of these conditions was met:

- if the placed sphere was partially outside the particle's boundary box
- if one or more of the overlapped lattice points were marked as zero (unoccupied), because the sphere placement at this location would have changed the volume of the particle
- if one or more of the overlapped lattice points were marked with a number larger than one (indicating that this point already part of an inclusion), because an overlap of inclusion would lead to a reduction of the total volume of included material.

Only if all of the overlapping points were marked as base material, was the placement of the sphere accepted. This was repeated until the desired volume of the reference particle was replaced by spherical inclusions. See Figure Figure 3.3 for an example.

3.3.3. Homogeneous particle

To study the effect of the inhomogeneities, a reference was needed. For each inhomogeneously mixed particle, a homogeneous counterpart was created. The homogeneous particles had no internal structure. The refractive index was calculated using a simple effective medium approach: the refractive index of all dipoles was set to the volume-weighted average refractive index of the inhomogeneous particle.

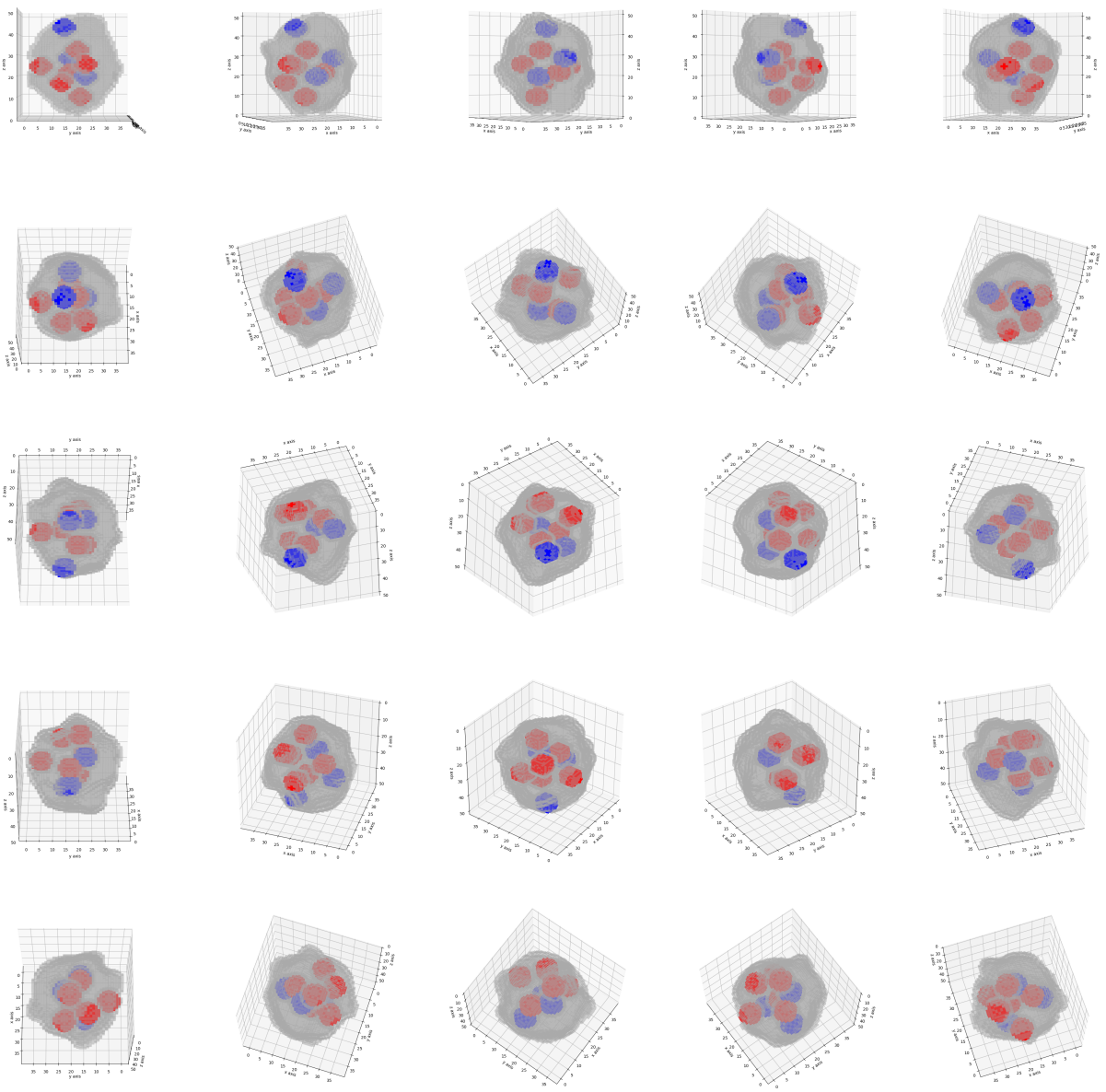

Figure 3.3: Sample internally-mixed particle shown from multiple angles. It was generated as described in Section 3.3.2 and is based on reference particle A with size parameter 11.0 at 11 dipoles/λ. The grey volume is the base material, with six haematite (red) and three goethite (blue) spherical inclusions each of 1% of the particles' volumes. The particle is constructed out of 30374 dipoles arranged on a cubic lattice.

3.4. Computing optical properties with ADDA

The result of an individual DDA simulation were the 16 entries of the Mueller matrix for a total of 102 polar scattering angles and 32 azimuthal angles, saved in the file `mueller_scatgrid`. In addition, the matrix, integrated over the the azimuthal angle, was saved in the file `mueller_integr`. All file names are relative to the directory specific

to an individual run of ADDA.

All calculations were done with ADDA, version 1.3b6. Depending on available computational resources both the MPI and the sequential version of ADDA were used. For a list of used command line parameters see Table A.1.

The result of DDA simulations is dependent on multiple parameters like the spatial resolution (number of dipoles per wavelength) and the stopping criterion for the solver. See Section 4.1.

3.5. Orientation averaging

The computations of the optical properties were done over a multitude of particle orientations. The orientation of the scatterer in respect to the laboratory reference frame within ADDA are specified using the Euler angles α, β and γ, based on [35]. This was done to ensure consistency with the existing MOPSMAP dataset.

The Euler angles for the orientation averaging were based on [16]: The rotation over α, corresponding to a rotation of the scattering plane, was done in ADDA within a single simulation where the Mueller scattering matrix was integrated over 32 azimuthal angles. The optical properties were calculated for 24 values of β, with a 15° step width. The number of values for γ were dependent on the value β, with step widths of down to 15°. The optical properties of each particle were obtained in total from 206 different orientations, that is rotations around β and γ, each corresponding to a single ADDA run. This resulted in a total of $32 \times 206 = 6592$ orientations per particle.

3.6. Examination of the optical properties of ensembles

3.6.1. MOPSMAP

MOPSMAP is a software package which allows modelling of the optical properties of aerosol ensembles, consisting of spherical, spheroidal, and irregularly shaped particles [16].

As the calculation of optical properties of single particles is computationally expensive, MOPSMAP uses a dataset of pre-calculated single particle optical properties and interpolates missing values to generate particle ensembles. Particle ensembles are defined by a size distribution, particle composition and number concentration. MOPSMAP assumes random particle orientation. For this thesis, MOPSMAP was extended for the application of inhomogeneous particles using the results from the ADDA calculations described above.

3.6.2. Particle ensembles

The optical properties of a particle ensemble, based on OPAC (Optical Properties of Aerosols and Clouds) desert mineral dust profiles [46] were calculated. The desert mineral dust composition consisted of a water soluble mode, and mineral dust in the nucle-

ation and accumulation mode, but is lacking the coarse mode, as the particle sizes were outside the calculated single particle size range. For the same reasons the size distributions were limited to an upper diameter of 3.4 µm. In addition, the optical properties of ensembles with a log-normal size distribution of varying modal radii were calculated. For details, see Table 1.c and 4 in [46].

The calculations were done for each particle shape (and for a mixture of all shapes), each mixture type (homogeneous and inhomogeneous) and each combination of haematite and goethite volume percentages. See Table 3.2 for simulation parameters. For the ensembles, the refractive indices were kept constant for all wavelengths, except the imaginary part of haematite's refractive index. For wavelengths between 350 nm and 400 nm the larger imaginary part for haematite was used, for wavelengths between 600 nm and 700 nm the smaller imaginary part for haematite was used. For wavelengths between 400 nm and 600 nm the imaginary part of haematite was interpolated linearly.

Table 3.2. Particle ensemble parameters for single mode size distributions

Parameter	**Values**
wavelengths [µm]	0.35 – 0.70 in 0.01 steps
modal radius [µm]	0.1 – 0.5 in 0.1 steps
haematite content [volume %]	0, 2, 6
goethite content [volume %]	0, 3, 9
optical properties	extinction coefficient, single scattering albedo, absorption coefficient, and asymmetry factor

4. Results

The optical properties of a total of 21313 particles were calculated. This is the combination of six particle shapes, 111 size parameters, ranging from 10^{-3} to 30.2, two mixture methods (homogeneous vs inhomogeneous), nine mixture ratios of goethite and haematite and two refractive indices for haematite, corresponding to two different wavelengths. To keep the required computational resources manageable, only the refractive index of haematite was varied, as it has a significantly stronger wavelength dependence than goethite. This reduced the number of distinct particles from 23976, because for particles without haematite no variation of the refractive index was needed. For each particle a total of 6592 orientations were calculated, requiring 206 DDA simulations per particle, for a total of 4390478 individual DDA simulations. See Table 3.1 for simulation parameters.

Results are shown for shape D. For the results of other shapes see Appendix B. For the particle generation and calculation of individual orientations a volume-equivalent size parameter was used. For the results after orientation averaging, the size parameter was converted to a cross-section equivalent one. The conversion factors for shape A–F were taken from [6].

4.1. Sensitivity to simulation parameters

Because of ADDA's high computing resources requirements, not only trade-offs between numerical accuracy and computing time had to be made, but also it was not possible to run repetitions of calculations within a sensible time frame.

To explore the impact of three effects – the numerical accuracy of ADDA's solver, the placement of inclusions, and the spatial resolution of the particles – subsets of the calculations with varying parameters were repeated.

4.1.1. Effect of the iterative solver's residual

The discrete dipole approximation relies on solving a large number of linear equations [38, 47]. This is done with a iterative solver that stops when the relative norm of the residual falls below a specified limit $10^{-\epsilon}$ [47]. The accuracy of the optical properties' calculations, and also the computation time needed, rises with increasing ϵ. For larger size parameters ≥ 10.0 a stopping criterion of $\epsilon = 3$ was used, as this achieves a good trade-off between accuracy and computation time [16]. For smaller size parameters the greater value of $\epsilon = 6$ was used.

To quantify the effect of the stopping criterion, a subset of calculations was done for multiple values of ϵ (Figure 4.1). Higher values of ϵ converge against the highest value $\epsilon = 6$ that was used, but even the deviation for the lowest value of $\epsilon = 3$ exceeds 0.01% only for the largest size parameters.

4.1.2. Effect of inclusion location

The inclusions for the heterogeneously mixed particles were placed randomly. To study the effects of the inclusion placement, a new set of particles were generated. Based on reference particle D, the inclusion process, as described in Section 3.3 was repeated ten times. New particles were generated for a volume-equivalent size parameter range from 10.0 to 32.7, each inclusion mixture ratio, and all sets of refractive indices. Subsequently the optical properties of these particles were calculated and compared (Figures 4.2 and 4.3.)

For the SSA the effect of the inclusion placement location is small compared to the difference between the homogeneous and inhomogeneous mixtures. For size parameters up to approximately 15, the difference in SSA between the two different refractive indices for haematite is larger than the placement location effect, but for greater size parameters the difference in SSA gets smaller than the variation caused by the randomised inclusion locations. This is also the case for the absorption efficiency and the asymmetry factor, where the effect of the mixture strategy shows a strong divergence when compared to the homogeneously mixed particles. Only for small size parameters < 20, a high haematite content and only for the smaller refractive index of haematite is an overlap in values of the optical properties between mixture types observed. For the extinction efficiency, the effect of the inclusion location shows the largest variation, but for a high haematite content the different mixture types' curves are still distinct. Only in the case of a low haematite content is differentiation between inclusion strategies difficult, as the curves intersect multiple times.

4.1.3. Effect of spatial resolution

The number of dipoles per wavelength, i.e. the spatial resolution of simulated particle, has an influence on the accuracy of the DDA simulation, although the relationship, especially with regards to the refractive index is complex and a minimum of 10 dipoles per wavelength is recommended [31, 38]. Again, this is a compromise between accuracy and computation time. For this thesis' simulations a minimum of 11 dipoles per wavelength have been used, with increasingly higher count for smaller size parameters.

To study the effect of the spatial resolution, i.e. the number of dipoles per wavelength λ, a subset of simulations has been repeated with increased resolution of 22, 33, and 44 dipoles per wavelength: The particle was stretched in each dimension by a factor of 2, 3, or 4. A single dipole at the lowest resolution of 11 dipoles per wavelength was split into 8, 27, or 64 dipoles. The material of split dipoles remained the same, i.e. no smoothing of features was attempted. The DDA simulations were repeated, but the size parameter was kept fixed to the original.

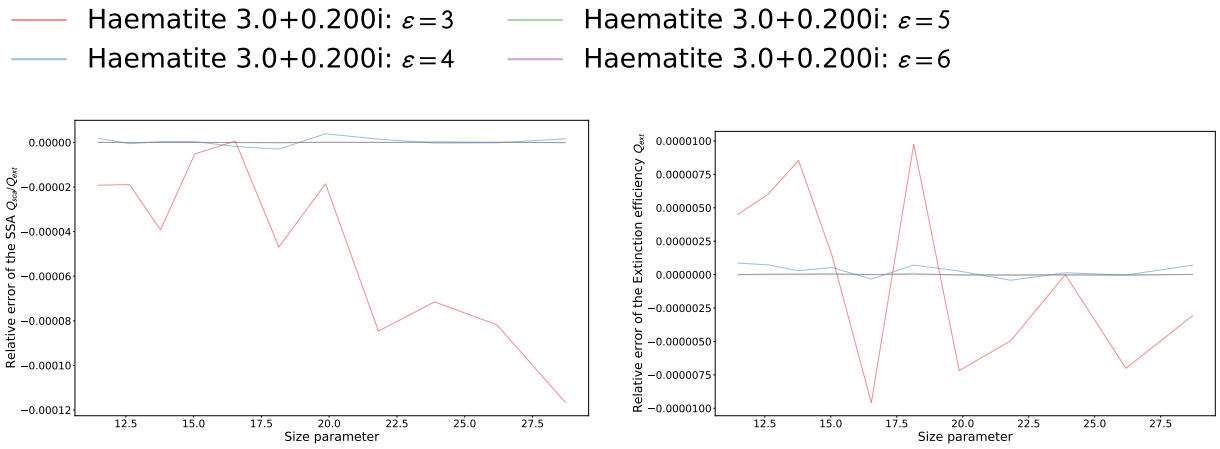

(a) Effect of solver's residual ϵ on SSA

(b) Effect of solver's residual ϵ on Q_E

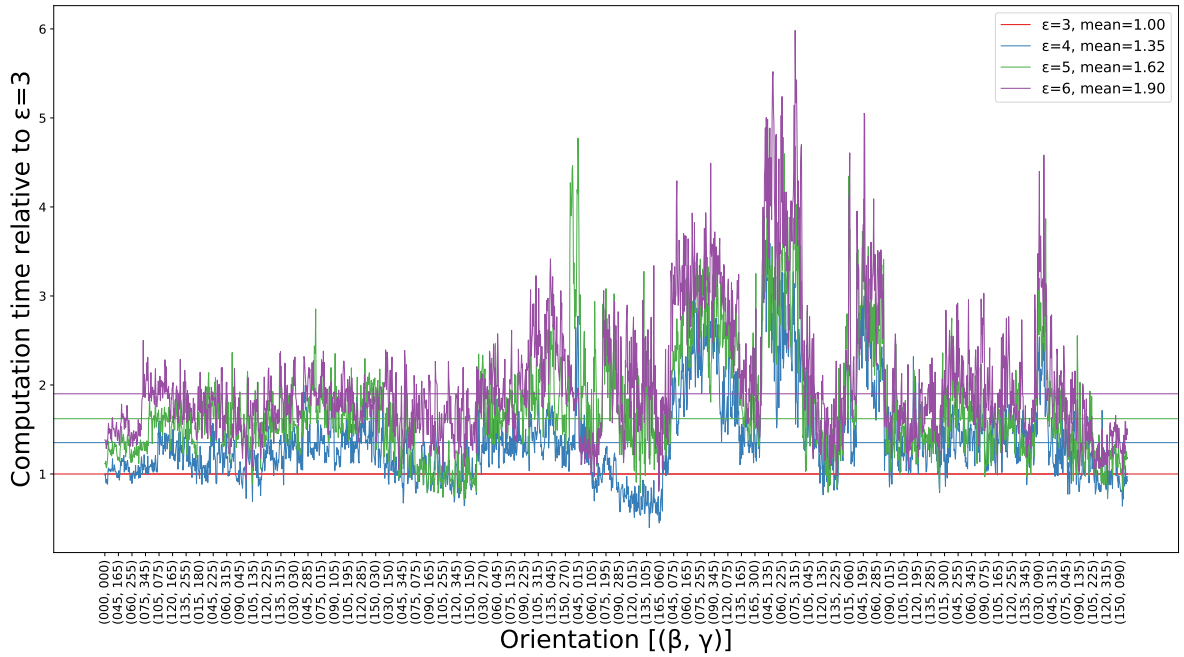

(c) Relative computation time

Figure 4.1: Sensitivity to solver's residual ϵ. Shown are the effects of the solver's residual ϵ on single scattering albedo (a) and extinction efficiency (b) for an inhomogeneous particle with shape D and spherical 2% haematite and 3% goethite inclusions by volume. Both figures show the relative error of the respective quantity for values of $\epsilon = 3$, 4, 5 and 6, compared to the value at $\epsilon = 6$.
The computation times, relative to $\epsilon = 3$, depending on particle orientation, and the mean over all orientations, are shown in (c).

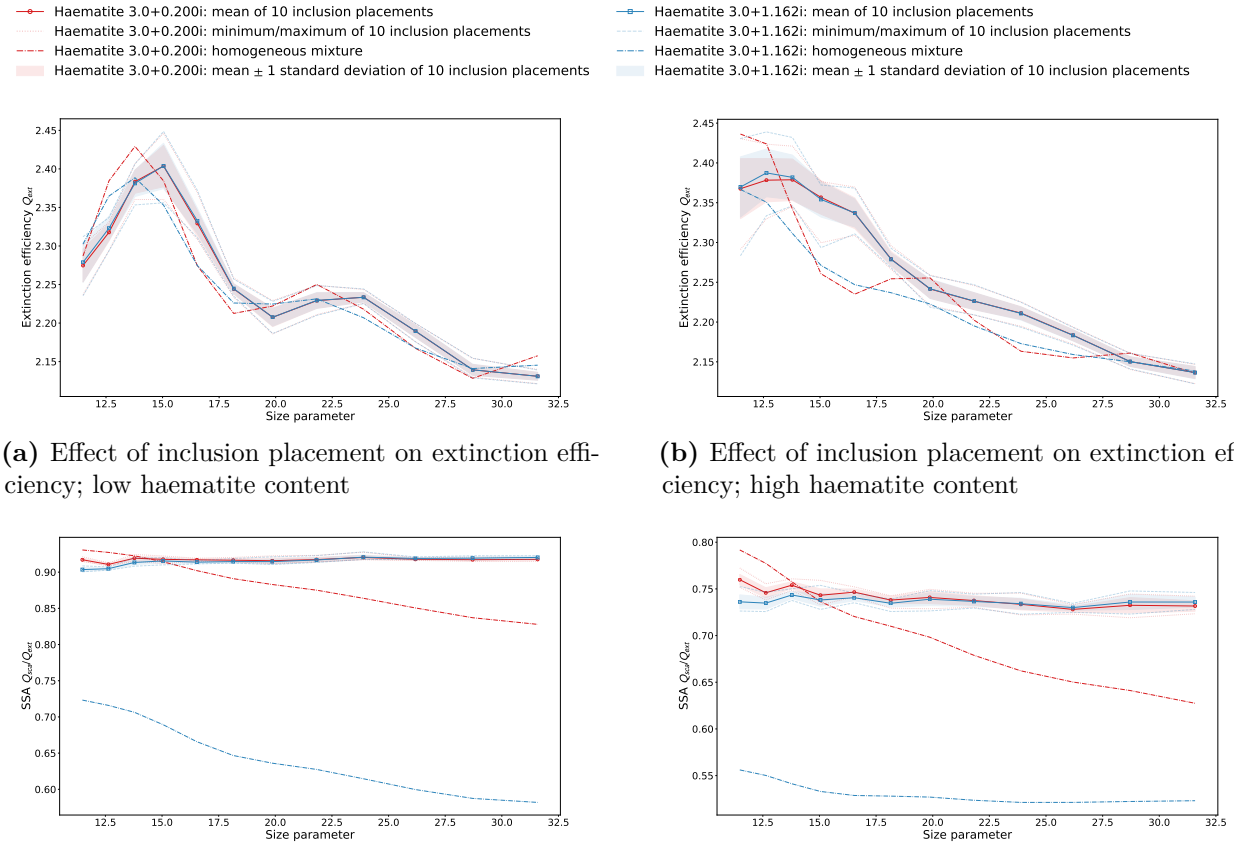

(a) Effect of inclusion placement on extinction efficiency; low haematite content

(b) Effect of inclusion placement on extinction efficiency; high haematite content

(c) Effect of inclusion placement on SSA; low haematite content

(d) Effect of inclusion placement on SSA; high haematite content

Figure 4.2: Effect of inclusion placement location on SSA and extinction efficiency. Shown are the effect on extinction efficiency (top) and SSA (bottom) for particles with shape D and 2% haematite and 0% goethite content by volume (left) and 6% haematite and 3% goethite (right) content by volume.
The red lines indicate the lower refractive index of haematite $(3.0 + 0.2i)$ and the blue lines the higher refractive index $(3.0 + 1.162i)$. The solid lines show the mean of 10 replicates, for which the inclusion locations have been randomised, the shaded areas show the range of mean ± one standard deviation. The dash-dotted lines show the SSA and extinction efficiency for the homogeneous mixture (single run, no replicates). Size parameters are volume equivalents.

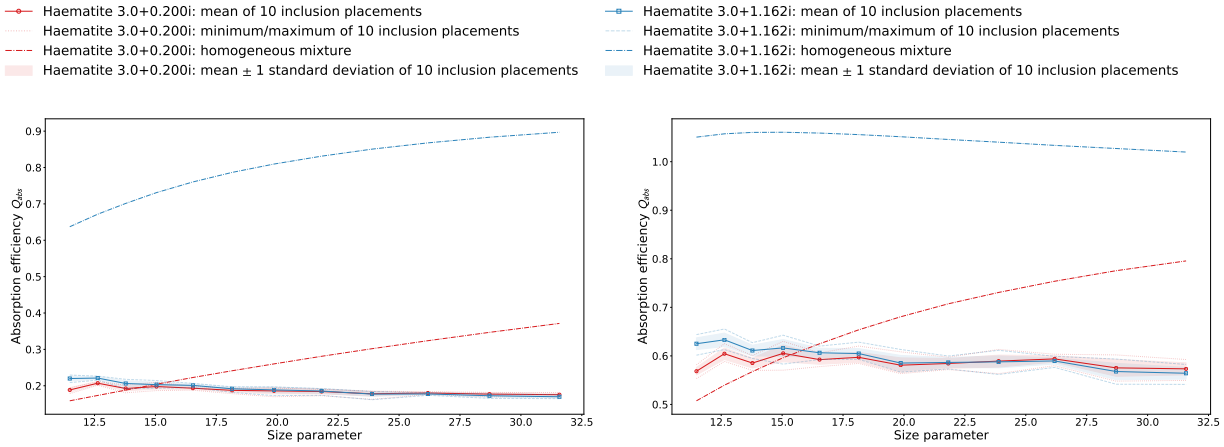

(a) Effect of inclusion placement on absorption efficiency; low haematite content

(b) Effect of inclusion placement on absorption efficiency; high haematite content

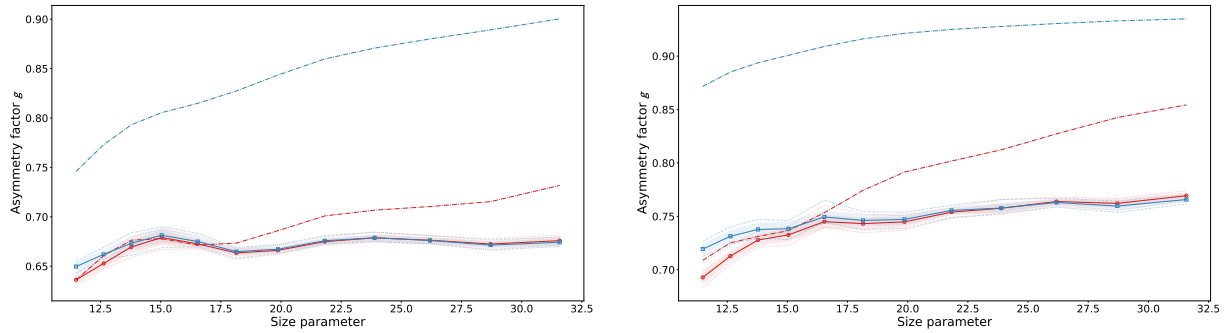

(c) Effect of inclusion placement on asymmetry factor; low haematite content

(d) Effect of inclusion placement on asymmetry factor; high haematite content

Figure 4.3: Effect of inclusion placement location on absorption efficiency and asymmetry factor. Shown are the effect on absorption efficiency (top) and asymmetry factor (bottom) for particles with shape D and 2% haematite and 0% goethite content by volume (left) and 6% haematite and 3% goethite (right) content by volume.
The red lines indicate the lower refractive index of haematite $(3.0 + 0.2i)$ and the blue lines the higher refractive index $(3.0 + 1.162i)$. The solid lines show the mean of 10 replicates, for which the inclusion locations have been randomised, the shaded areas show the range of mean ± one standard deviation. The dash-dotted lines show the absorption efficiency and asymmetry factor for the homogeneous mixture (single run, no replicates). Size parameters are volume equivalents.

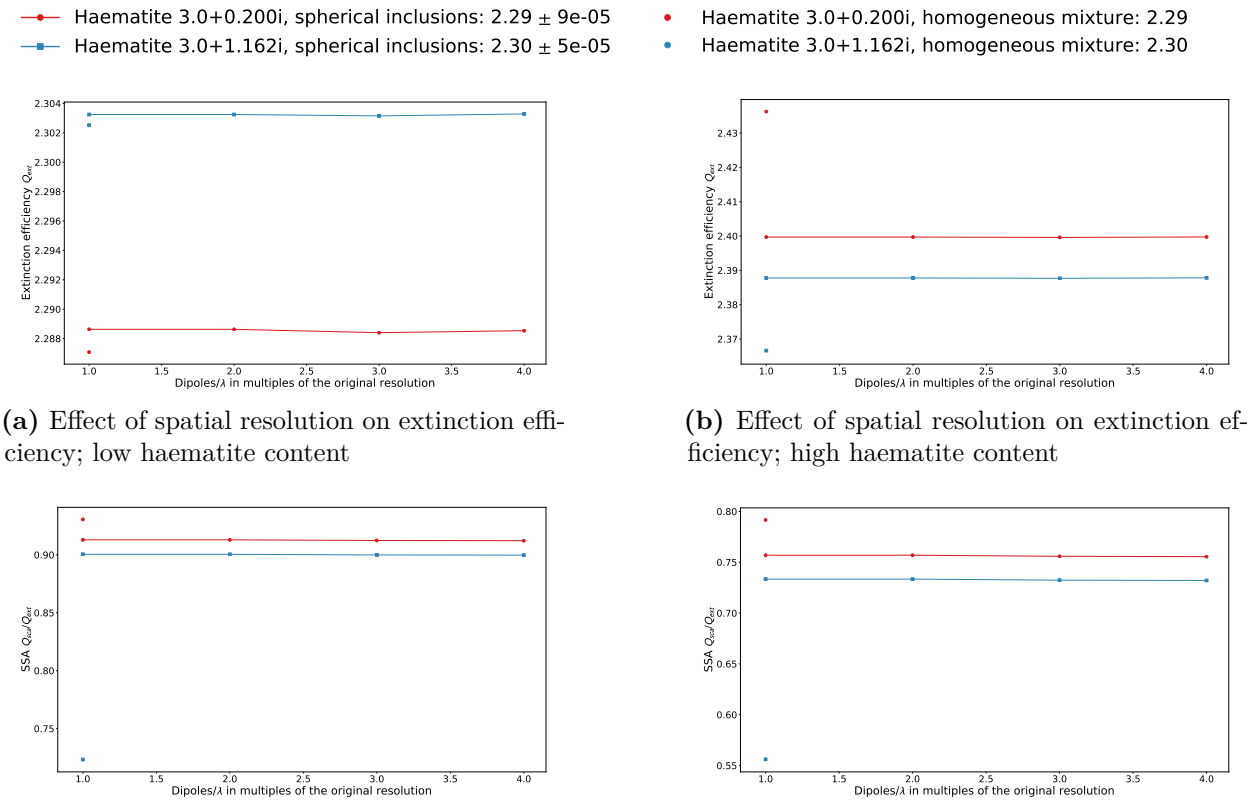

(a) Effect of spatial resolution on extinction efficiency; low haematite content

(b) Effect of spatial resolution on extinction efficiency; high haematite content

(c) Effect of spatial resolution on SSA; low haematite content

(d) Effect of spatial resolution on SSA; high haematite content

Figure 4.4: Effect of spatial resolution on extinction efficiency and SSA. Shown are the effect on absorption efficiency (top) and asymmetry factor (bottom) for particles with shape D and 2% haematite and 0% goethite content by volume (left) and 6% haematite and 3% goethite (right) content by volume. The shown cross-section equivalent size parameter is 11.48.
The red lines indicate the lower refractive index of haematite $(3.0 + 0.2i)$ and the blue lines the higher refractive index $(3.0+1.162i)$. The single markers show the homogeneous case, but only for the original resolution.
The increase in spatial resolution is shown on the x-axis.

The change in the optical parameters' values were orders of magnitude smaller than both the difference between homogeneous and inhomogeneous mixtures and the difference between different refractive indices for haematite, while the computation time increased disproportionally (Figure 4.4 and Table 4.1).

Table 4.1. Effect of spatial resolution on computation time.
Shown are the computation times relative to the base resolution for 11 dipoles/λ for spatial resolutions of 11, 22, 33 and 44 dipoles/λ. Results were averaged over all inclusion mixture ratios for one haematite refractive set.

	dipoles/λ			
	11	22	33	44
relative time	1.0	17.8	67.7	150.6

4.2. Single particle properties

In this section, several single particle properties are shown: extinction efficiency, single scattering albedo, absorption efficiency and asymmetry factor. The results for all particle shapes look similar, so only the plots for particle shape D will be shown.

There is an interesting feature that is common in all properties: For all particle shapes and mixture ratios the SSA, absorption efficiency and asymmetric factor of both refractive indices converges at a size parameter of ≈ 15 in the inhomogeneous case, while this does not happen for the homogeneous mixture. For the extinction efficiency this convergence also happens in the homogeneous mixture, but at higher size parameters than for the inhomogeneous case. Size parameters in subsequent plots are cross-section equivalents.

4.2.1. Extinction efficiency

A difference in extinction efficiency between internally (heterogeneously) and homogeneously mixed particles can be seen for all shapes. Figures 4.5 and 4.6 show the extinction efficiency for shape D. The difference is strongest in the region starting near the maximum extinction efficiency at a size parameter of approximately 5. It all but vanishes for larger size parameters of approximately 20. In general, the effect of the mixture strategy on the extinction efficiency was stronger than the effect of the refractive indices for haematite.

As expected (cf. Section 2.3.3), the extinction efficiency converges to 2.0 for large size parameters

4.2.2. Single scattering albedo

For all cases a common pattern can be found in the single scattering albedo (SSA), see Figure 4.7. A difference between the homogeneous mixture of materials and spherical

inclusions is clearly visible for all mixtures and refractive indices. For smaller size parameters, the SSA of the inhomogeneously mixed particles is lower than the homogeneous case for haematite's lower refractive index of $3.0+0.2i$ and higher for the higher refractive index $3.0 + 1.162i$.

For all particle shapes and mixture ratios the SSA of both refractive indices converges at a size parameter of ≈ 15 in the inhomogeneous case, while this does not happen for the homogeneous mixture. At about the same size parameter, the SSA of the inhomogeneous mixtures of the lower refractive index rises above the homogeneous mixture SSA.

For homogeneous mixtures the SSA's difference between different refractive indices decreases with increasing size parameter. This becomes visible for size parameters larger than ≈ 20. Figures 4.7 and 4.8 show the single scattering albedo for shape D. The deviations of the inhomogeneous from the homogeneous case are stronger for the SSA than for the extinction efficiency, c.f. Figure 4.5. The largest difference in SSA between mixture types can be for seen for low (2%) haematite content for the higher refractive index at large size parameters.

4.2.3. Absorption efficiency

Figures 4.9 and 4.10 show the absorption efficiency for shape D. For the homogeneous case, the absorption efficiency increases with the particle size for almost all mixtures. Only for the greater value of refractive index imaginary part and high percentages of haematite ($\geq 6\%$) is the maximum of the absorption efficiency reached in the simulated size range. The absorption efficiencies for all mixtures are distinct between refractive indices across the size range: The absorption efficiency for the greater imaginary part of haematite's refractive index is higher than for the smaller one. For size parameters > 20 the absorption efficiency is up to 4–5 times higher in the homogeneous case.

For the heterogeneous mixture (i.e. with spherical inclusions) an interesting feature can be seen: Unlike the homogeneous case, the absorption efficiencies for the different refractive indices of haematite converge after reaching a certain size parameter, approximately for values of size parameter 12.5–15.

These results are consistent with results for the single scattering albedo, see Equation (2.10). The difference in single scattering albedo for the different mixture strategies seems to be mostly caused by the change in absorption efficiency, which shows a larger effect than the extinction efficiency.

4.2.4. Asymmetry factor

Figures 4.11 and 4.12 show the asymmetry factor for shape D. As for the properties discussed above, the same pattern emerges: the asymmetry factor for the different refractive indices of inhomogeneous mixed particles converges, while for the homogeneous case this does not happen in the examined size range.

The asymmetry factor for the inhomogeneous mixture tends to be lower than for the homogeneous case, especially for larger size parameters, indicating a weaker forward-scattering of the incident light for the inhomogeneous mixture.

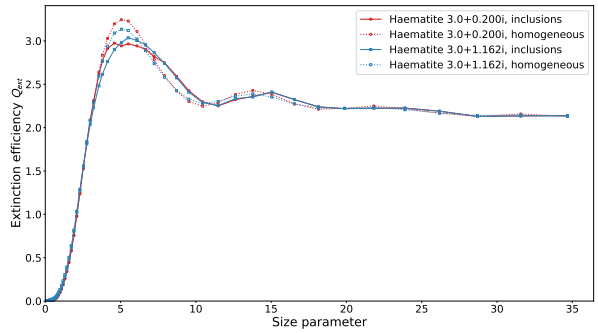

(a) Haematite 2%, goethite 0%

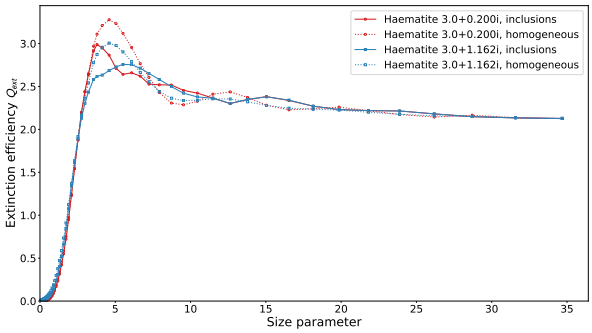

(b) Haematite 6%, goethite 0%

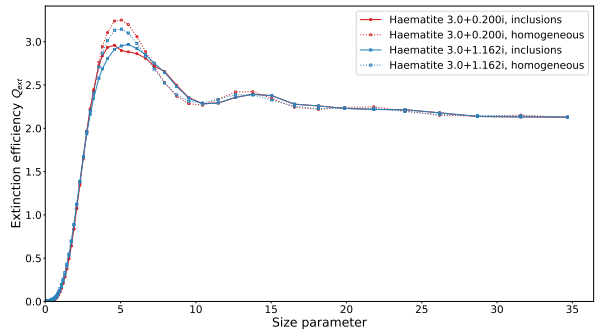

(c) Haematite 2%, goethite 3%

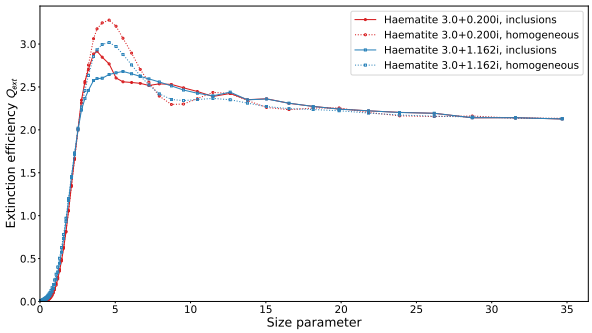

(d) Haematite 6%, goethite 3%

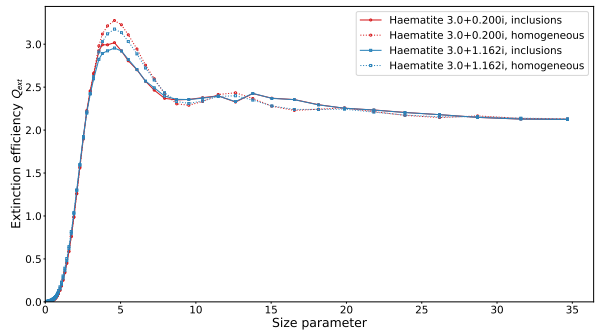

(e) Haematite 2%, goethite 9%

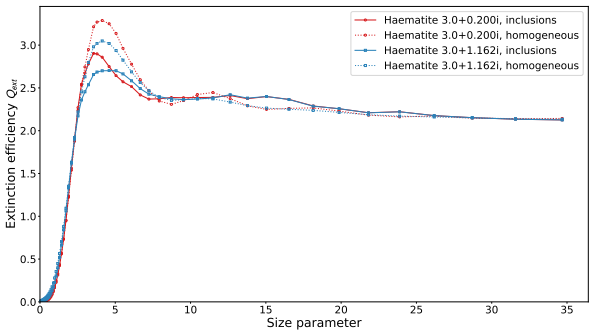

(f) Haematite 6%, goethite 9%

Figure 4.5: Extinction efficiency comparison for shape D. Shown is the extinction efficiency for a range of size parameters. The colours indicate the refractive index of haematite (red: $3.0 + 0.2i$, blue: $3.0 + 1.162i$), corresponding to different wavelengths, while the line style indicates the mixture strategy: Inhomogeneous mixture (inclusions of one percent volume spheres each) are shown as solid lines, the homogeneous mixtures shown as dotted lines. Shown are six different mixture ratios (a) – (f) of haematite and goethite by volume.

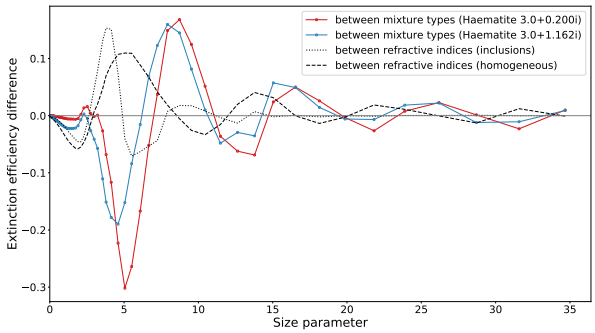

(a) Haematite 2%, goethite 0%

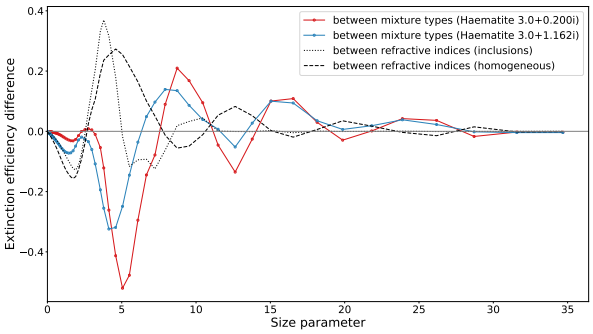

(b) Haematite 6%, goethite 0%

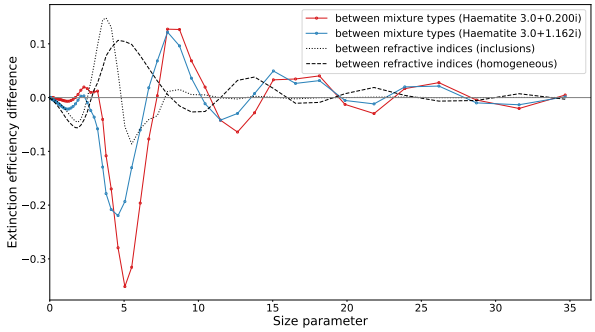

(c) Haematite 2%, goethite 3%

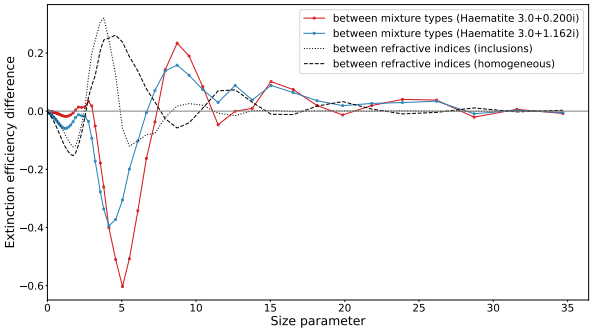

(d) Haematite 6%, goethite 3%

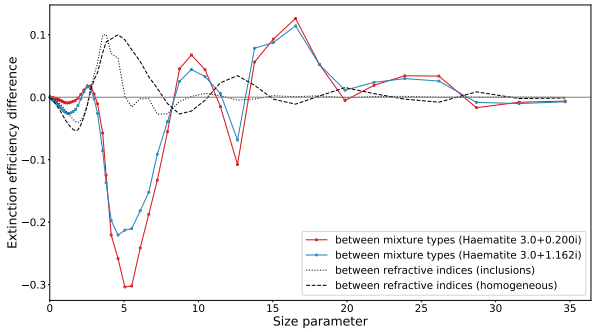

(e) Haematite 2%, goethite 9%

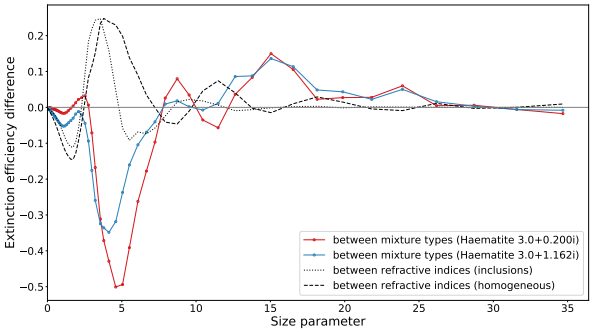

(f) Haematite 6%, goethite 9%

Figure 4.6: Difference in extinction efficiency for shape D. Shown is the difference in extinction efficiency between mixture strategies, i.e. spherical inclusions vs homogeneous in solid lines (red: $3.0 + 0.2i$, blue: $3.0 + 1.162i$) and between refractive indices in black (dotted for spherical inclusions and dashed for the homogeneous case).
Shown are six different mixture ratios (a) – (f) of haematite and goethite by volume.

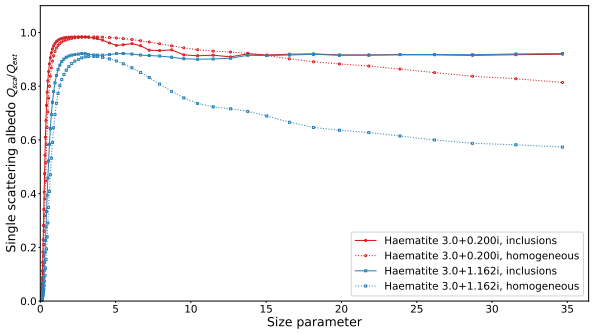

(a) Haematite 2%, goethite 0%

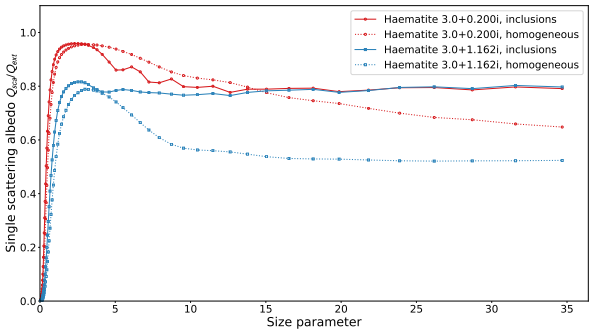

(b) Haematite 6%, goethite 0%

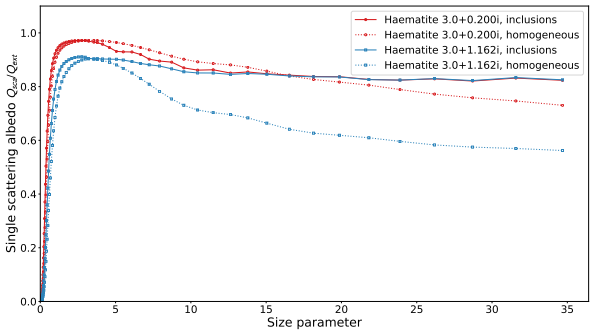

(c) Haematite 2%, goethite 3%

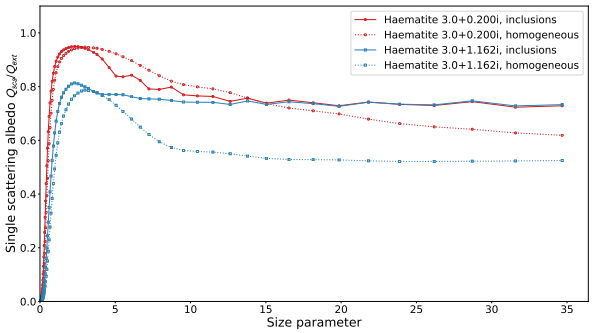

(d) Haematite 6%, goethite 3%

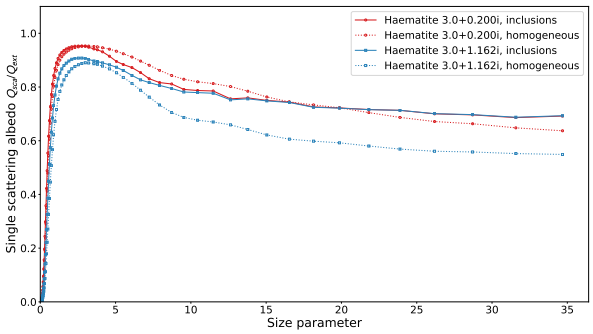

(e) Haematite 2%, goethite 9%

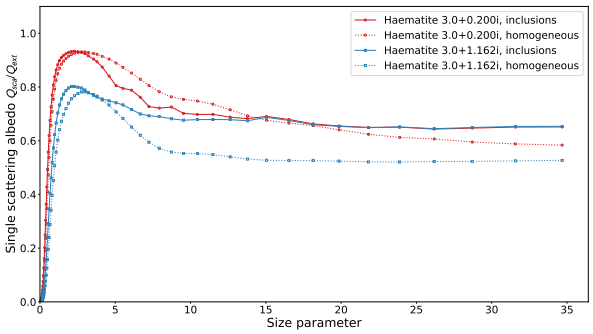

(f) Haematite 6%, goethite 9%

Figure 4.7: Single scattering albedo comparison for shape D. Shown is the single scattering albedo for a range of size parameters. The colours indicate the refractive index of haematite (red: $3.0 + 0.2i$, blue: $3.0 + 1.162i$), corresponding to different wavelengths, while the line style indicates the mixture strategy: Inhomogeneous mixture (inclusions of one percent volume spheres each) are shown as solid lines, the homogeneous mixtures shown as dotted lines. Shown are six different mixture ratios (a) – (f) of haematite and goethite by volume.

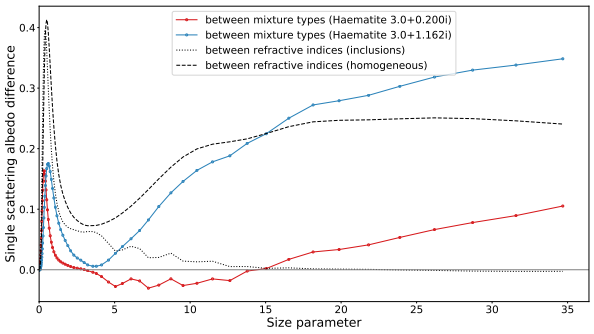

(a) Haematite 2%, goethite 0%

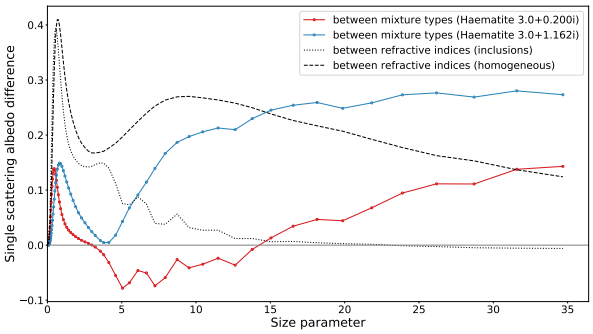

(b) Haematite 6%, goethite 0%

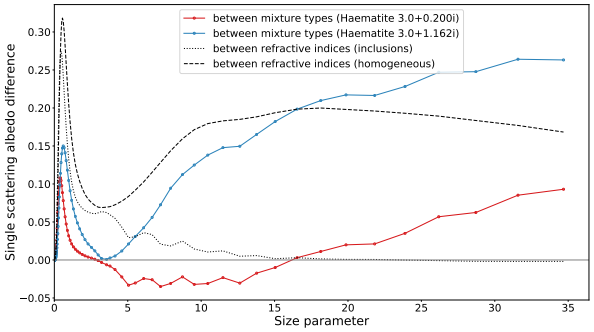

(c) Haematite 2%, goethite 3%

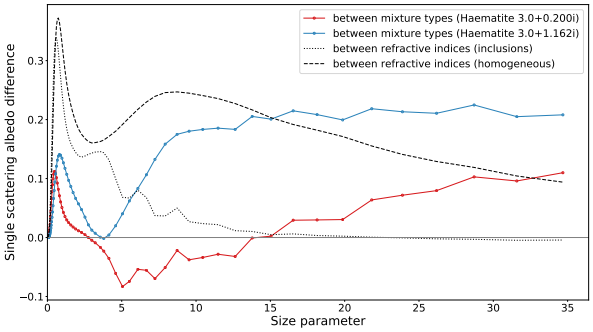

(d) Haematite 6%, goethite 3%

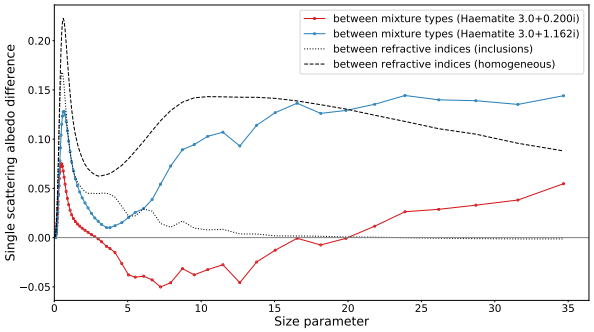

(e) Haematite 2%, goethite 9%

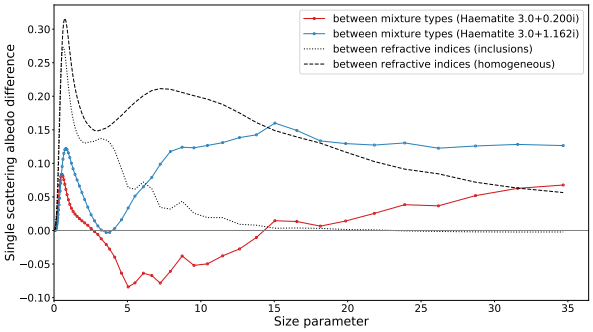

(f) Haematite 6%, goethite 9%

Figure 4.8: Difference in single scattering albedo for shape D. Shown is the difference in single scattering albedo between mixture strategies, i.e. spherical inclusions vs homogeneous in solid lines (red: $3.0 + 0.2i$, blue: $3.0 + 1.162i$) and between refractive indices in black (dotted for spherical inclusions and dashed for the homogeneous case). Shown are six different mixture ratios (a) – (f) of haematite and goethite by volume.

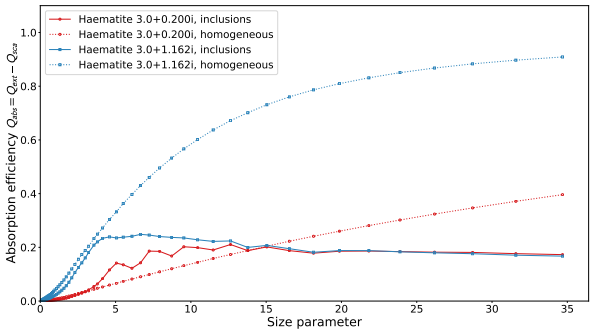

(a) Haematite 2%, goethite 0%

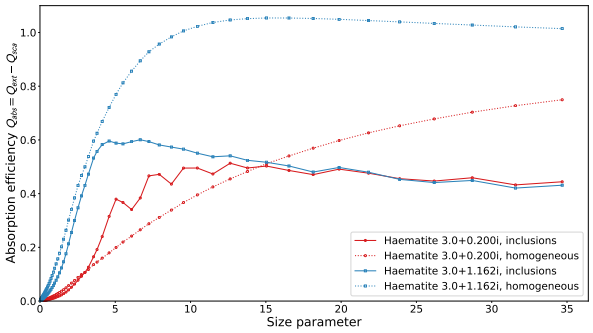

(b) Haematite 6%, goethite 0%

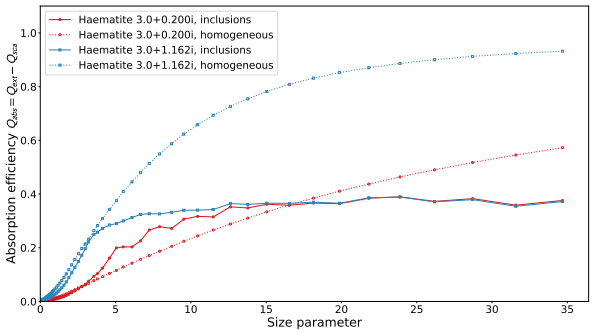

(c) Haematite 2%, goethite 3%

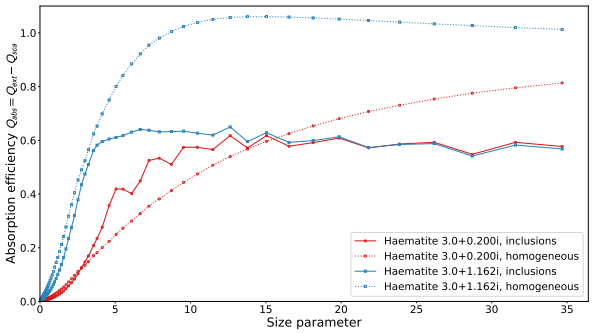

(d) Haematite 6%, goethite 3%

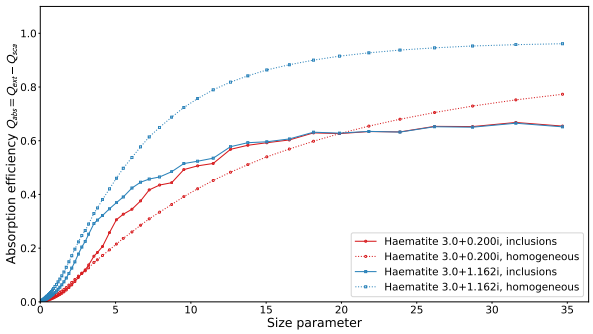

(e) Haematite 2%, goethite 9%

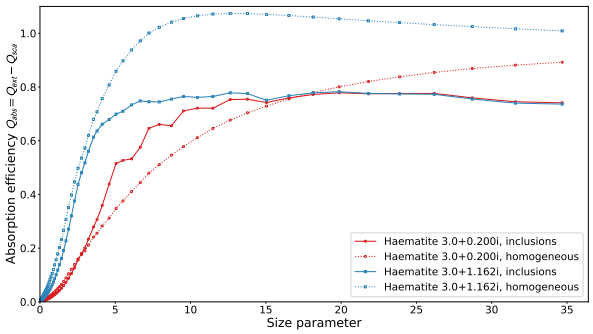

(f) Haematite 6%, goethite 9%

Figure 4.9: Absorption efficiency comparison for shape D. Shown is the absorption efficiency for a range of size parameters. The colours indicate the refractive index of haematite (red: $3.0 + 0.2i$, blue: $3.0 + 1.162i$), corresponding to different wavelengths, while the line style indicates the mixture strategy: Inhomogeneous mixture (inclusions of one percent volume spheres each) are shown as solid lines, the homogeneous mixtures shown as dotted lines. Shown are six different mixture ratios (a) – (f) of haematite and goethite by volume.

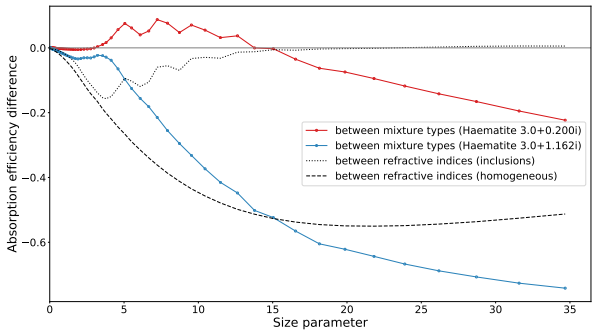

(a) Haematite 2%, goethite 0%

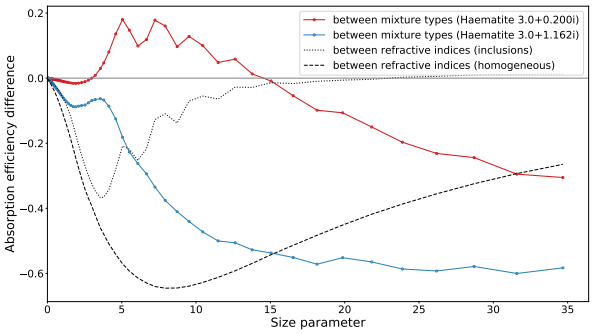

(b) Haematite 6%, goethite 0%

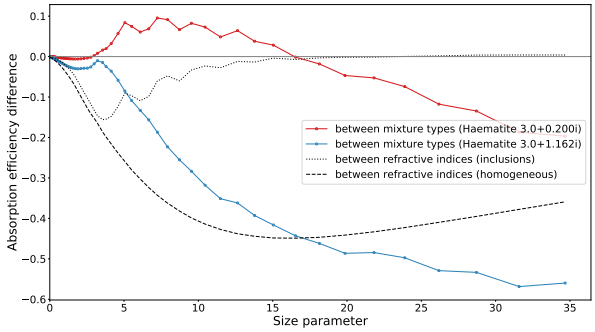

(c) Haematite 2%, goethite 3%

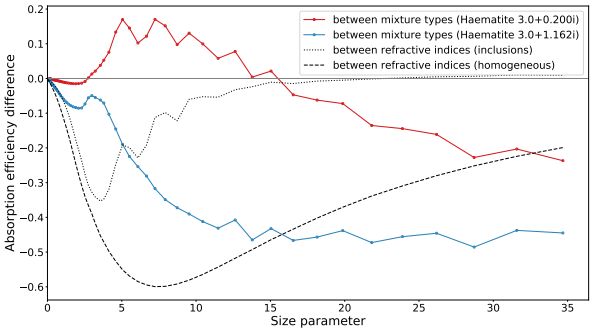

(d) Haematite 6%, goethite 3%

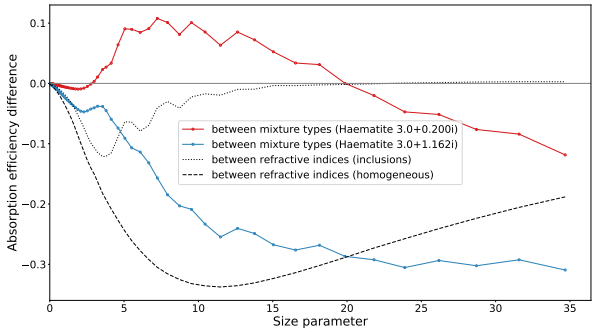

(e) Haematite 2%, goethite 9%

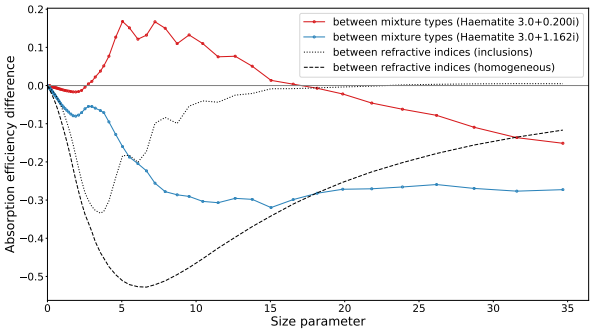

(f) Haematite 6%, goethite 9%

Figure 4.10: Difference in absorption efficiency for shape D. Shown is the difference in absorption efficiency between mixture strategies, i.e. spherical inclusions vs homogeneous in solid lines (red: $3.0 + 0.2i$, blue: $3.0 + 1.162i$) and between refractive indices in black (dotted for spherical inclusions and dashed for the homogeneous case).
Shown are six different mixture ratios (a) – (f) of haematite and goethite by volume.

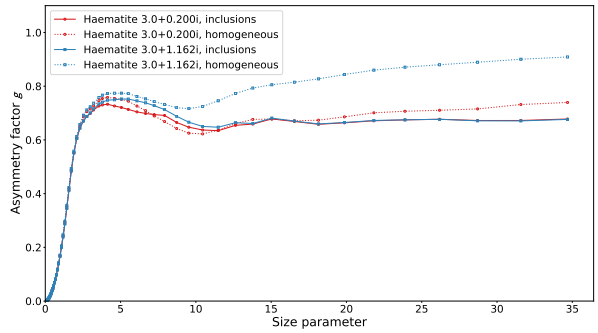

(a) Haematite 2%, goethite 0%

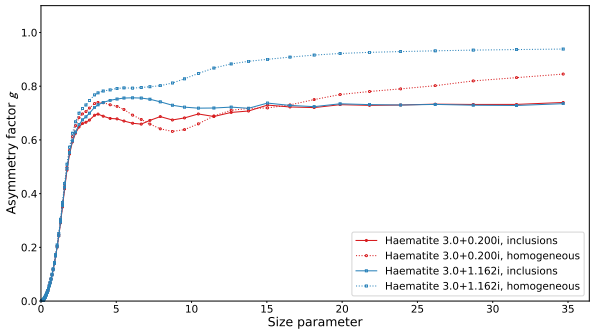

(b) Haematite 6%, goethite 0%

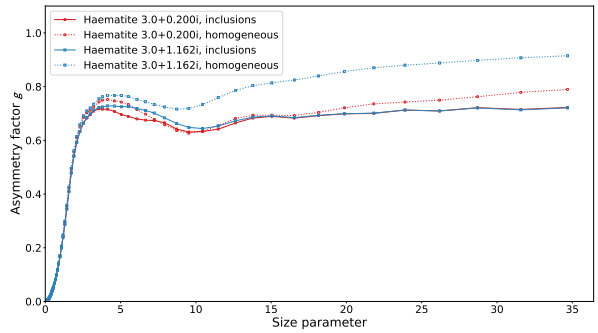

(c) Haematite 2%, goethite 3%

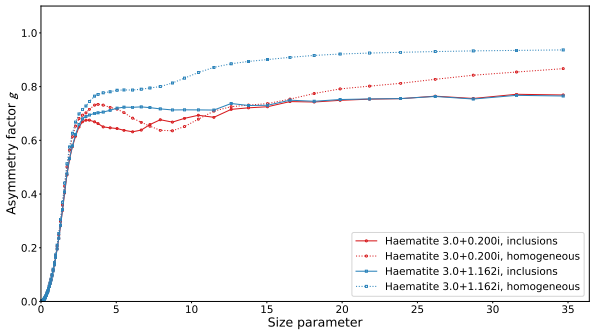

(d) Haematite 6%, goethite 3%

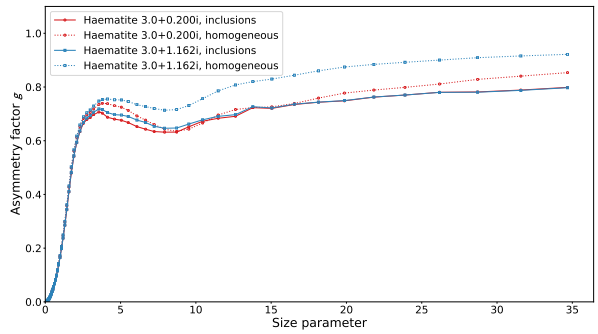

(e) Haematite 2%, goethite 9%

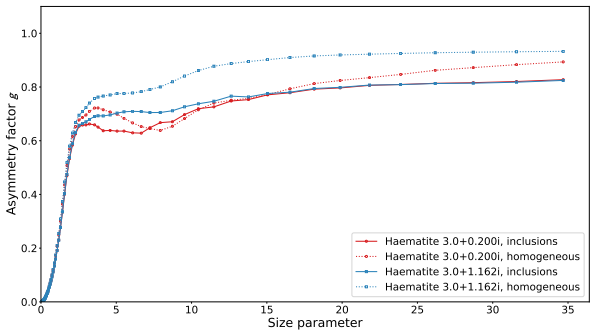

(f) Haematite 6%, goethite 9%

Figure 4.11: Asymmetry factor comparison for shape D. Shown is the asymmetry factor for a range of size parameters. The colours indicate the refractive index of haematite (red: $3.0+0.2i$, blue: $3.0+1.162i$), corresponding to different wavelengths, while the line style indicates the mixture strategy: Inhomogeneous mixture (inclusions of one percent volume spheres each) are shown as solid lines, the homogeneous mixtures shown as dotted lines. Shown are six different mixture ratios (a) – (f) of haematite and goethite by volume.

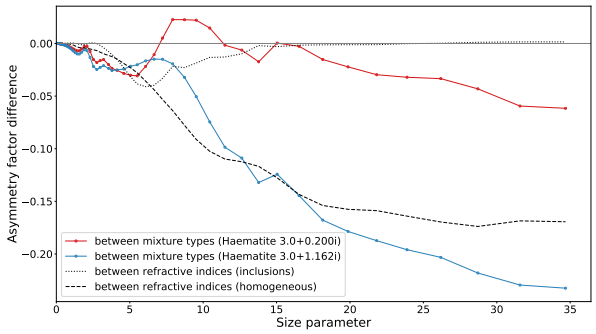

(a) Haematite 2%, goethite 0%

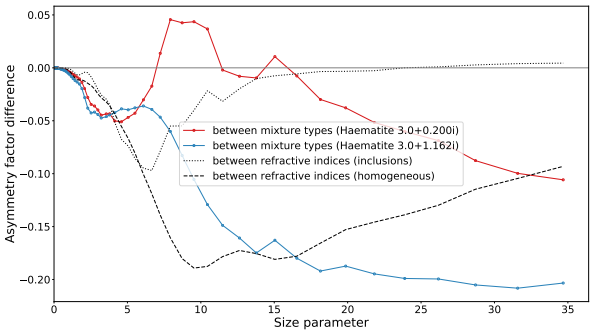

(b) Haematite 6%, goethite 0%

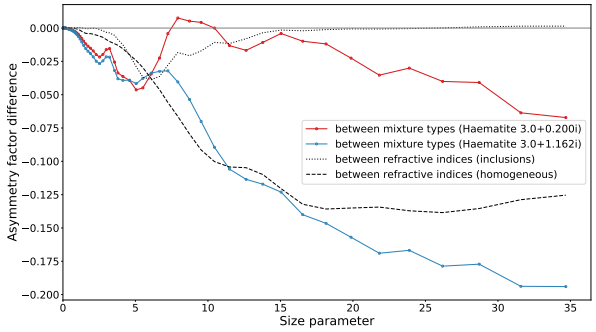

(c) Haematite 2%, goethite 3%

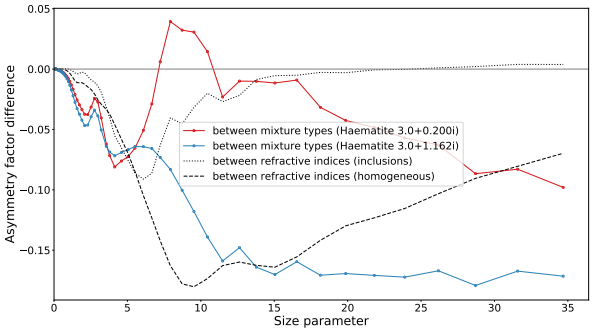

(d) Haematite 6%, goethite 3%

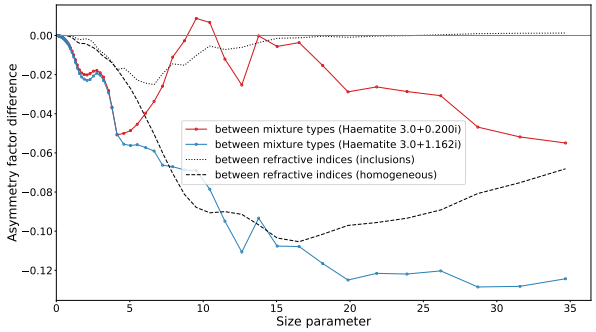

(e) Haematite 2%, goethite 9%

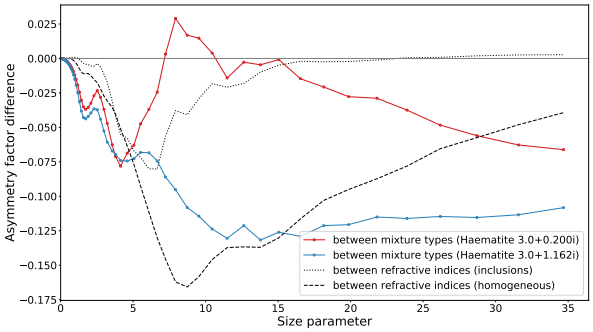

(f) Haematite 6%, goethite 9%

Figure 4.12: Difference in asymmetry factor for shape D. Shown is the difference in asymmetry factor between mixture strategies, i.e. spherical inclusions vs homogeneous in solid lines (red: $3.0 + 0.2i$, blue: $3.0 + 1.162i$) and between refractive indices in black (dotted for spherical inclusions and dashed for the homogeneous case).
Shown are six different mixture ratios (a) – (f) of haematite and goethite by volume.

4.3. Particle ensembles

The extinction coefficient, single scattering albedo, absorption coefficient and the asymmetry factor for log-normal size distributions and desert mineral dust were calculated for wavelengths of visible light. Pictured (Figures 4.13 to 4.16) are the results for a mixture of shapes A–F in equal parts.

Generally, a trend can be seen: with the exception of the extinction coefficient, which shows little difference between homogeneous and inhomogeneous particles, the optical properties show a larger divergence between inhomogeneous and homogeneous particles at smaller wavelengths.

To compare the effect of the internal mixture strategy, two indices, based on the absolute value of the point-wise difference Δ_λ between the curves were used. For the intensive properties, the single scattering albedo and the asymmetry factor, the absolute point-wise difference $\Delta_{\lambda,\text{abs}}$ was used:

$$\Delta_{\lambda,\text{abs}} = |a_{\text{inh},\lambda} - a_{\text{hom},\lambda}| \tag{4.1}$$

where $a_{\text{inh},\lambda}$ is the value of the optical property for the inhomogeneous particles at wavelength λ, $a_{\text{hom},\lambda}$is the value of the optical property for the homogeneous particles at wavelength λ. For the extensive properties, the extinction and absorption coefficient, the relative point-wise difference $\Delta_{\lambda,\text{rel}}$ was used:

$$\Delta_{\lambda,\text{rel}} = |\frac{a_{\text{inh},\lambda} - a_{\text{hom},\lambda}}{a_{\text{hom},\lambda}}| \tag{4.2}$$

The mean differences $\bar{\Delta}_{\text{abs}}$ and $\bar{\Delta}_{\text{rel}}$ are the means of point-wise absolute and respectively relative differences over all wavelengths.
The higher $\bar{\Delta}_{\text{rel}}$ is, the larger the impact of the inhomogeneities. A value of 0 for $\bar{\Delta}_{\text{rel}}$ indicates that there is no difference between internal mixture strategies, and that the curves are identical. A value of 0.1 for $\bar{\Delta}_{\text{rel}}$ means that on average, the value for the inhomogeneous particles was 10% greater or smaller than for the homogeneous case.

Additionally $\Delta_{\text{rel, max}}$ was calculated, the maximum relative difference. For approximately parallel curves, $\Delta_{\text{rel, max}}$ and $\bar{\Delta}_{\text{rel}}$ are equal.

4.3.1. Extinction coefficient

The internal mixture has little effect on the extinction coefficient. Even for the distribution with the largest modal radius a small relative difference in extinction coefficient can be seen only for large wavelengths and high inclusion volume. Even then, the maximum difference between mixing strategies across all ensembles is only 6%, see Figure 4.13 and Table 4.2.

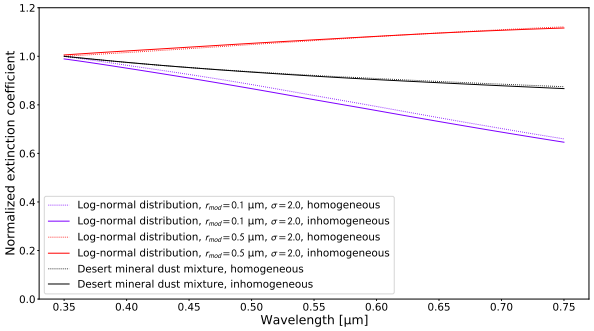

(a) Haematite 2%, goethite 0%

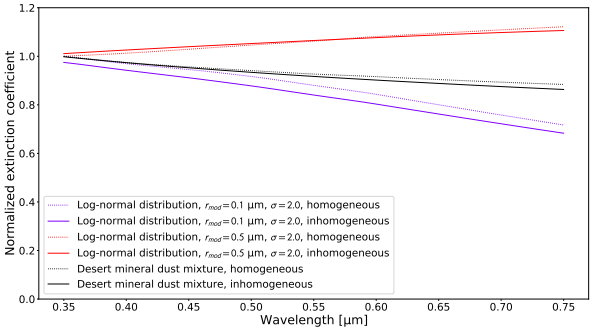

(b) Haematite 6%, goethite 0%

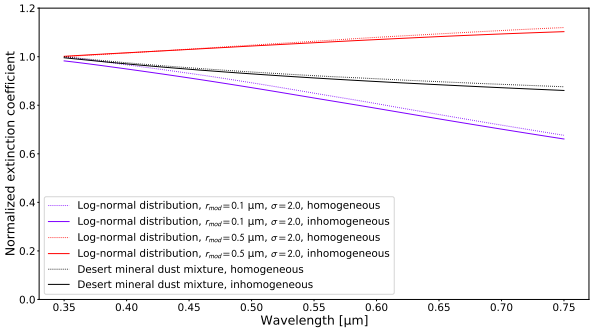

(c) Haematite 2%, goethite 3%

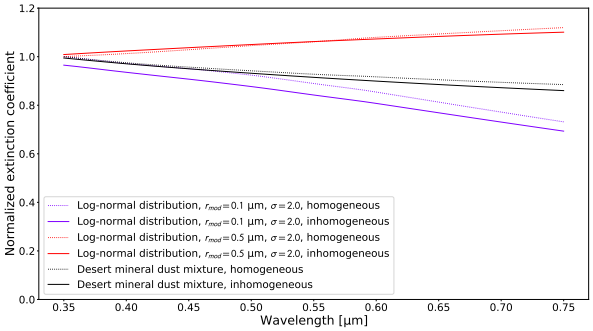

(d) Haematite 6%, goethite 3%

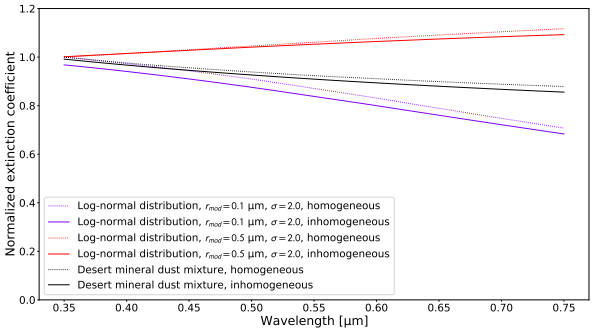

(e) Haematite 2%, goethite 9%

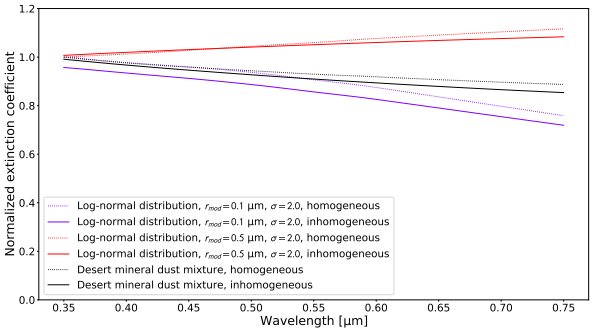

(f) Haematite 6%, goethite 9%

Figure 4.13: Normalised extinction coefficient comparison for shapes A–F. Shown is the wavelength dependent normalised extinction coefficient of log-normal distributions with different modal radii (colours) and a desert mineral dust mixture (black). Homogeneous particles are shown as dotted lines, inhomogeneous particles as solid lines.
Values have been normalised to the value of the respective homogeneous mixture at the shortest wavelength.
Shown are six different mixture ratios (a) – (f) of haematite and goethite by volume.

4.3.2. Single scattering albedo

For the single scattering albedo, the internal mixture type's effect is clearly visible and more pronounced for shorter wavelengths, where the SSA of the inhomogeneous mixture is larger than in the homogeneous case. This trend reverses for wavelengths of about 0.55–0.60 µm where the SSA for the homogeneous case becomes larger than for the inhomogeneous case. The maximum difference is as high as 0.16–0.38, depending on inclusion volume percentages and particle ensemble.

Additionally, the variation in SSA over the wavelength range is much larger for the homogeneous case. This can be seen for all size distributions (Figure 4.14 and Table 4.3).

4.3.3. Absorption coefficient

As for the single scattering albedo, a difference between internal mixture types can be seen. This effect is pronounced for the distribution with the largest modal radius, but all but vanishes for smaller modal radii. The effect of the inclusions is a significantly lower absorption coefficient for wavelengths up to about 0.5–0.6µm compared to the homogeneous case, while it is slightly higher at larger wavelengths. Of all optical properties, the absorption coefficient shows the largest differences between internal mixture types: up to 23%–70% depending on inclusion volume percentages and particle ensemble (Figure 4.15 and Table 4.4).

4.3.4. Asymmetry factor

A large difference for the asymmetry factor between internal mixture types can be seen for all particle ensembles and size distributions. The effect is more pronounced for shorter wavelengths. The inhomogeneous particles show a lower asymmetry factor compared to the homogeneous case, indicating a less pronounced forward scattering of light. The maximum difference is as high as 0.12–0.14 depending on inclusion volume percentages and particle ensemble (Figure 4.16 and Table 4.5).

Table 4.2. Extinction coefficient mean relative difference between homogeneous and inhomogeneous ensembles. Shown are the mean relative difference $\bar{\Delta}_{\text{rel}}$, and the maximum relative difference $\Delta_{\text{rel, max}}$ for combinations of haematite (H) and goethite (G) content (as percentage of the particle's volume) and particle ensembles.

H [%]	G [%]	Ensemble	$\bar{\Delta}_{\text{rel}}$	$\Delta_{\text{rel, max}}$
2	0	log-normal, $r_{mod} = 0.1$	0.02	0.02
2	0	log-normal, $r_{mod} = 0.5$	0.00	0.01
2	0	OPAC mineral dust	0.00	0.01
6	0	log-normal, $r_{mod} = 0.1$	0.04	0.05
6	0	log-normal, $r_{mod} = 0.5$	0.01	0.01
6	0	OPAC mineral dust	0.01	0.02
2	3	log-normal, $r_{mod} = 0.1$	0.02	0.02
2	3	log-normal, $r_{mod} = 0.5$	0.01	0.02
2	3	OPAC mineral dust	0.01	0.02
6	3	log-normal, $r_{mod} = 0.1$	0.05	0.05
6	3	log-normal, $r_{mod} = 0.5$	0.01	0.02
6	3	OPAC mineral dust	0.01	0.03
2	9	log-normal, $r_{mod} = 0.1$	0.04	0.04
2	9	log-normal, $r_{mod} = 0.5$	0.01	0.02
2	9	OPAC mineral dust	0.02	0.03
6	9	log-normal, $r_{mod} = 0.1$	0.05	0.06
6	9	log-normal, $r_{mod} = 0.5$	0.01	0.03
6	9	OPAC mineral dust	0.02	0.04

Table 4.3. Single scattering albedo mean differences between homogeneous and inhomogeneous ensembles. Shown are the mean absolute difference $\bar{\Delta}_{\text{abs}}$, and the maximum absolute difference $\Delta_{\text{abs, max}}$ for combinations of haematite (H) and goethite (G) content (as percentage of the particle's volume) and particle ensembles.

H [%]	G [%]	Ensemble	$\bar{\Delta}_{\text{abs}}$	$\Delta_{\text{abs, max}}$
2	0	log-normal, $r_{mod} = 0.1$	0.02	0.06
2	0	log-normal, $r_{mod} = 0.5$	0.08	0.22
2	0	OPAC mineral dust	0.05	0.14
6	0	log-normal, $r_{mod} = 0.1$	0.03	0.08
6	0	log-normal, $r_{mod} = 0.5$	0.09	0.21
6	0	OPAC mineral dust	0.06	0.14
2	3	log-normal, $r_{mod} = 0.1$	0.02	0.05
2	3	log-normal, $r_{mod} = 0.5$	0.07	0.17
2	3	OPAC mineral dust	0.04	0.11
6	3	log-normal, $r_{mod} = 0.1$	0.03	0.07
6	3	log-normal, $r_{mod} = 0.5$	0.07	0.17
6	3	OPAC mineral dust	0.05	0.12
2	9	log-normal, $r_{mod} = 0.1$	0.02	0.03
2	9	log-normal, $r_{mod} = 0.5$	0.05	0.10
2	9	OPAC mineral dust	0.03	0.06
6	9	log-normal, $r_{mod} = 0.1$	0.02	0.05
6	9	log-normal, $r_{mod} = 0.5$	0.05	0.11
6	9	OPAC mineral dust	0.04	0.08

Table 4.4. Absorption coefficient mean relative difference between homogeneous and inhomogeneous ensembles. Shown are the mean relative difference $\bar{\Delta}_{\text{rel}}$, and the maximum relative difference $\Delta_{\text{rel, max}}$ for combinations of haematite (H) and goethite (G) content (as percentage of the particle's volume) and particle ensembles.

H [%]	G [%]	Ensemble	$\bar{\Delta}_{\text{rel}}$	$\Delta_{\text{rel, max}}$
2	0	log-normal, $r_{mod} = 0.1$	0.29	0.42
2	0	log-normal, $r_{mod} = 0.5$	0.42	0.70
2	0	OPAC mineral dust	0.38	0.62
6	0	log-normal, $r_{mod} = 0.1$	0.20	0.28
6	0	log-normal, $r_{mod} = 0.5$	0.28	0.46
6	0	OPAC mineral dust	0.26	0.41
2	3	log-normal, $r_{mod} = 0.1$	0.21	0.32
2	3	log-normal, $r_{mod} = 0.5$	0.30	0.50
2	3	OPAC mineral dust	0.28	0.46
6	3	log-normal, $r_{mod} = 0.1$	0.17	0.24
6	3	log-normal, $r_{mod} = 0.5$	0.22	0.36
6	3	OPAC mineral dust	0.21	0.33
2	9	log-normal, $r_{mod} = 0.1$	0.13	0.19
2	9	log-normal, $r_{mod} = 0.5$	0.18	0.26
2	9	OPAC mineral dust	0.17	0.24
6	9	log-normal, $r_{mod} = 0.1$	0.12	0.19
6	9	log-normal, $r_{mod} = 0.5$	0.15	0.23
6	9	OPAC mineral dust	0.15	0.22

Table 4.5. Asymmetry factor mean differences between homogeneous and inhomogeneous ensembles. Shown are the mean absolute difference $\bar{\Delta}_{\text{abs}}$, and the maximum absolute difference $\Delta_{\text{abs, max}}$ for combinations of haematite (H) and goethite (G) content (as percentage of the particle's volume) and particle ensembles.

H [%]	G [%]	Ensemble	$\bar{\Delta}_{\text{abs}}$	$\Delta_{\text{abs, max}}$
2	0	log-normal, $r_{mod} = 0.1$	0.03	0.04
2	0	log-normal, $r_{mod} = 0.5$	0.05	0.12
2	0	OPAC mineral dust	0.03	0.07
6	0	log-normal, $r_{mod} = 0.1$	0.05	0.07
6	0	log-normal, $r_{mod} = 0.5$	0.07	0.15
6	0	OPAC mineral dust	0.05	0.09
2	3	log-normal, $r_{mod} = 0.1$	0.03	0.04
2	3	log-normal, $r_{mod} = 0.5$	0.05	0.12
2	3	OPAC mineral dust	0.04	0.07
6	3	log-normal, $r_{mod} = 0.1$	0.06	0.07
6	3	log-normal, $r_{mod} = 0.5$	0.07	0.14
6	3	OPAC mineral dust	0.05	0.09
2	9	log-normal, $r_{mod} = 0.1$	0.05	0.06
2	9	log-normal, $r_{mod} = 0.5$	0.06	0.11
2	9	OPAC mineral dust	0.05	0.07
6	9	log-normal, $r_{mod} = 0.1$	0.05	0.06
6	9	log-normal, $r_{mod} = 0.5$	0.05	0.11
6	9	OPAC mineral dust	0.04	0.07

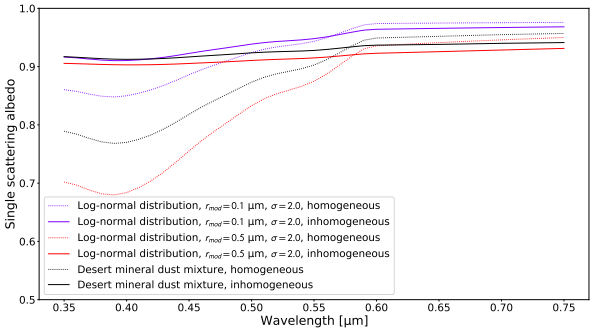

(a) Haematite 2%, goethite 0%

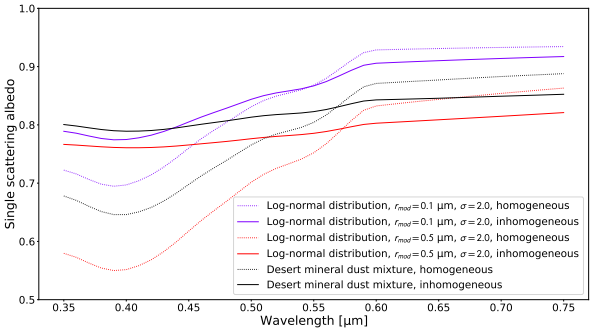

(b) Haematite 6%, goethite 0%

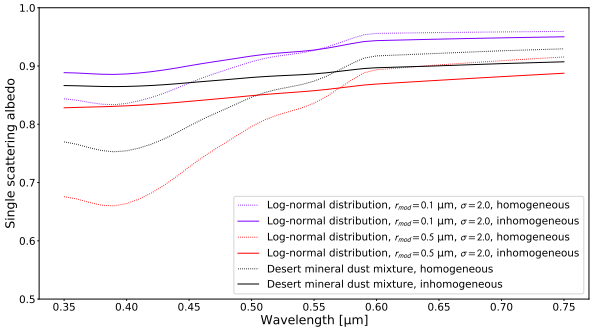

(c) Haematite 2%, goethite 3%

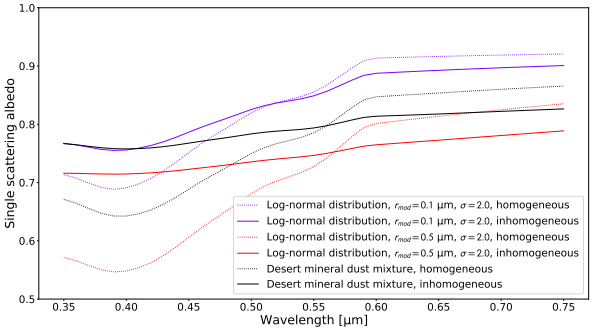

(d) Haematite 6%, goethite 3%

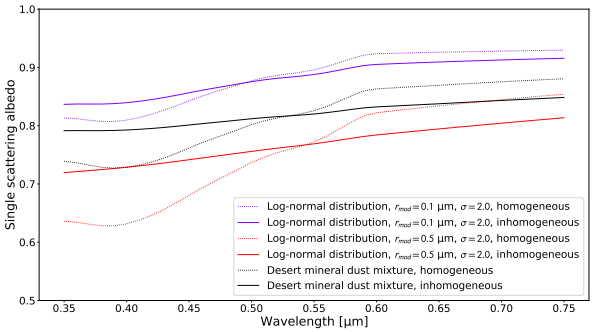

(e) Haematite 2%, goethite 9%

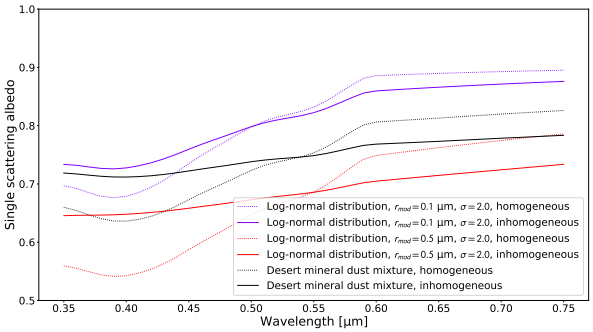

(f) Haematite 6%, goethite 9%

Figure 4.14: Single scattering albedo comparison for shapes A–F. Shown is the wavelength dependent single scattering albedo of log-normal distributions with different modal radii (colours) and a desert mineral dust mixture (black). Homogeneous particles are shown as dotted lines, inhomogeneous particles as solid lines.
Shown are six different mixture ratios (a) – (f) of haematite and goethite by volume.

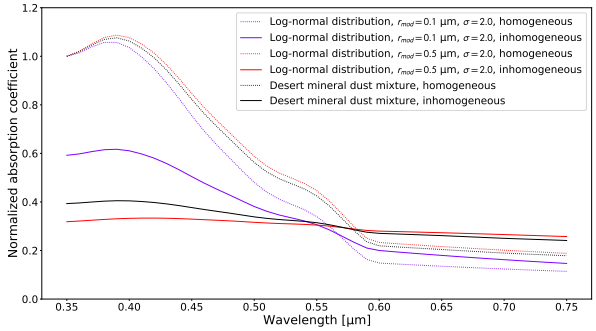

(a) Haematite 2%, goethite 0%

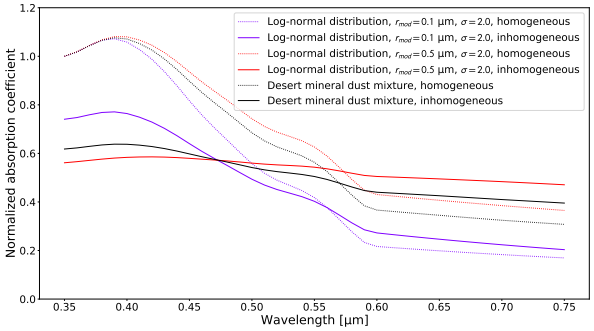

(b) Haematite 6%, goethite 0%

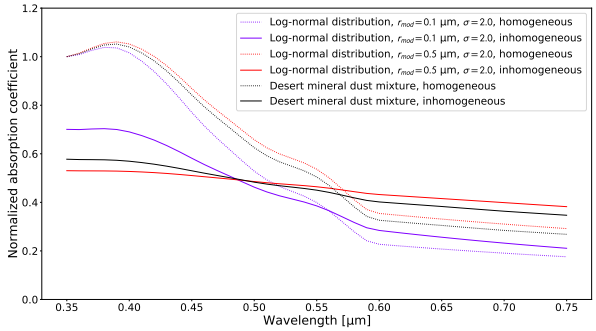

(c) Haematite 2%, goethite 3%

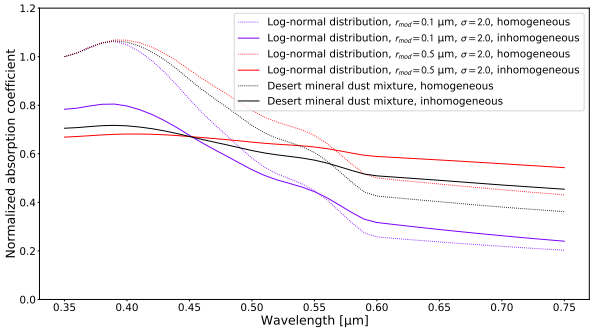

(d) Haematite 6%, goethite 3%

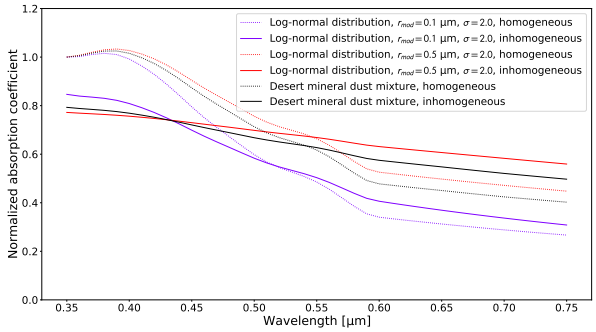

(e) Haematite 2%, goethite 9%

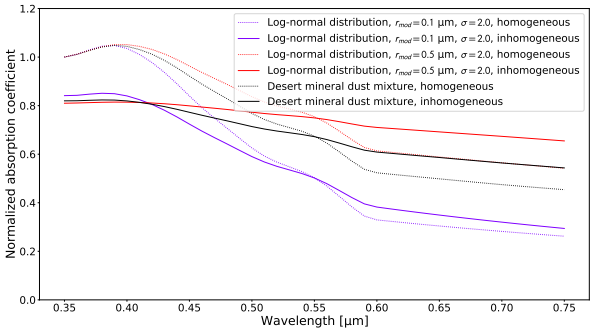

(f) Haematite 6%, goethite 9%

Figure 4.15: Normalised absorption coefficient comparison for shapes A–F. Shown is the wavelength dependent normalised absorption coefficient of log-normal distributions with different modal radii (colours) and a desert mineral dust mixture (black). Homogeneous particles are shown as dotted lines, inhomogeneous particles as solid lines.
Values have been normalised to the value of the respective homogeneous mixture at the shortest wavelength.
Shown are six different mixture ratios (a) – (f) of haematite and goethite by volume.

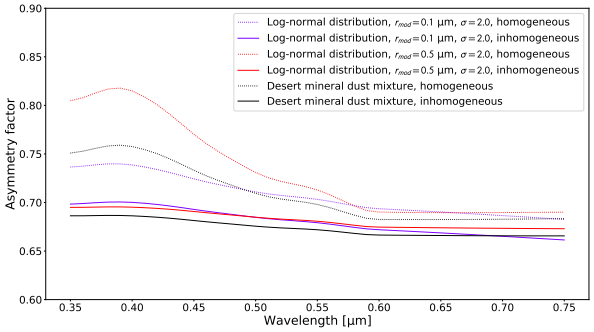

(a) Haematite 2%, goethite 0%

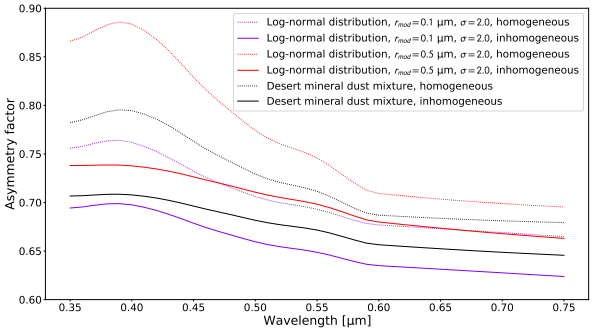

(b) Haematite 6%, goethite 0%

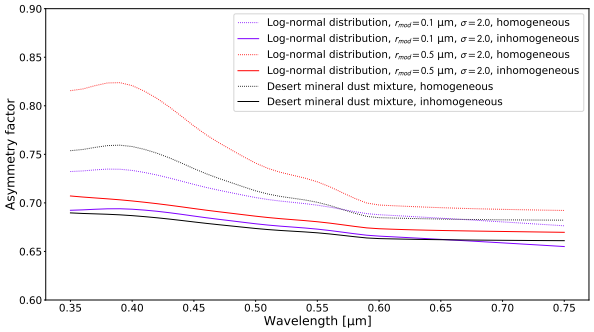

(c) Haematite 2%, goethite 3%

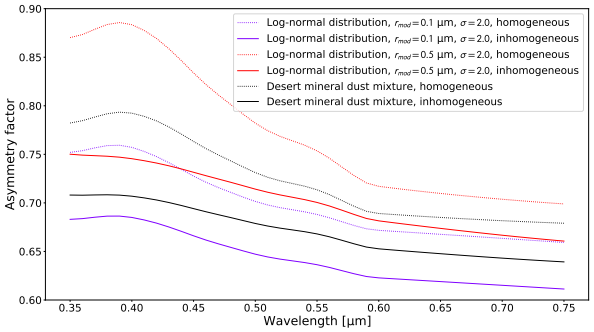

(d) Haematite 6%, goethite 3%

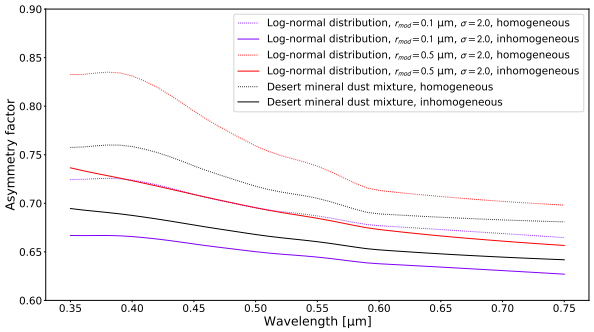

(e) Haematite 2%, goethite 9%

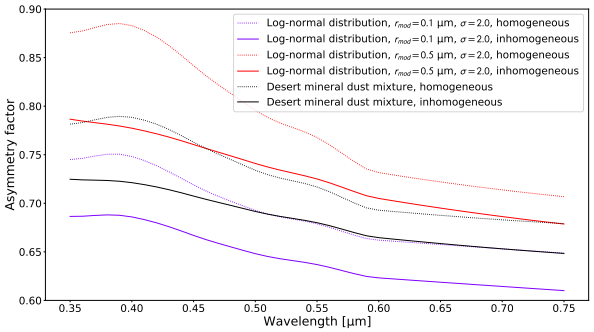

(f) Haematite 6%, goethite 9%

Figure 4.16: Asymmetry factor comparison for shapes A–F. Shown is the wavelength dependent asymmetry factor of log-normal distributions with different modal radii (colours) and a desert mineral dust mixture (black). Homogeneous particles are shown as dotted lines, inhomogeneous particles as solid lines.
Shown are six different mixture ratios (a) – (f) of haematite and goethite by volume.

4.4. Summary of results

Four optical properties (extinction efficiency, single scattering albedo, absorption efficiency and asymmetry factor) were calculated for more than 20000 particles of six different shapes. Additionally, four optical properties (extinction coefficient, single scattering albedeo, absorption coefficient and asymmetry factor) of particle ensembles based on the calculated single particles were calculated. While the effects of the internal structure can not be summarised or described easily (see Tables 4.2 to 4.5 and Figures 4.5 to 4.12), several trends could be observed.

The effect of iron oxide's inclusion locations was small compared to the difference of the internal structure's effect for all calculated optical properties, except the extinction efficiency, where the effects were of the same order of magnitude for the lower refractive index of haematite. The spatial resolution of 11 dipoles/λ was sufficient. Additional increases in resolution showed negligible changes compared to the mixture type. The internal structure had an effect on all single particle optical properties, especially on absorption efficiency, but the effect was less pronounced for the extinction efficiency. For particle ensembles, the internal structure had a strong effect on the single scattering albedo and absorption coefficient, but little effect on the extinction coefficient.

5. Discussion

A particle's internal structure has an effect on its optical properties. While this can be easily seen qualitatively, a quantitative description is not trivial to achieve. The strength of the effect depends not only on size parameter, but also on inclusion volume and refractive index and shows differences for each individual optical property.

5.1. Sensitivity to simulation parameters

The effect of spatial resolution and the solver's residual error ϵ are negligible compared to variations of the refractive indices, inclusion ratios and inclusion strategy within the envelope of used values. This may be different for other DDA simulations, but for the presented results, the trade-off between computation time and accuracy is acceptable. The rule of thumb for the spatial resolution is that at least 10 dipoles per wavelength times magnitude of the refractive index are recommended to achieve a cross-section accuracy of several percent [48]. This rule is for small size parameters. At higher size parameters, $x > 10$, the error increases with the magnitude of the refractive index. Increasing the spatial resolution without smoothing resulted in sub-percent changes in cross-sections, see Figure 4.4.

Increasing the numerical accuracy by setting ϵ to 6 instead of 3 would have approximately doubled the computation time (Figure 4.1c), while increasing the spatial resolution would have had an even stronger effect on computation time, see Table 4.1.

The effect of inclusion location on the optical properties is more pronounced, but the inclusion strategy still dominates, see Figures 4.2 and 4.3. The effect is diminished when averaging over sizes or shapes, e.g. when using particle ensembles.

5.2. Single particle properties

There is a difference between homogeneous and inhomogeneous inclusion strategies for all calculated optical properties. For the extinction efficiency, several effects can be seen for the heterogeneous mixture compared to the homogeneous case:

1. a reduction of the maximum extinction efficiency, in the range of -2% to -16%, depending on particle shape and mixture

2. a shift of size parameter for the maximum value – on average, the maximum is reached at smaller size parameters for the lower refractive index of haematite, and at larger size parameters for the higher refractive index

3. a convergence of extinction efficiencies for larger particle sizes independent of refractive index or homogeneity

The reduction in the maximum value for the heterogeneous mixture can also be seen for the absorption efficiency, single scattering albedo and the asymmetry factor. For these properties an interesting pattern can be observed: In the heterogeneous mixture these properties converge for the different refractive indices starting at size parameters of ≈ 15. This effect cannot be seen for homogeneous particles in the studied range of size parameters.

A possible explanation can be found in [49], where the product of κx is examined, where κ is the imaginary part of the refractive index and x is the (homogeneous, spherical) particle's size parameter. For very small particles, the single scattering albedo is approximately zero and increases until it reaches a maximum at a size parameter of approximately 5, after which the SSA decreases until at $\kappa x \approx 1$, where it reaches a near-constant value. This plateau is caused by a skin effect, where all of the light entering the particle is absorbed. This can be seen in Figure 4.7, where the plateau is reached at smaller size parameters for the higher imaginary part of the refractive index. Note, that the size parameter of the host particle is not relevant for this effect in the inhomogeneous case. It is the size parameter of the spherical inclusions that is relevant. A 1% spherical inclusion corresponds to a particle with a size parameter of ≈ 0.215 of the host particle's. For a single inclusion the product $\kappa x = 1$ is reached for a size parameter $x \approx 23$ for the smaller imaginary part of haematite of $\kappa = 0.2$. For size parameter $x \approx 15$, this product is already $\kappa x \approx 0.65$. This is in agreement with Figures 4.7, 4.9 and 4.11. For the higher refractive index this convergence is reached at lower size parameters, see Figure 4.9 where saturation can be seen at size parameters starting at 4–5.

For the homogeneous mixture, the imaginary part of the refractive index is diluted, i.e. averaged over the particle's whole volume, so the SSA's independence from κ and x is outside the inspected size range. For the absorption efficiency the effect can also be seen for the homogeneous mixture. In Figure 4.9b, for the larger refractive index of haematite of $\kappa = 1.162$ saturation is reached at size parameters 10–15. This corresponds to $0.06\kappa x = 0.06 \cdot 1.162 \cdot 15 \approx 1.05$, which is in agreement with the explanation. For larger particles' size parameters the homogeneous mixture can result in an overestimation of the absorption efficiency by a factor of 4–5.

While [49] only describes this effect for the SSA and for the absorption efficiency, our results indicate that it might also be applicable for the asymmetry factor, which shows similar behaviour.

5.3. Particle ensembles

The differences in internal mixture strategy are also pronounced in the optical properties observed for particle ensembles. The effect was strong for the single scattering albedo, absorption coefficient and asymmetry factor, where the difference was large for all studied size distributions. The internal structure had the strongest effect on absorption for short wavelengths. A difference of a factor of two in absorption could be observed

compared to homogeneously mixed particles. This illustrates the importance of the internal structure for assessing the climate impact of dust. The extinction coefficient was largely unaffected by internal structure. The findings are in line with [9], where internal structure showed effects on the single scattering albedo, but the extinction efficiency was much less sensitive to inhomogeneities.

While the size range for the calculations were chosen for practical reasons, i.e. limited by available computational resources, it is expected that for larger size parameters the effect of the internal structure will be even more pronounced.

5.4. Refractive indices for haematite

The sets of refractive indices for haematite were chosen to correspond approximately to the lower and upper wavelength of visible light. For the calculation of the imaginary part of the refractive index the formula from [40] was used to weight the incident light's different polarizations, based on data from [43]. The weights used are interchanged compared to the source cited. The error introduced by using the wrong weights is on the order of 5%. The imaginary part not only shows a strong wavelength dependence, it also varies in the visible spectrum, for the same wavelength, by more than one order of magnitude, depending on data source [40]. Therefore, the error of 5% is negligible, but the results of this thesis should only be considered qualitatively. Because of this and the high amount of computational resources and time needed, the calculations were not repeated.

6. Summary, conclusion & outlook

6.1. Summary

In this thesis the effects of mineral dust inhomogeneities on optical properties were studied. This was done by placing spherical inclusions of iron oxides inside the model dust particle, resulting in a dataset of more than 700 particles (the combination of six shapes, nine inclusion volume combinations and thirteen sizes), which were used as input for DDA calculations. The optical properties of individual particles were then calculated using ADDA for a various shapes, refractive indices and size parameters, resulting in a dataset of multiple TB of size. Differences of the optical properties compared to a homogeneous mixture with the same average refractive index, but without internal structure could be observed for all studied properties, although the difference was small for the extinction efficiency. Additionally, a skin effect has been observed, where the incident radiation cannot fully penetrate the inclusions, which partially explains the differences between the different particle types.

Subsequently, the results for single particles were used with MOPSMAP to study the inhomogeneities' effects on the optical properties of particle ensembles. Again, considerable differences compared to the homogeneous mixture were observed for SSA, asymmetry factor and absorption coefficient. The observed differences were largest at small wavelengths, where the imaginary part of haematite's refractive index is large. At these wavelengths, absorption by inhomogeneous particles is significantly weaker than for corresponding ensembles of homogeneous particles. Similar to the single particles, the difference in extinction coefficient was small between mixture strategies.

6.2. Conclusion

The internal structure of aerosol particles does matter and has an effect on the optical properties. This has to be taken into account when modelling aerosols' effect on Earth's climate. Since our model particles are still a significant simplification of real dust and precise knowledge about dust is limited, this also means that the source and composition of atmospheric dust aerosols has to be studied further to provide a data basis for an accurate modelling of the aerosols' internal structure. The findings also have consequences for the inversion, where the micro-physical properties of aerosol particles are calculated from the measured optical properties. The inversion is made more difficult by adding additional degrees of freedom. Similar observations have been made in [9].

Even with this simple model of the particles' internal structure, the results are an improvement over the simulation of homogeneous particles and allow to estimate the

effect of the particles' internal structure on the optical properties. The effect of the internal structure is not easy to summarise. Even for the individual optical properties, both the magnitude and the sign of the change introduced by the internal structure depend on size parameter and refractive index of the inclusions, as can be seen in the figures and tables in Chapter 4.

While the calculations in this thesis were computationally resource intensive because of their comprehensiveness, the computations for a smaller dataset could be used to provide auxiliary error estimates, even when the composition and structure is not known exactly.

6.3. Outlook

Electron microscopic examination of dust particles have shown that iron oxides are evenly distributed in the particle agglomerate, but that the internal structure consists of a patterned arrangement of mineral grains and pores [10]. More realistic inclusion shapes can be achieved by Voronoi tessellation [11]. As more data on the composition and structure of mineral dust particles is collected, it would be interesting to create a more realistic model of such a particles. Additionally, it would be interesting to study the effect of further randomisation for the inclusion locations, e.g. to change the inclusion locations for each particle orientation, although this would mean no longer having a concrete particle, over which the orientation averaging would be applied. For spherical inclusions, the inclusion size could be varied, either by using a different constant relative volume per inclusion, or by randomising the number and sizes of inclusions, but keeping the total relative inclusion volume constant. Furthermore, other inclusion distributions could be considered, e.g. surface layers as opposed to deep inclusions.

6.3.1. MOPSMAP expansion

For the expansion of MOPSMAP, the optical properties of a wider range of size parameters should be calculated, so that larger particles can be simulated. Because the computational time increases non-linearly with the size parameter, the size dependency of the optical properties for larger particles could be examined for a single composition at various sizes, to see how far the step size between size parameters can be increased and the simulation resolution can be decreased while keeping the interpolation error acceptably small. Now that the inhomogeneities' effect on the optical properties of particle ensembles has been qualitatively assessed, the expansion of MOPSMAP data could be implemented using a set of more realistic, wavelength dependent refractive indices for all particle components.

6.3.2. Black carbon attachments

While the magnitude of mineral dust's effect on the Earth's radiation budget is uncertain, black carbon strongly absorbs solar radiation and has a warming effect [50, 51]. Future extensions to these results could include attaching a black carbon surface coating to a

host particle from our study and examining whether the internal structure still remains relevant, and if the simulation can be split into individual simulations of attachment and host particle.

Bibliography

[1] Boucher, O. et al. 'Clouds and Aerosols'. In: *Climate Change 2013: The Physical Science Basis. Contribution of Working Group I to the Fifth Assessment Report of the Intergovernmental Panel on Climate Change*. Ed. by T. Stocker et al. Cambridge, United Kingdom and New York, NY, USA: Cambridge University Press, 2013, pp. 571–658. ISBN: ISBN 978-1-107-66182-0. DOI: 10.1017/CBO9781107415324.016.

[2] Gonzi, S. et al. 'Clear-Sky Aerosol Radiative Forcing Effects Based on Multi-Site AERONET Observations over Europe'. In: *Meteorology and Atmospheric Physics* 96.3-4 (June 2007), pp. 277–291. ISSN: 0177-7971, 1436-5065. DOI: 10.1007/s00703-006-0212-9.

[3] Myhre, G. et al. 'Anthropogenic and Natural Radiative Forcing'. In: *Climate Change 2013: The Physical Science Basis. Contribution of Working Group I to the Fifth Assessment Report of the Intergovernmental Panel on Climate Change*. Ed. by T. Stocker et al. Cambridge, United Kingdom and New York, NY, USA: Cambridge University Press, 2013, pp. 659–740. ISBN: ISBN 978-1-107-66182-0. DOI: 10.1017/CBO9781107415324.018.

[4] Kok, J. F. et al. 'Smaller Desert Dust Cooling Effect Estimated from Analysis of Dust Size and Abundance'. In: *Nature Geoscience* 10.4 (Apr. 2017), pp. 274–278. ISSN: 1752-0894, 1752-0908. DOI: 10.1038/ngeo2912.

[5] Sokolik, I. N. and Toon, O. B. 'Direct Radiative Forcing by Anthropogenic Airborne Mineral Aerosols'. In: *Nature* 381.6584 (1996), pp. 681–683. DOI: 10.1038/381681a0.

[6] Gasteiger, J. et al. 'Modelling Lidar-Relevant Optical Properties of Complex Mineral Dust Aerosols'. In: *Tellus B: Chemical and Physical Meteorology* 63.4 (Jan. 2011), pp. 725–741. ISSN: 1600-0889. DOI: 10.1111/j.1600-0889.2011.00559.x.

[7] Balkanski, Y. et al. 'Reevaluation of Mineral Aerosol Radiative Forcings Suggests a Better Agreement with Satellite and AERONET Data'. In: *Atmospheric Chemistry and Physics* 7.1 (2007), pp. 81–95. DOI: 10.5194/acp-7-81-2007.

[8] Kandler, K. et al. 'Electron Microscopy of Particles Collected at Praia, Cape Verde, during the Saharan Mineral Dust Experiment: Particle Chemistry, Shape, Mixing State and Complex Refractive Index'. In: *Tellus B: Chemical and Physical Meteorology* 63.4 (2011), pp. 475–496. DOI: 10.1111/j.1600-0889.2011.00550.x.

[9] Kahnert, M. 'Modelling Radiometric Properties of Inhomogeneous Mineral Dust Particles: Applicability and Limitations of Effective Medium Theories'. In: *Journal of Quantitative Spectroscopy and Radiative Transfer* 152 (Feb. 2015), pp. 16–27. ISSN: 00224073. DOI: 10.1016/j.jqsrt.2014.10.025.

[10] Jeong, G. Y. and Nousiainen, T. 'TEM Analysis of the Internal Structures and Mineralogy of Asian Dust Particles and the Implications for Optical Modeling'. In: *Atmospheric Chemistry and Physics* 14.14 (July 2014), pp. 7233–7254. ISSN: 1680-7316. DOI: 10.5194/acp-14-7233-2014.

[11] Kemppinen, O., Nousiainen, T. and Jeong, G. Y. 'Effects of Dust Particle Internal Structure on Light Scattering'. In: *Atmospheric Chemistry and Physics* 15.20 (Oct. 2015), pp. 12011–12027. ISSN: 1680-7324. DOI: 10.5194/acp-15-12011-2015.

[12] Kahnert, M., Nousiainen, T. and Räisänen, P. 'Mie Simulations as an Error Source in Mineral Aerosol Radiative Forcing Calculations'. In: *Quarterly Journal of the Royal Meteorological Society* 133.623 (Jan. 2007), pp. 299–307. DOI: 10.1002/qj.40.

[13] Dubovik, O. et al. 'Application of Spheroid Models to Account for Aerosol Particle Nonsphericity in Remote Sensing of Desert Dust'. In: *J. Geophys. Res.* 111 (2006), p. D11208. DOI: 10.1029/2005JD006619.

[14] Dubovik, O. et al. 'Non-Spherical Aerosol Retrieval Method Employing Light Scattering by Spheroids'. In: *Geophysical Research Letters* 29.10 (2002), pp. 54–1–54–4. DOI: 10.1029/2001gl014506.

[15] Kahn, R. et al. 'Sensitivity of Multiangle Remote Sensing Observations to Aerosol Sphericity'. In: *Journal of Geophysical Research: Atmospheres* 102.D14 (1997), pp. 16861–16870. DOI: 10.1029/96jd01934.

[16] Gasteiger, J. and Wiegner, M. 'MOPSMAP v1.0: A Versatile Tool for the Modeling of Aerosol Optical Properties'. In: *Geoscientific Model Development* 11.7 (July 2018), pp. 2739–2762. ISSN: 1991-9603. DOI: 10.5194/gmd-11-2739-2018.

[17] Lindqvist, H. et al. 'Single Scattering by Realistic, Inhomogeneous Mineral Dust Particles with Stereogrammetric Shapes'. In: *Atmospheric Chemistry and Physics* 14.1 (2014), pp. 143–157. DOI: 10.5194/acp-14-143-2014.

[18] Hulst, H. C. van de. *Light Scattering by Small Particles*. New York: Dover Publications, 1981. ISBN: 978-0-486-64228-4.

[19] Hinds, W. C. *Aerosol Technology: Properties, Behavior, and Measurement of Airborne Particles*. 2nd ed. New York: Wiley, 1999. ISBN: 978-0-471-19410-1.

[20] Seinfeld, J. H. and Pandis, S. N. *Atmospheric Chemistry and Physics: From Air Pollution to Climate Change*. Third edition. Hoboken, New Jersey: John Wiley & Sons, 2016. ISBN: 978-1-119-22117-3.

[21] Bohren, C. F. and Huffman, D. R. *Absorption and Scattering of Light by Small Particles*. Weinheim: Wiley-VCH, 2004. ISBN: 978-0-471-29340-8.

[22] Zender, C. S., Miller, R. L. L. and Tegen, I. 'Quantifying Mineral Dust Mass Budgets: Terminology, Constraints, and Current Estimates'. In: *Eos, Transactions American Geophysical Union* 85.48 (Nov. 2004), pp. 509–512. ISSN: 00963941. DOI: 10.1029/2004EO480002.

[23] Shao, Y. et al. 'Dust Cycle: An Emerging Core Theme in Earth System Science'. In: *Aeolian Research* 2.4 (Mar. 2011), pp. 181–204. ISSN: 18759637. DOI: 10.1016/j.aeolia.2011.02.001.

[24] Sokolik, I. N. et al. 'Introduction to Special Section: Outstanding Problems in Quantifying the Radiative Impacts of Mineral Dust'. In: *Journal of Geophysical Research: Atmospheres* 106.D16 (Aug. 2001), pp. 18015–18027. ISSN: 01480227. DOI: 10.1029/2000JD900498.

[25] Perlwitz, J., Tegen, I. and Miller, R. L. 'Interactive Soil Dust Aerosol Model in the GISS GCM: 1. Sensitivity of the Soil Dust Cycle to Radiative Properties of Soil Dust Aerosols'. In: *Journal of Geophysical Research: Atmospheres* 106.D16 (Aug. 2001), pp. 18167–18192. ISSN: 01480227. DOI: 10.1029/2000JD900668.

[26] Krueger, B. et al. 'Heterogeneous Chemistry of Individual Mineral Dust Particles from Different Dust Source Regions: The Importance of Particle Mineralogy'. In: *Atmospheric Environment* 38.36 (Nov. 2004), pp. 6253–6261. ISSN: 13522310. DOI: 10.1016/j.atmosenv.2004.07.010.

[27] Fitzgerald, E. et al. 'Comparison of the Mixing State of Long-Range Transported Asian and African Mineral Dust'. In: *Atmospheric Environment* 115 (Aug. 2015), pp. 19–25. ISSN: 13522310. DOI: 10.1016/j.atmosenv.2015.04.031.

[28] Marshall, S. F., Covert, D. S. and Charlson, R. J. 'Relationship between Asymmetry Parameter and Hemispheric Backscatter Ratio: Implications for Climate Forcing by Aerosols'. In: *Applied Optics* 34.27 (Sept. 1995), p. 6306. ISSN: 0003-6935, 1539-4522. DOI: 10.1364/AO.34.006306.

[29] Mie, G. 'Beiträge Zur Optik Trüber Medien, Speziell Kolloidaler Metallösungen'. In: *Annalen der Physik* 330.3 (1908), pp. 377–445. ISSN: 00033804, 15213889. DOI: 10.1002/andp.19083300302.

[30] Frezza, F., Mangini, F. and Tedeschi, N. 'Introduction to Electromagnetic Scattering: Tutorial'. In: *Journal of the Optical Society of America A* 35.1 (Jan. 2018), p. 163. ISSN: 1084-7529, 1520-8532. DOI: 10.1364/JOSAA.35.000163.

[31] Draine, B. T. and Flatau, P. J. 'Discrete-Dipole Approximation For Scattering Calculations'. In: *Journal of the Optical Society of America A* 11.4 (Apr. 1994), p. 1491. ISSN: 1084-7529, 1520-8532. DOI: 10.1364/JOSAA.11.001491.

[32] Waterman, P. 'Matrix Formulation of Electromagnetic Scattering'. In: *Proceedings of the IEEE* 53.8 (1965), pp. 805–812. ISSN: 0018-9219. DOI: 10.1109/PROC.1965.4058.

[33] Mishchenko, M. I., Travis, L. D. and Mackowski, D. W. 'T-Matrix Computations of Light Scattering by Nonspherical Particles: A Review'. In: *Journal of Quantitative Spectroscopy and Radiative Transfer* 55.5 (May 1996), pp. 535–575. ISSN: 00224073. DOI: 10.1016/0022-4073(96)00002-7.

[34] Mishchenko, M. I. and Travis, L. D. 'Capabilities and Limitations of a Current FORTRAN Implementation of the T-Matrix Method for Randomly Oriented, Rotationally Symmetric Scatterers'. In: *Journal of Quantitative Spectroscopy and Radiative Transfer* 60.3 (Sept. 1998), pp. 309–324. ISSN: 00224073. DOI: 10.1016/S0022-4073(98)00008-9.

[35] Mishchenko, M. I. 'Calculation of the Amplitude Matrix for a Nonspherical Particle in a Fixed Orientation'. In: *Applied Optics* 39.6 (Feb. 2000), p. 1026. ISSN: 0003-6935, 1539-4522. DOI: 10.1364/AO.39.001026.

[36] Purcell, E. M. and Pennypacker, C. R. 'Scattering and Absorption of Light by Nonspherical Dielectric Grains'. In: *The Astrophysical Journal* 186 (Dec. 1973), p. 705. ISSN: 0004-637X, 1538-4357. DOI: 10.1086/152538.

[37] Draine, B. T. 'The Discrete-Dipole Approximation and Its Application to Interstellar Graphite Grains'. In: *The Astrophysical Journal* 333 (Oct. 1988), p. 848. ISSN: 0004-637X, 1538-4357. DOI: 10.1086/166795.

[38] Yurkin, M. A. and Hoekstra, A. G. 'The Discrete Dipole Approximation: An Overview and Recent Developments'. In: *Journal of Quantitative Spectroscopy and Radiative Transfer* 106.1-3 (July 2007), pp. 558–589. ISSN: 00224073. DOI: 10.1016/j.jqsrt.2007.01.034.

[39] Yurkin, M. A., Min, M. and Hoekstra, A. G. 'Application of the Discrete Dipole Approximation to Very Large Refractive Indices: Filtered Coupled Dipoles Revived'. In: *Physical Review E* 82.3 (Sept. 2010), p. 036703. ISSN: 1539-3755, 1550-2376. DOI: 10.1103/PhysRevE.82.036703.

[40] Zhang, X. L. et al. 'What Is the Real Role of Iron Oxides in the Optical Properties of Dust Aerosols?' In: *Atmospheric Chemistry and Physics* 15.21 (Nov. 2015), pp. 12159–12177. ISSN: 1680-7324. DOI: 10.5194/acp-15-12159-2015.

[41] Formenti, P. et al. 'Dominance of Goethite over Hematite in Iron Oxides of Mineral Dust from Western Africa: Quantitative Partitioning by X-Ray Absorption Spectroscopy'. In: *Journal of Geophysical Research: Atmospheres* 119.22 (Nov. 2014), pp. 12, 740–12, 754. ISSN: 2169897X. DOI: 10.1002/2014JD021668.

[42] Kandler, K. et al. 'Size Distribution, Mass Concentration, Chemical and Mineralogical Composition and Derived Optical Parameters of the Boundary Layer Aerosol at Tinfou, Morocco, during SAMUM 2006'. In: *Tellus B: Chemical and Physical Meteorology* 61.1 (Jan. 2009), pp. 32–50. ISSN: 1600-0889. DOI: 10.1111/j.1600-0889.2008.00385.x.

[43] Querry, M. *Optical Constants*. Contractor report, CRDC-CR, US Army Armament, Munitions & Chemical Research, Development & Engineering Center, Aberdeen Proving Ground, MD, 1985.

[44] Bedidi, A. and Cervelle, B. 'Light Scattering by Spherical Particles with Hematite and Goethitelike Optical Properties: Effect of Water Impregnation'. en. In: *Journal of Geophysical Research: Solid Earth* 98.B7 (July 1993), pp. 11941–11952. ISSN: 01480227. DOI: 10.1029/93JB00188.

[45] OEIS Foundation Inc., The On-Line Encyclopedia of Integer Sequences. *A000605*. http://oeis.org/A000605. 2019.

[46] Hess, M., Koepke, P. and Schult, I. 'Optical Properties of Aerosols and Clouds: The Software Package OPAC'. In: *Bulletin of the American Meteorological Society* 79.5 (May 1998), pp. 831–844. ISSN: 0003-0007. DOI: 10.1175/1520-0477(1998)079<0831:OPOAAC>2.0.CO;2.

[47] Yurkin, M. A. and Hoekstra, A. G. *User Manual for the Discrete Dipole Approximation Code ADDA 1.3b4*. 2014.

[48] Yurkin, M. A. and Hoekstra, A. G. 'The Discrete-Dipole-Approximation Code ADDA: Capabilities and Known Limitations'. In: *Journal of Quantitative Spectroscopy and Radiative Transfer* 112.13 (2011), pp. 2234–2247. DOI: 10.1016/j.jqsrt.2011.01.031.

[49] Moosmüller, H. and Sorensen, C. 'Small and Large Particle Limits of Single Scattering Albedo for Homogeneous, Spherical Particles'. In: *Journal of Quantitative Spectroscopy and Radiative Transfer* 204 (Jan. 2018), pp. 250–255. ISSN: 00224073. DOI: 10.1016/j.jqsrt.2017.09.029.

[50] Bond, T. C. and Bergstrom, R. W. 'Light Absorption by Carbonaceous Particles: An Investigative Review'. In: *Aerosol Science and Technology* 40.1 (Jan. 2006), pp. 27–67. ISSN: 0278-6826, 1521-7388. DOI: 10.1080/02786820500421521.

[51] Bond, T. C. et al. 'Bounding the Role of Black Carbon in the Climate System: A Scientific Assessment: BLACK CARBON IN THE CLIMATE SYSTEM'. In: *Journal of Geophysical Research: Atmospheres* 118.11 (June 2013), pp. 5380–5552. ISSN: 2169897X. DOI: 10.1002/jgrd.50171.

List of Figures

List of Tables

A. ADDA options

For a detailed explanation of the command line parameters see [47]. For a list of relevant non-default options used see Table A.1.

Explanation	Parameter	Value
Particle orientation Euler angles α, β and γ	-orient	0, β γ, see Section 3.5
Mueller matrix integration over azimuthal angle	-phi_integr	1
Refractive indices of materials	-m	variable, see Section 4.1.1
Store the resulting Mueller scattering matrices	-store_scat_grid	N/A
Stopping criterion for the iterative solver	-eps	varies
Particle's volume-equivalent size parameter	-eq_rad	varies
Polarizability calculation method	-pol	fcd
Interaction term	-int	fcd

Table A.1. ADDA command line parameters
ADDA command line parameters. Rotation over α corresponds to a rotation of the scattering plane, which was done within a single DDA calculation. The iterative solver stops when the relative norm of the residuals falls below $10^{-\text{eps}}$

B. Optical properties for the remaining particle shapes

In this appendix the optical properties (extinction efficiency, single scattering albedo, absorption efficiency and asymmetry factor) between mixtures types are shown for the five remaining particle shapes A, B, C, E and F.

B.1. Extinction efficiency

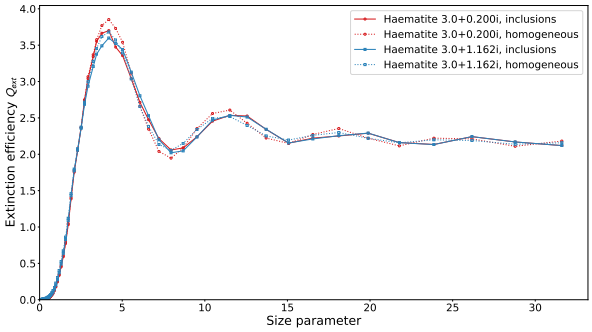

(a) Haematite 2%, goethite 0%

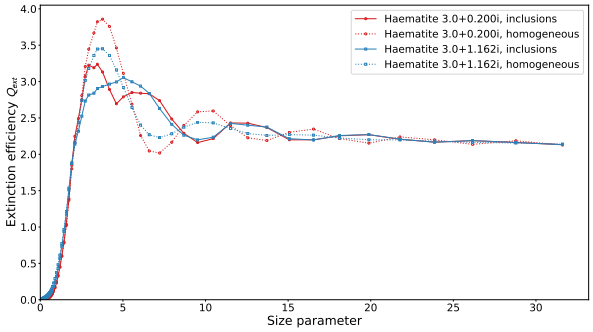

(b) Haematite 6%, goethite 0%

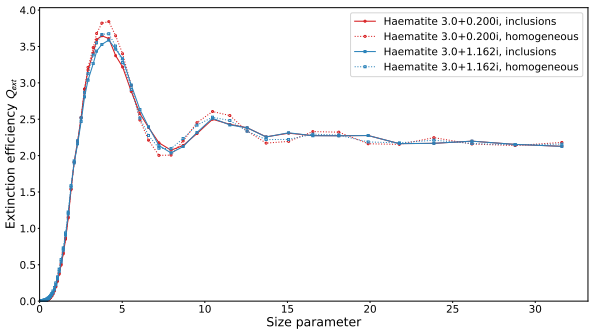

(c) Haematite 2%, goethite 3%

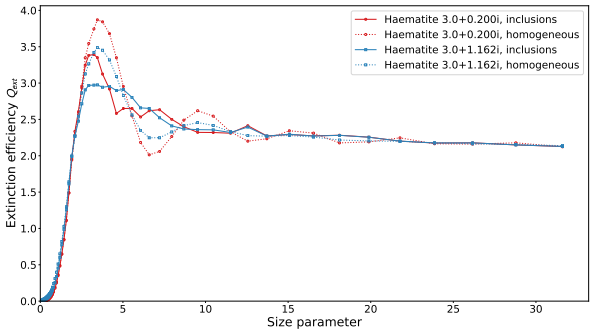

(d) Haematite 6%, goethite 3%

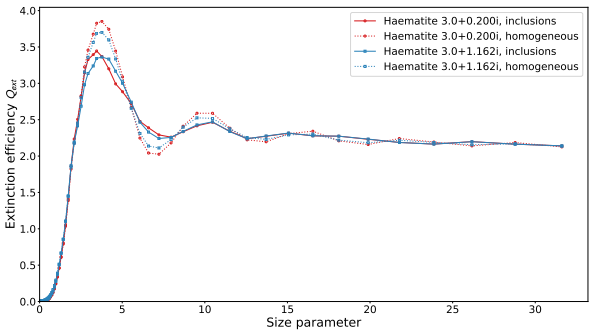

(e) Haematite 2%, goethite 9%

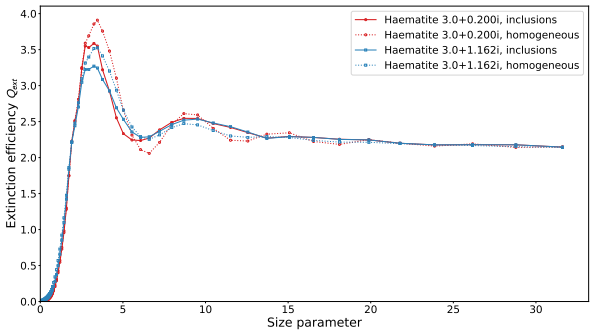

(f) Haematite 6%, goethite 9%

Figure B.1: Extinction efficiency comparison for shape A. Shown is the extinction efficiency for a range of size parameters. The colours indicate the refractive index of haematite (red: $3.0 + 0.2i$, blue: $3.0 + 1.162i$), corresponding to different wavelengths, while the line style indicates the mixture strategy: Inhomogeneous mixture (inclusions of one percent volume spheres each) are shown as solid lines, the homogeneous mixtures shown as dotted lines. Shown are six different mixture ratios (a) – (f) of haematite and goethite by volume.

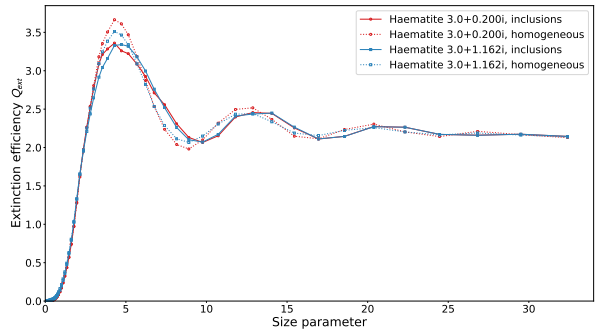

(a) Haematite 2%, goethite 0%

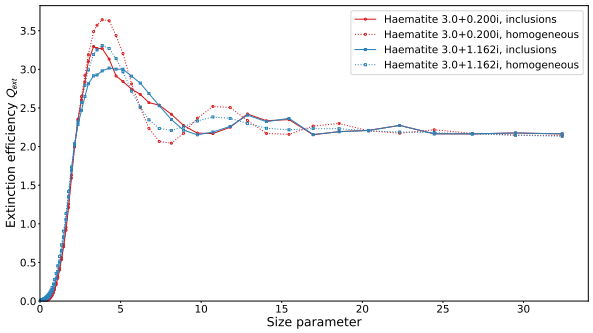

(b) Haematite 6%, goethite 0%

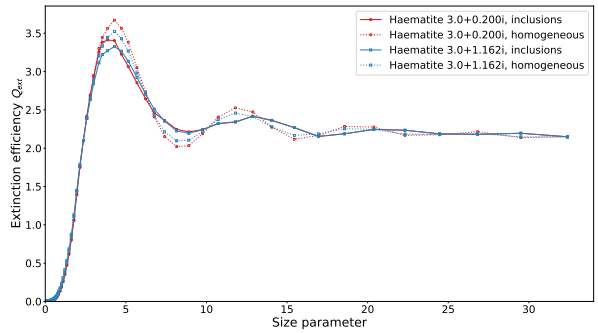

(c) Haematite 2%, goethite 3%

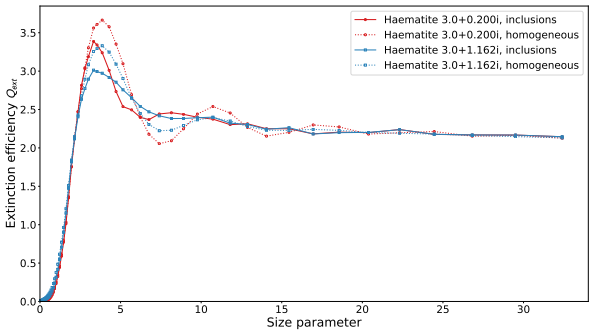

(d) Haematite 6%, goethite 3%

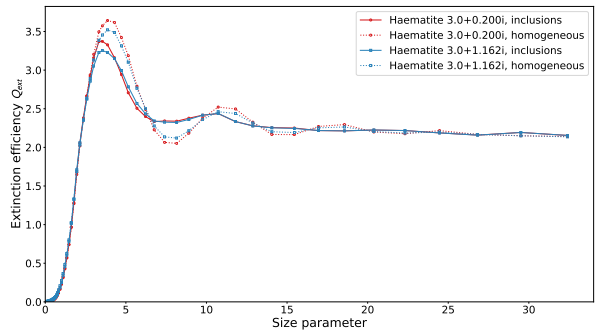

(e) Haematite 2%, goethite 9%

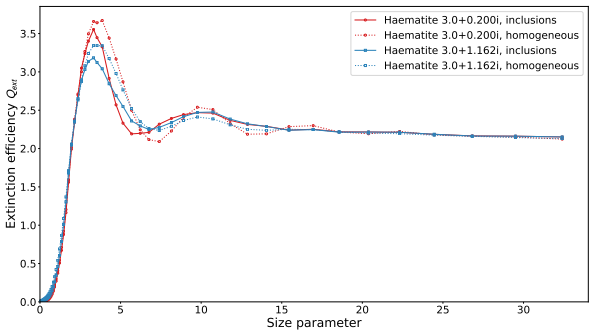

(f) Haematite 6%, goethite 9%

Figure B.2: Extinction efficiency comparison for shape B. Shown is the extinction efficiency for a range of size parameters. The colours indicate the refractive index of haematite (red: $3.0 + 0.2i$, blue: $3.0 + 1.162i$), corresponding to different wavelengths, while the line style indicates the mixture strategy: Inhomogeneous mixture (inclusions of one percent volume spheres each) are shown as solid lines, the homogeneous mixtures shown as dotted lines. Shown are six different mixture ratios (a) – (f) of haematite and goethite by volume.

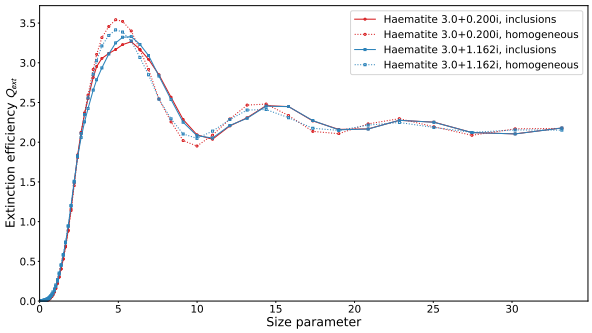

(a) Haematite 2%, goethite 0%

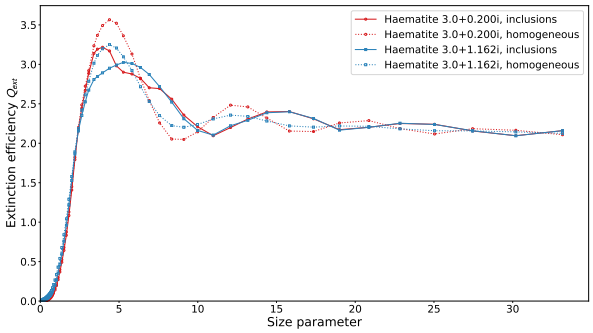

(b) Haematite 6%, goethite 0%

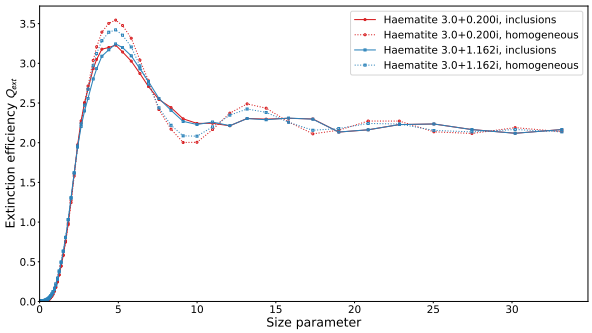

(c) Haematite 2%, goethite 3%

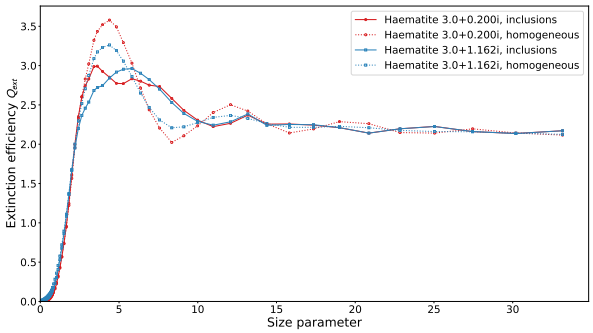

(d) Haematite 6%, goethite 3%

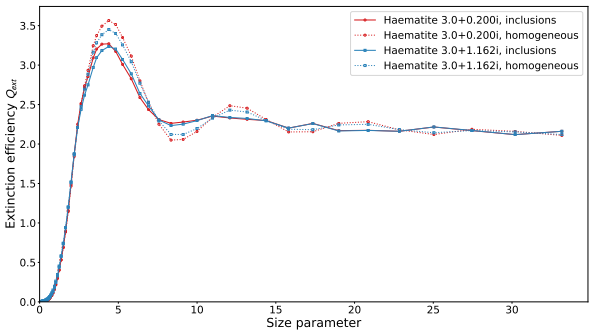

(e) Haematite 2%, goethite 9%

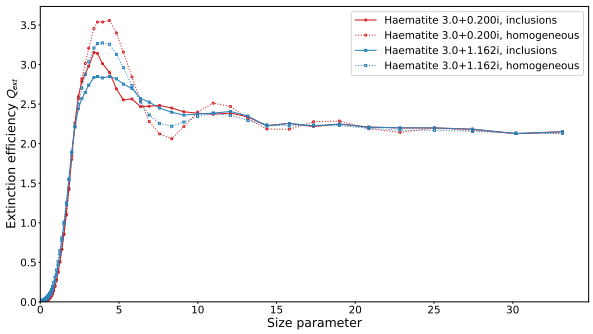

(f) Haematite 6%, goethite 9%

Figure B.3: Extinction efficiency comparison for shape C. Shown is the extinction efficiency for a range of size parameters. The colours indicate the refractive index of haematite (red: $3.0 + 0.2i$, blue: $3.0 + 1.162i$), corresponding to different wavelengths, while the line style indicates the mixture strategy: Inhomogeneous mixture (inclusions of one percent volume spheres each) are shown as solid lines, the homogeneous mixtures shown as dotted lines. Shown are six different mixture ratios (a) – (f) of haematite and goethite by volume.

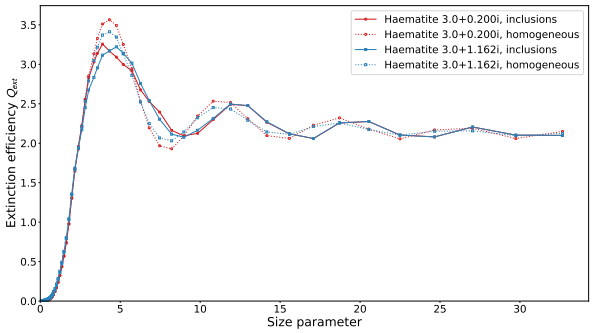

(a) Haematite 2%, goethite 0%

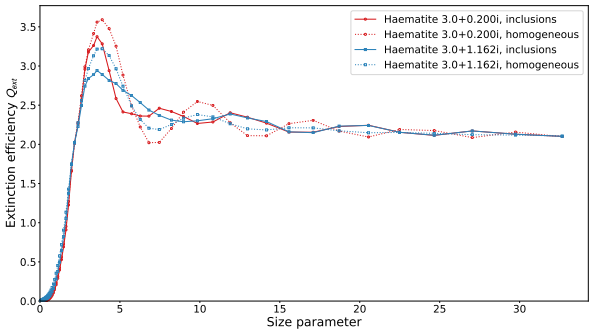

(b) Haematite 6%, goethite 0%

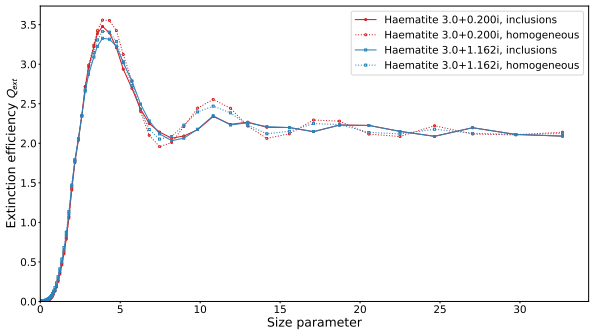

(c) Haematite 2%, goethite 3%

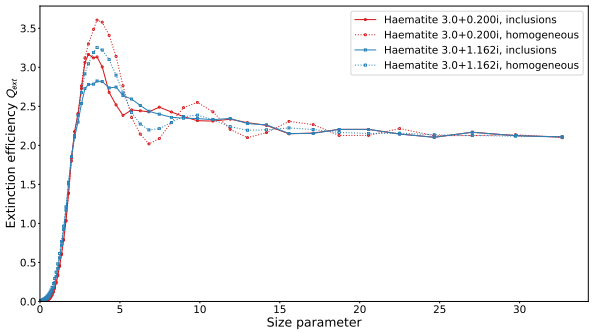

(d) Haematite 6%, goethite 3%

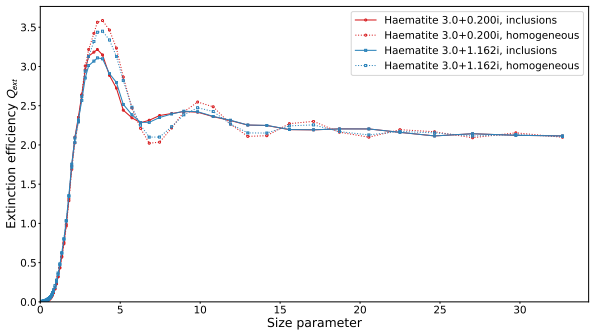

(e) Haematite 2%, goethite 9%

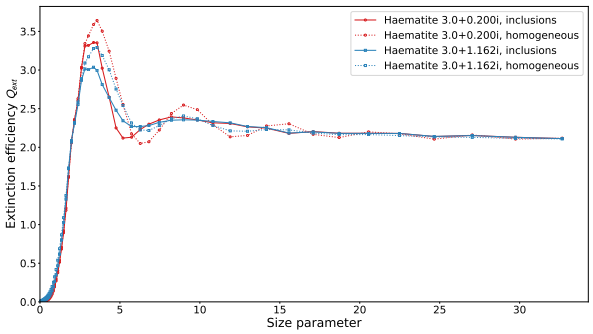

(f) Haematite 6%, goethite 9%

Figure B.4: Extinction efficiency comparison for shape E. Shown is the extinction efficiency for a range of size parameters. The colours indicate the refractive index of haematite (red: $3.0 + 0.2i$, blue: $3.0 + 1.162i$), corresponding to different wavelengths, while the line style indicates the mixture strategy: Inhomogeneous mixture (inclusions of one percent volume spheres each) are shown as solid lines, the homogeneous mixtures shown as dotted lines. Shown are six different mixture ratios (a) – (f) of haematite and goethite by volume.

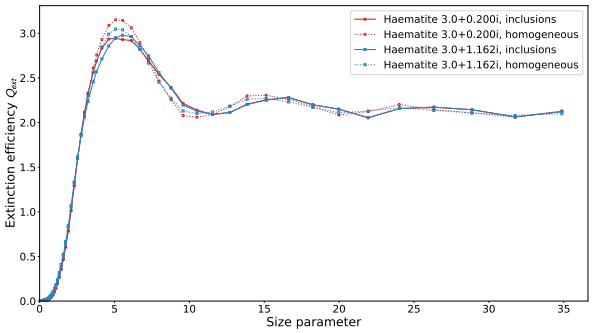

(a) Haematite 2%, goethite 0%

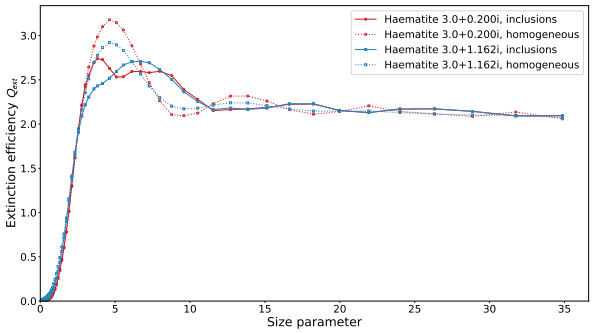

(b) Haematite 6%, goethite 0%

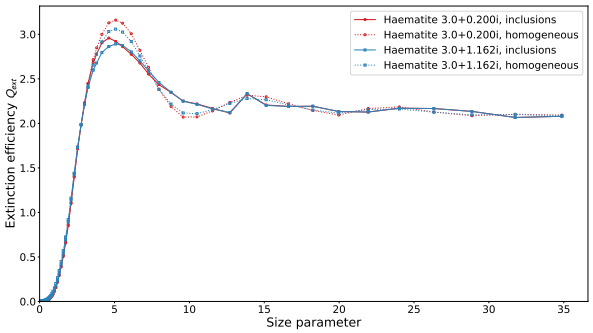

(c) Haematite 2%, goethite 3%

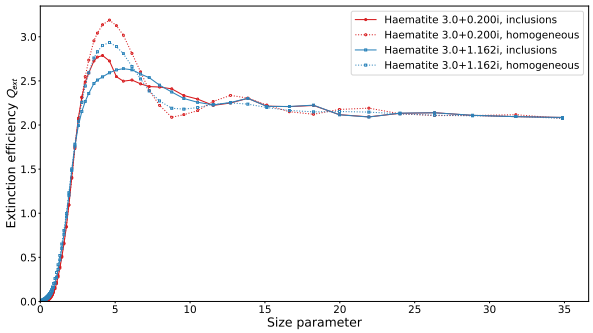

(d) Haematite 6%, goethite 3%

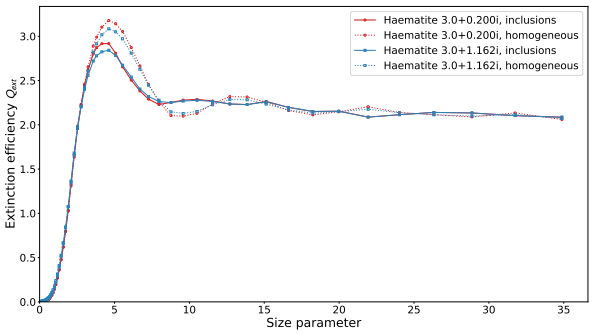

(e) Haematite 2%, goethite 9%

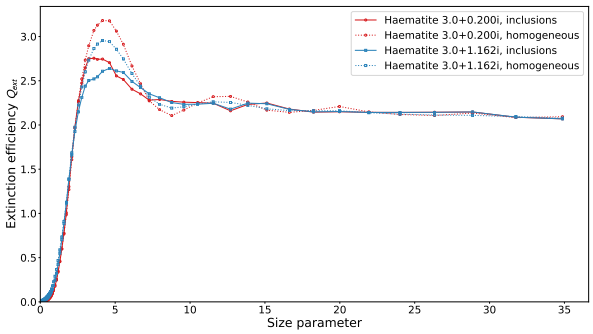

(f) Haematite 6%, goethite 9%

Figure B.5: Extinction efficiency comparison for shape F. Shown is the extinction efficiency for a range of size parameters. The colours indicate the refractive index of haematite (red: $3.0 + 0.2i$, blue: $3.0 + 1.162i$), corresponding to different wavelengths, while the line style indicates the mixture strategy: Inhomogeneous mixture (inclusions of one percent volume spheres each) are shown as solid lines, the homogeneous mixtures shown as dotted lines. Shown are six different mixture ratios (a) – (f) of haematite and goethite by volume.

B.2. Single scattering albedo

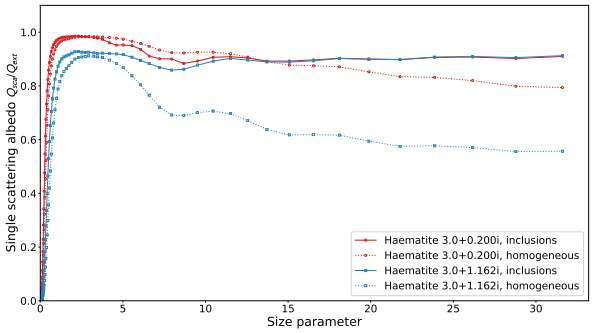

(a) Haematite 2%, goethite 0%

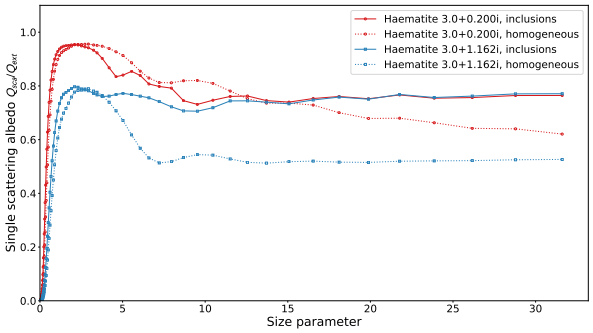

(b) Haematite 6%, goethite 0%

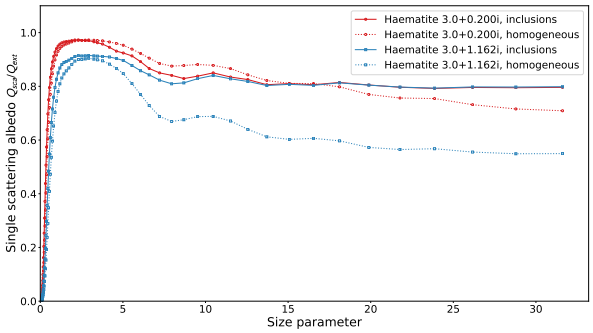

(c) Haematite 2%, goethite 3%

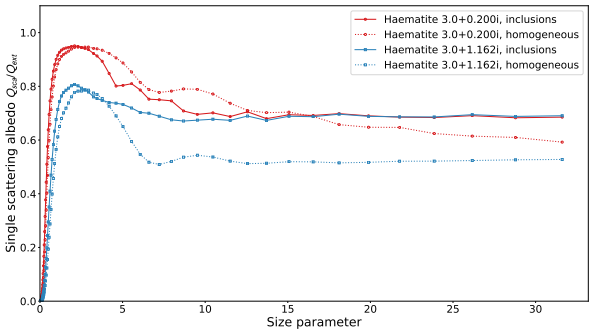

(d) Haematite 6%, goethite 3%

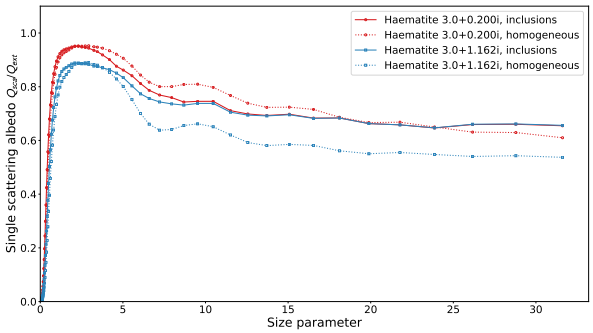

(e) Haematite 2%, goethite 9%

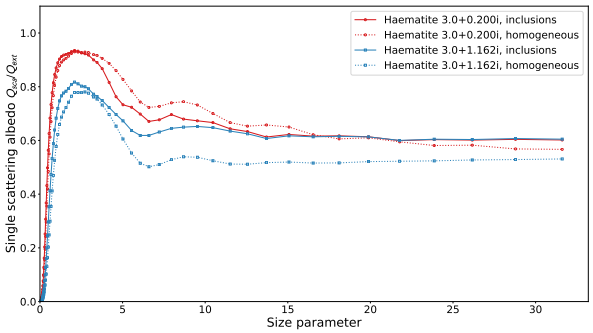

(f) Haematite 6%, goethite 9%

Figure B.6: Single scattering albedo comparison for shape A. Shown is the single scattering albedo for a range of size parameters. The colours indicate the refractive index of haematite (red: $3.0 + 0.2i$, blue: $3.0 + 1.162i$), corresponding to different wavelengths, while the line style indicates the mixture strategy: Inhomogeneous mixture (inclusions of one percent volume spheres each) are shown as solid lines, the homogeneous mixtures shown as dotted lines. Shown are six different mixture ratios (a) – (f) of haematite and goethite by volume.

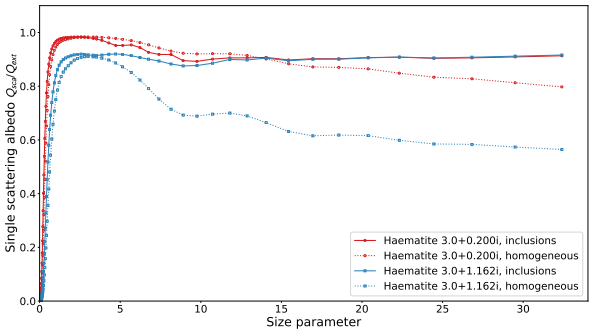

(a) Haematite 2%, goethite 0%

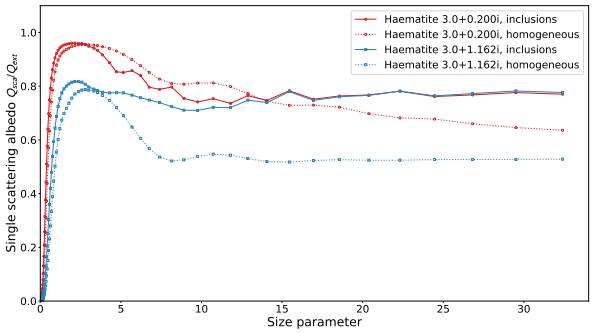

(b) Haematite 6%, goethite 0%

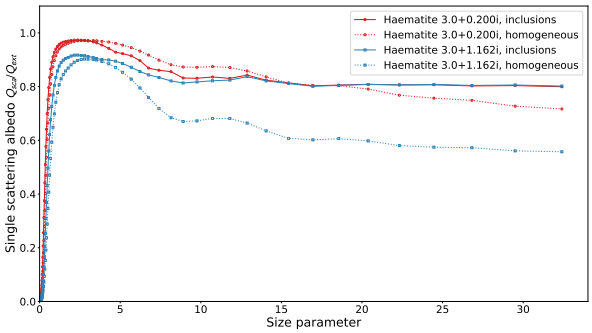

(c) Haematite 2%, goethite 3%

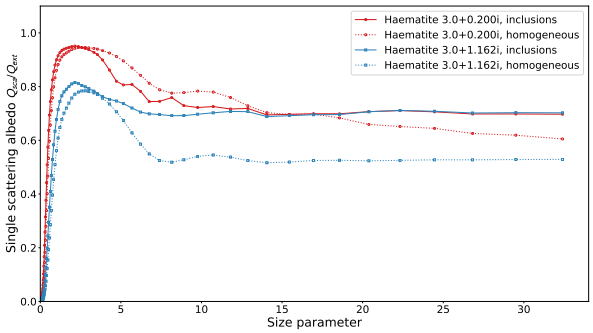

(d) Haematite 6%, goethite 3%

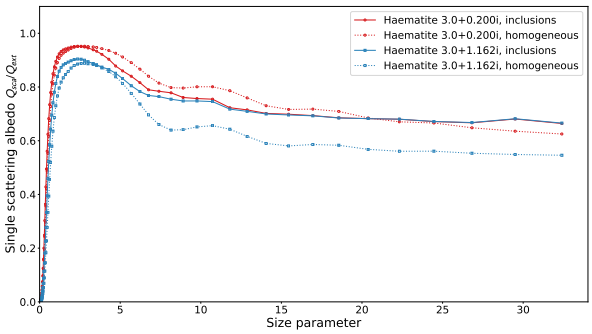

(e) Haematite 2%, goethite 9%

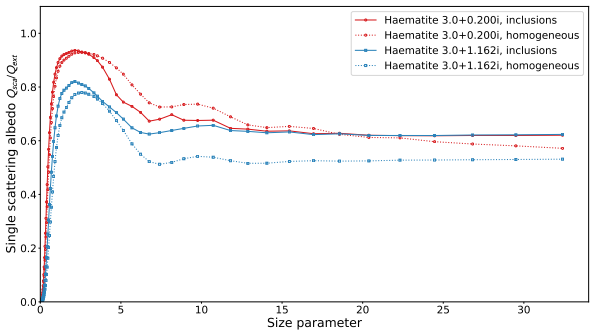

(f) Haematite 6%, goethite 9%

Figure B.7: Single scattering albedo comparison for shape B. Shown is the single scattering albedo for a range of size parameters. The colours indicate the refractive index of haematite (red: $3.0+0.2i$, blue: $3.0+1.162i$), corresponding to different wavelengths, while the line style indicates the mixture strategy: Inhomogeneous mixture (inclusions of one percent volume spheres each) are shown as solid lines, the homogeneous mixtures shown as dotted lines. Shown are six different mixture ratios (a) – (f) of haematite and goethite by volume.

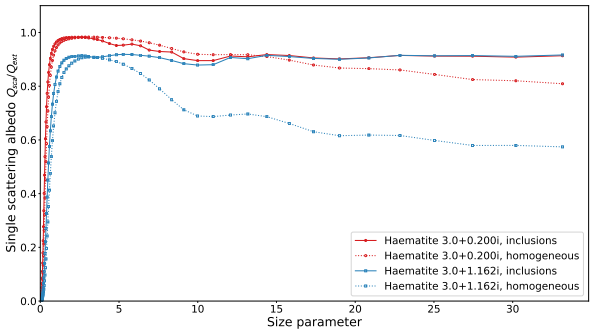

(a) Haematite 2%, goethite 0%

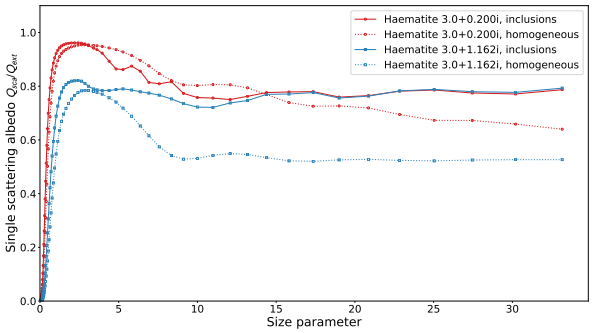

(b) Haematite 6%, goethite 0%

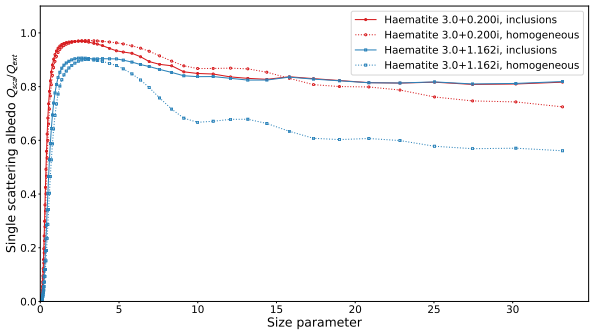

(c) Haematite 2%, goethite 3%

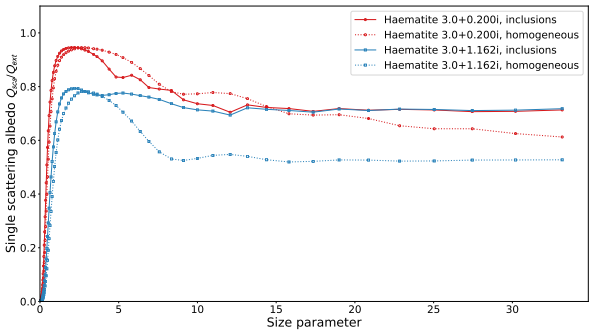

(d) Haematite 6%, goethite 3%

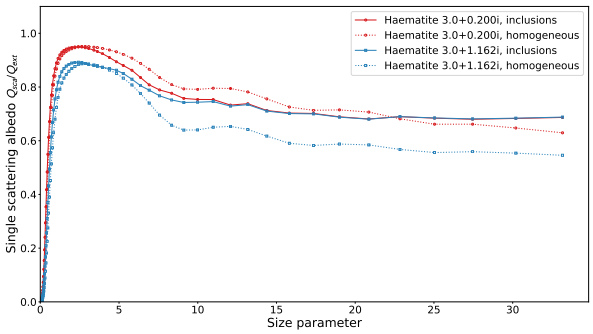

(e) Haematite 2%, goethite 9%

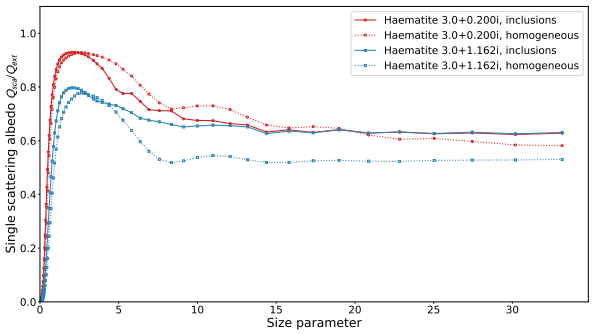

(f) Haematite 6%, goethite 9%

Figure B.8: Single scattering albedo comparison for shape C. Shown is the single scattering albedo for a range of size parameters. The colours indicate the refractive index of haematite (red: $3.0 + 0.2i$, blue: $3.0 + 1.162i$), corresponding to different wavelengths, while the line style indicates the mixture strategy: Inhomogeneous mixture (inclusions of one percent volume spheres each) are shown as solid lines, the homogeneous mixtures shown as dotted lines. Shown are six different mixture ratios (a) – (f) of haematite and goethite by volume.

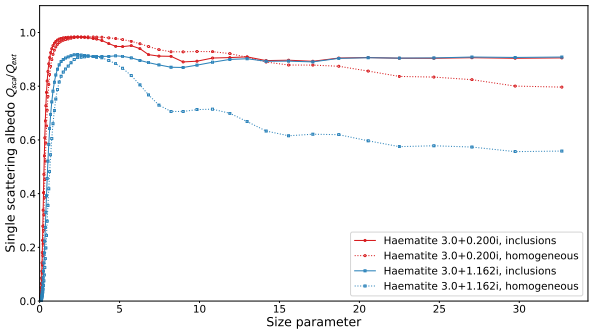

(a) Haematite 2%, goethite 0%

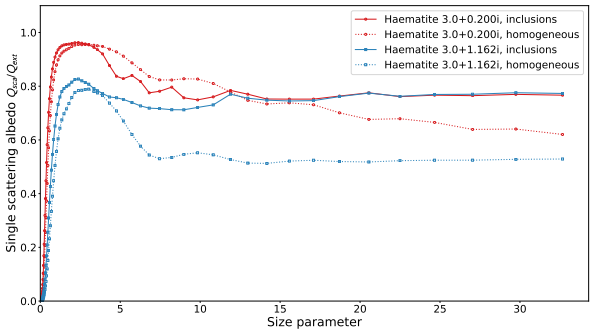

(b) Haematite 6%, goethite 0%

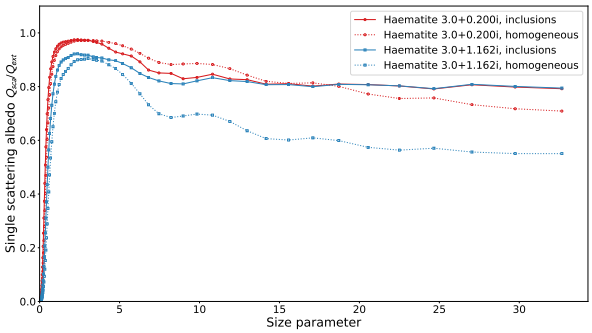

(c) Haematite 2%, goethite 3%

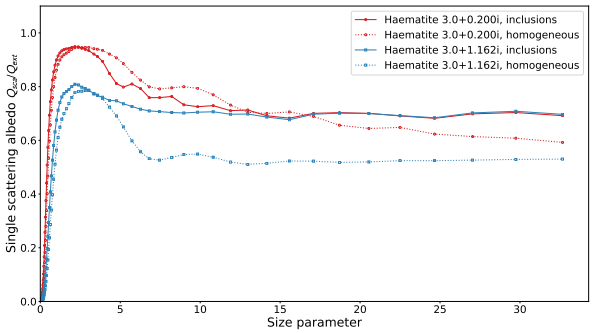

(d) Haematite 6%, goethite 3%

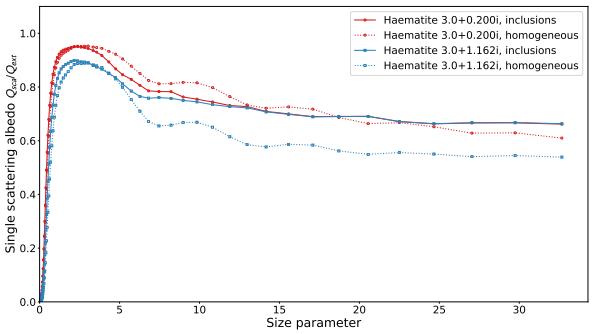

(e) Haematite 2%, goethite 9%

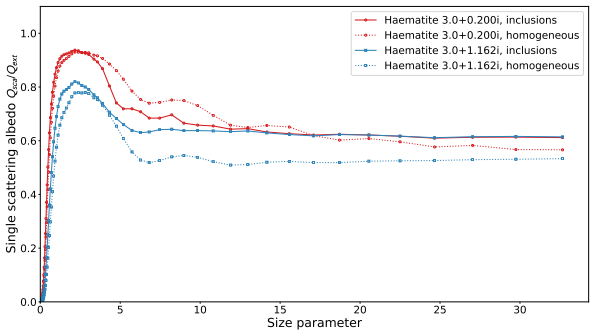

(f) Haematite 6%, goethite 9%

Figure B.9: Single scattering albedo comparison for shape E. Shown is the single scattering albedo for a range of size parameters. The colours indicate the refractive index of haematite (red: $3.0+0.2i$, blue: $3.0+1.162i$), corresponding to different wavelengths, while the line style indicates the mixture strategy: Inhomogeneous mixture (inclusions of one percent volume spheres each) are shown as solid lines, the homogeneous mixtures shown as dotted lines. Shown are six different mixture ratios (a) – (f) of haematite and goethite by volume.

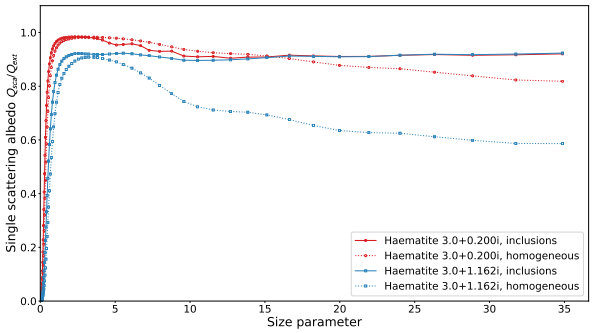

(a) Haematite 2%, goethite 0%

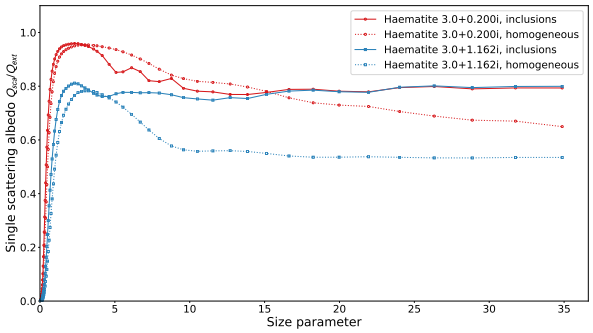

(b) Haematite 6%, goethite 0%

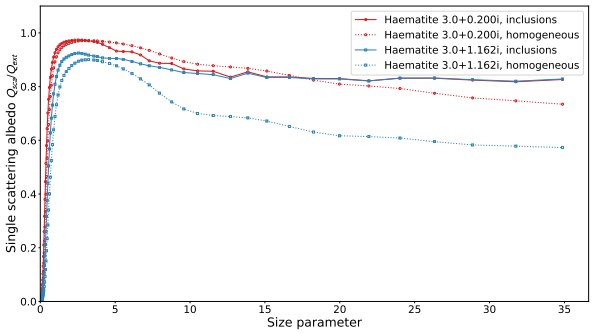

(c) Haematite 2%, goethite 3%

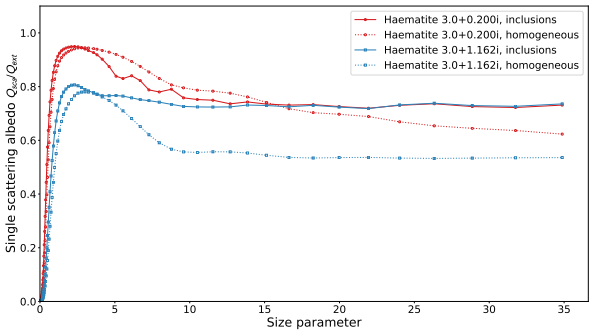

(d) Haematite 6%, goethite 3%

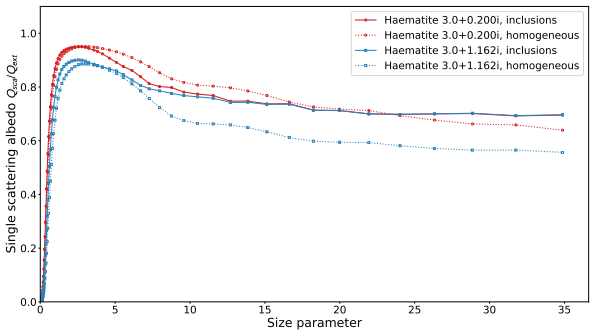

(e) Haematite 2%, goethite 9%

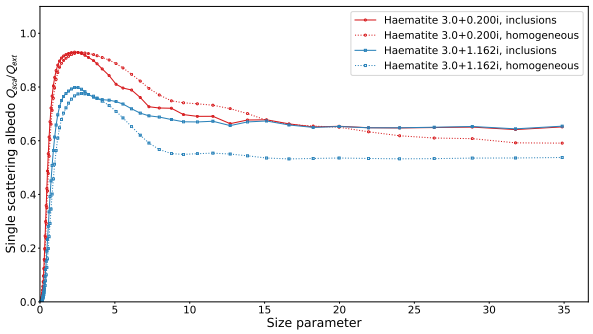

(f) Haematite 6%, goethite 9%

Figure B.10: Single scattering albedo comparison for shape F. Shown is the single scattering albedo for a range of size parameters. The colours indicate the refractive index of haematite (red: $3.0 + 0.2i$, blue: $3.0 + 1.162i$), corresponding to different wavelengths, while the line style indicates the mixture strategy: Inhomogeneous mixture (inclusions of one percent volume spheres each) are shown as solid lines, the homogeneous mixtures shown as dotted lines. Shown are six different mixture ratios (a) – (f) of haematite and goethite by volume.

B.3. Absorption efficiency

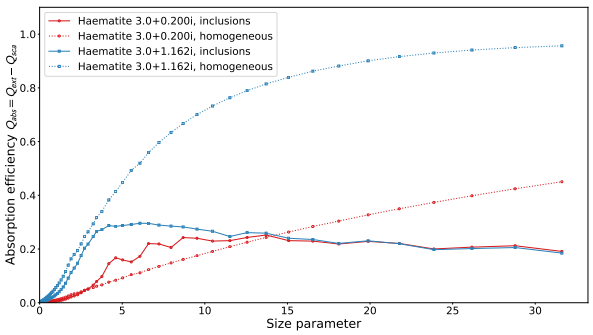

(a) Haematite 2%, goethite 0%

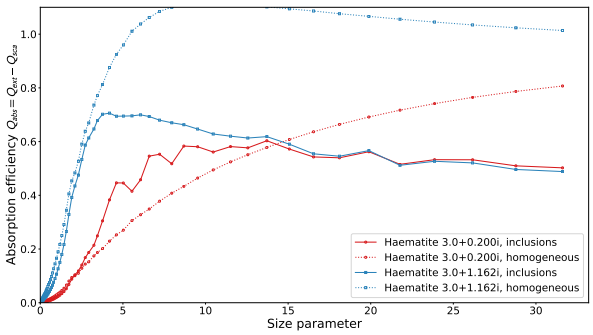

(b) Haematite 6%, goethite 0%

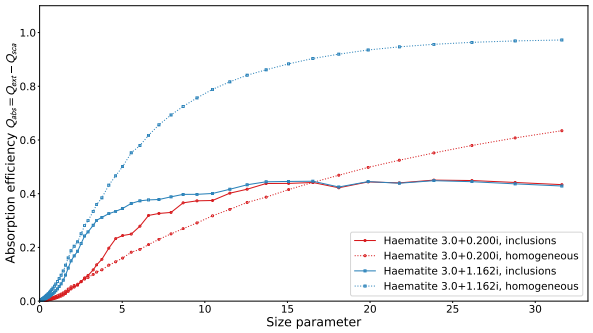

(c) Haematite 2%, goethite 3%

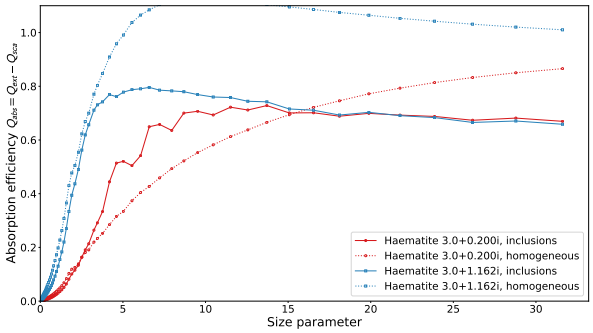

(d) Haematite 6%, goethite 3%

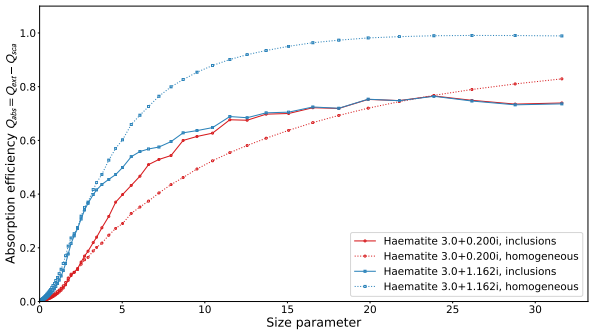

(e) Haematite 2%, goethite 9%

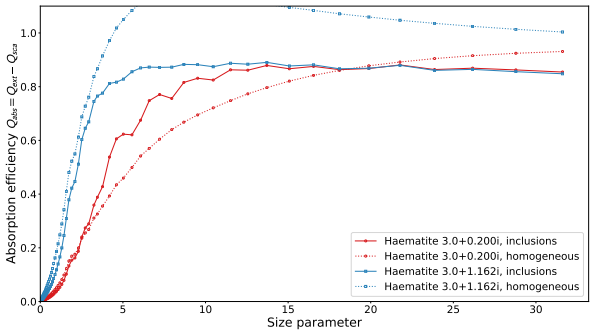

(f) Haematite 6%, goethite 9%

Figure B.11: Absorption efficiency comparison for shape A. Shown is the absorption efficiency for a range of size parameters. The colours indicate the refractive index of haematite (red: $3.0 + 0.2i$, blue: $3.0 + 1.162i$), corresponding to different wavelengths, while the line style indicates the mixture strategy: Inhomogeneous mixture (inclusions of one percent volume spheres each) are shown as solid lines, the homogeneous mixtures shown as dotted lines. Shown are six different mixture ratios (a) – (f) of haematite and goethite by volume.

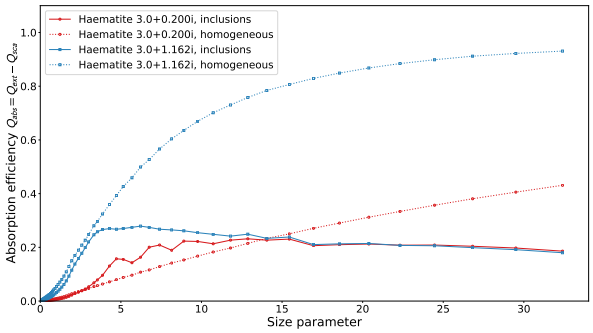

(a) Haematite 2%, goethite 0%

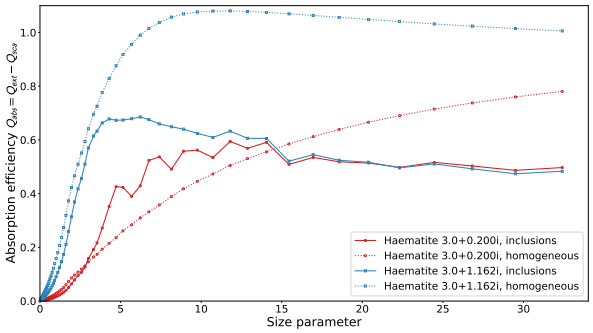

(b) Haematite 6%, goethite 0%

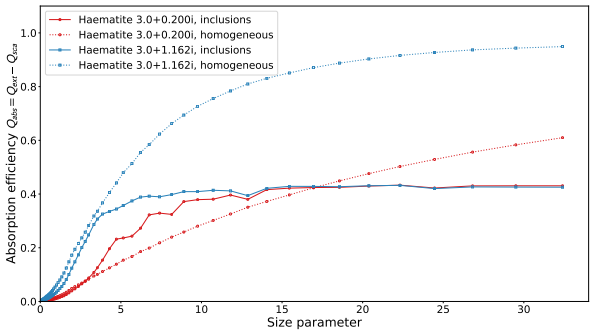

(c) Haematite 2%, goethite 3%

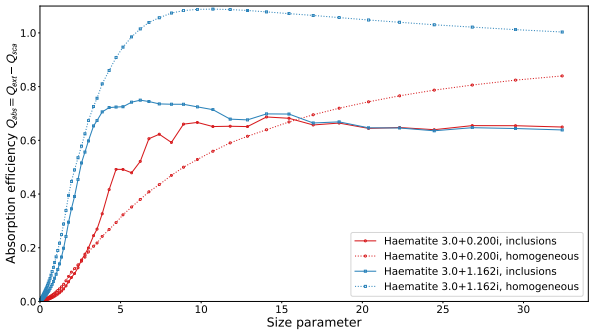

(d) Haematite 6%, goethite 3%

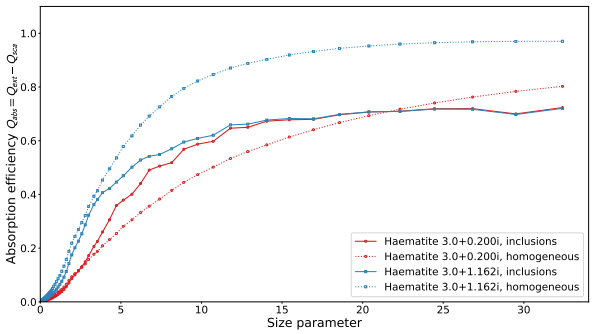

(e) Haematite 2%, goethite 9%

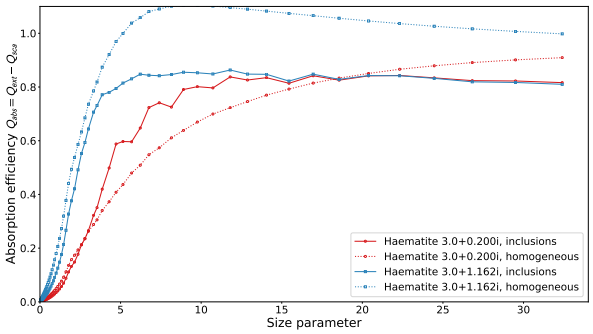

(f) Haematite 6%, goethite 9%

Figure B.12: Absorption efficiency comparison for shape B. Shown is the absorption efficiency for a range of size parameters. The colours indicate the refractive index of haematite (red: $3.0 + 0.2i$, blue: $3.0 + 1.162i$), corresponding to different wavelengths, while the line style indicates the mixture strategy: Inhomogeneous mixture (inclusions of one percent volume spheres each) are shown as solid lines, the homogeneous mixtures shown as dotted lines. Shown are six different mixture ratios (a) – (f) of haematite and goethite by volume.

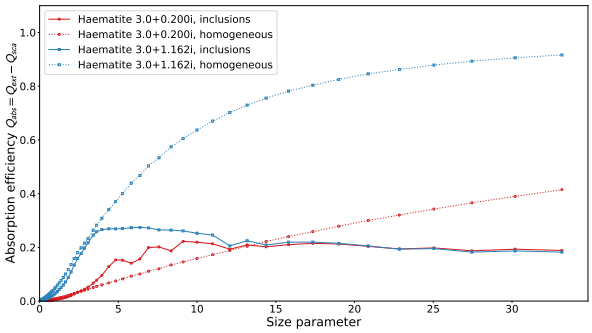

(a) Haematite 2%, goethite 0%

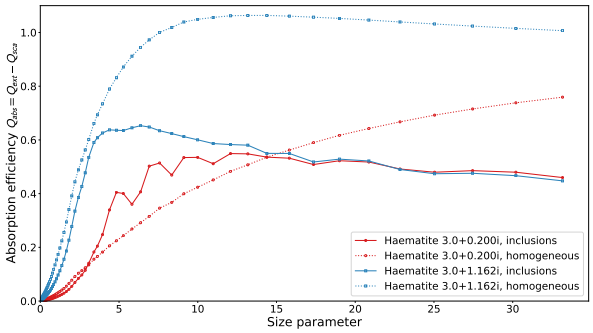

(b) Haematite 6%, goethite 0%

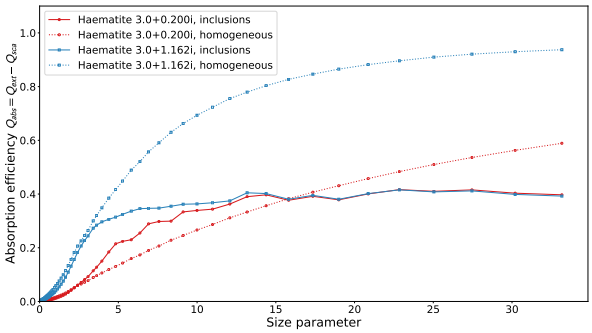

(c) Haematite 2%, goethite 3%

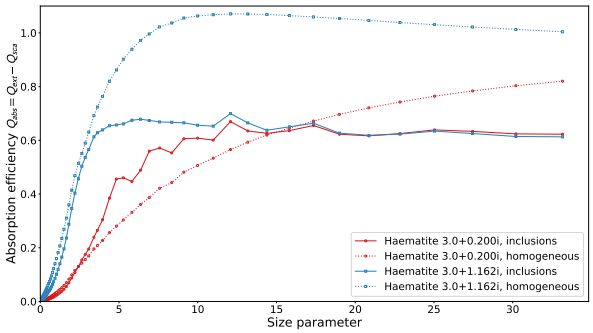

(d) Haematite 6%, goethite 3%

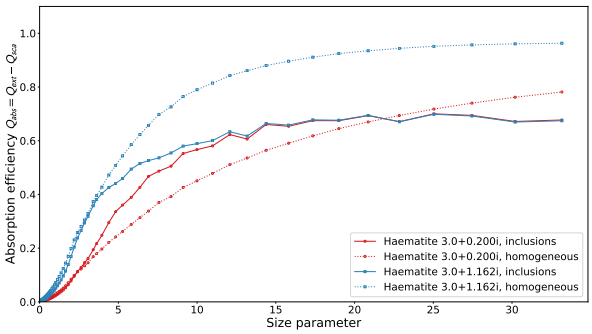

(e) Haematite 2%, goethite 9%

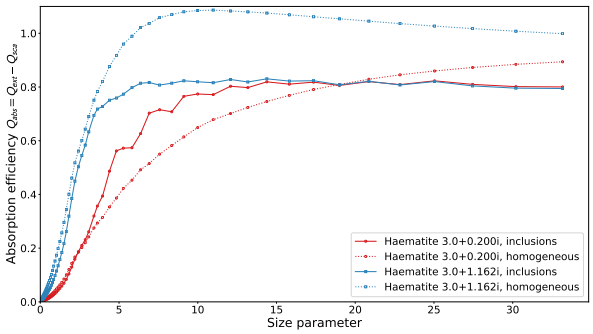

(f) Haematite 6%, goethite 9%

Figure B.13: Absorption efficiency comparison for shape C. Shown is the absorption efficiency for a range of size parameters. The colours indicate the refractive index of haematite (red: $3.0 + 0.2i$, blue: $3.0 + 1.162i$), corresponding to different wavelengths, while the line style indicates the mixture strategy: Inhomogeneous mixture (inclusions of one percent volume spheres each) are shown as solid lines, the homogeneous mixtures shown as dotted lines. Shown are six different mixture ratios (a) – (f) of haematite and goethite by volume.

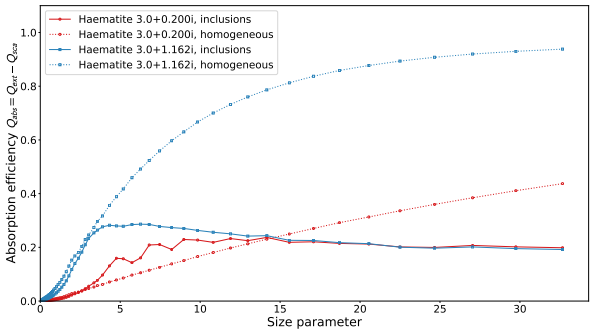

(a) Haematite 2%, goethite 0%

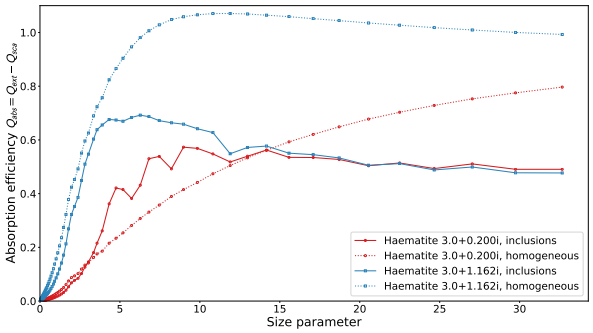

(b) Haematite 6%, goethite 0%

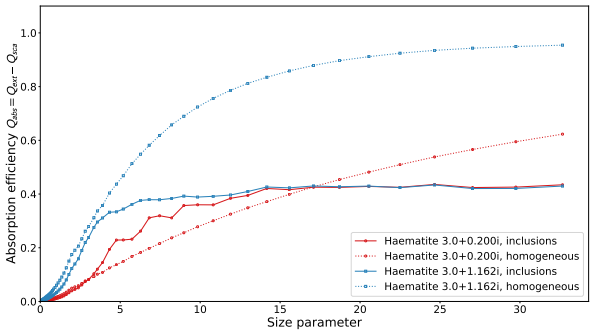

(c) Haematite 2%, goethite 3%

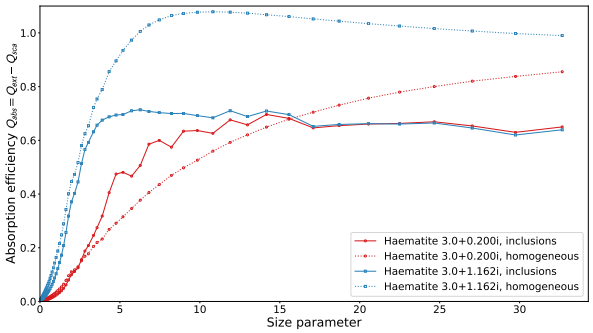

(d) Haematite 6%, goethite 3%

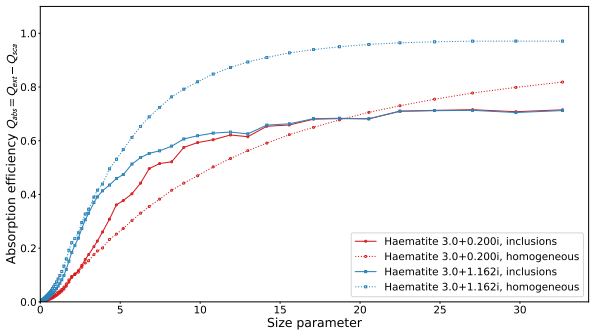

(e) Haematite 2%, goethite 9%

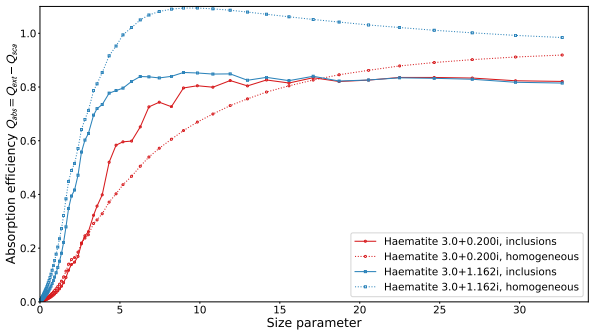

(f) Haematite 6%, goethite 9%

Figure B.14: Absorption efficiency comparison for shape E. Shown is the absorption efficiency for a range of size parameters. The colours indicate the refractive index of haematite (red: $3.0 + 0.2i$, blue: $3.0 + 1.162i$), corresponding to different wavelengths, while the line style indicates the mixture strategy: Inhomogeneous mixture (inclusions of one percent volume spheres each) are shown as solid lines, the homogeneous mixtures shown as dotted lines. Shown are six different mixture ratios (a) – (f) of haematite and goethite by volume.

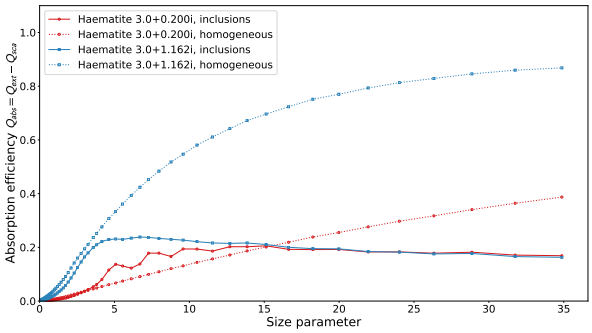

(a) Haematite 2%, goethite 0%

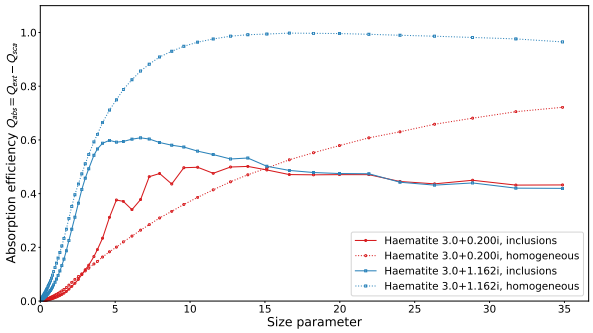

(b) Haematite 6%, goethite 0%

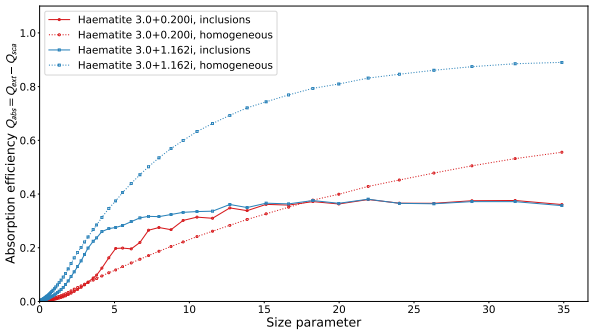

(c) Haematite 2%, goethite 3%

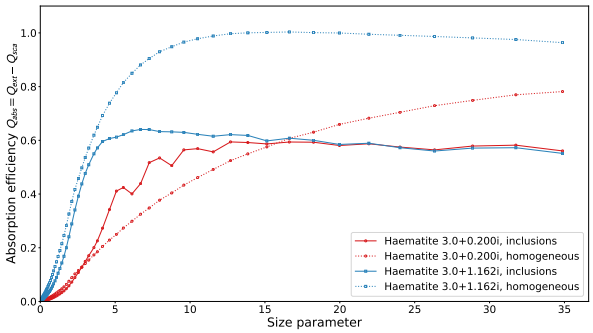

(d) Haematite 6%, goethite 3%

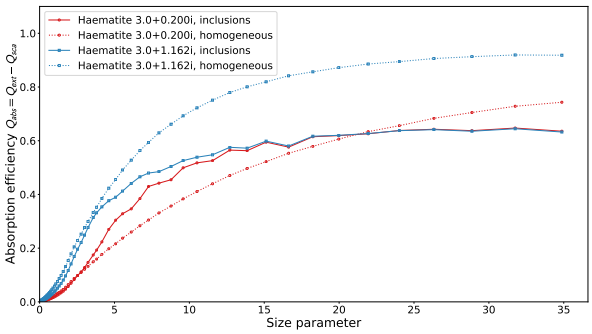

(e) Haematite 2%, goethite 9%

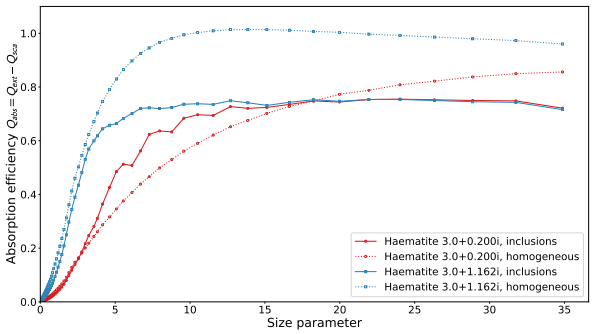

(f) Haematite 6%, goethite 9%

Figure B.15: Absorption efficiency comparison for shape F. Shown is the absorption efficiency for a range of size parameters. The colours indicate the refractive index of haematite (red: $3.0 + 0.2i$, blue: $3.0 + 1.162i$), corresponding to different wavelengths, while the line style indicates the mixture strategy: Inhomogeneous mixture (inclusions of one percent volume spheres each) are shown as solid lines, the homogeneous mixtures shown as dotted lines. Shown are six different mixture ratios (a) – (f) of haematite and goethite by volume.

B.4. Asymmetry factor

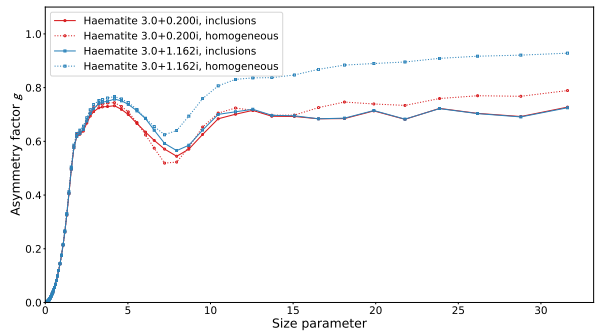

(a) Haematite 2%, goethite 0%

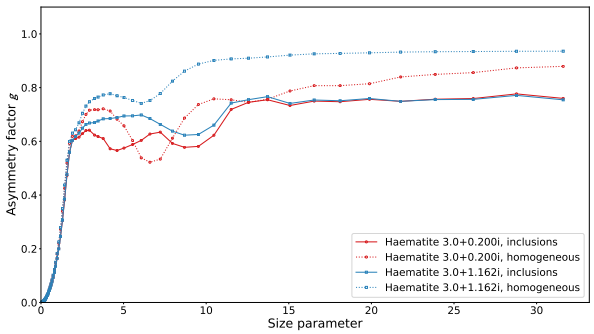

(b) Haematite 6%, goethite 0%

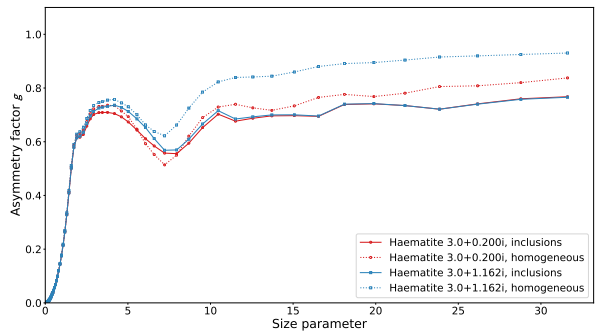

(c) Haematite 2%, goethite 3%

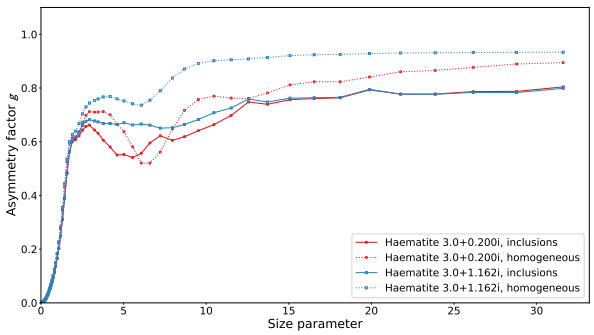

(d) Haematite 6%, goethite 3%

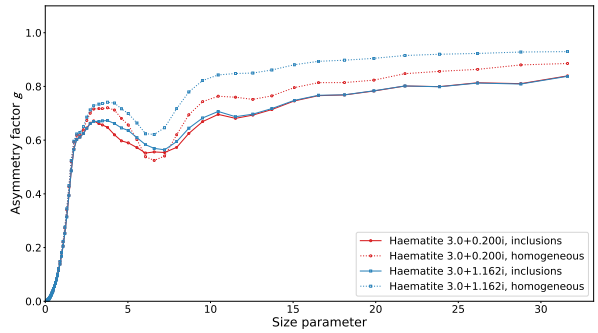

(e) Haematite 2%, goethite 9%

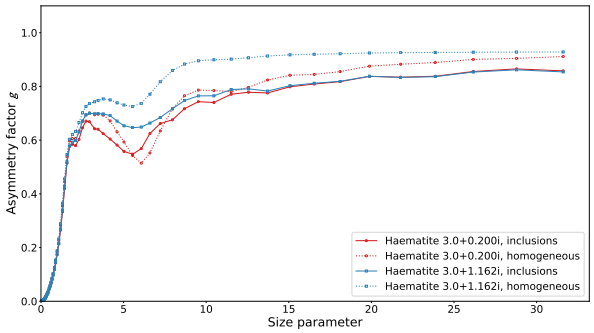

(f) Haematite 6%, goethite 9%

Figure B.16: Asymmetry factor comparison for shape A. Shown is the asymmetry factor for a range of size parameters. The colours indicate the refractive index of haematite (red: $3.0+0.2i$, blue: $3.0+1.162i$), corresponding to different wavelengths, while the line style indicates the mixture strategy: Inhomogeneous mixture (inclusions of one percent volume spheres each) are shown as solid lines, the homogeneous mixtures shown as dotted lines. Shown are six different mixture ratios (a) – (f) of haematite and goethite by volume.

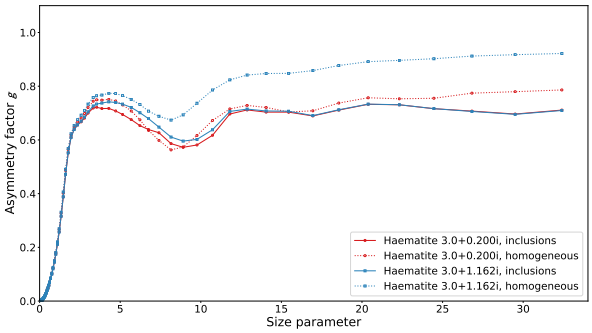

(a) Haematite 2%, goethite 0%

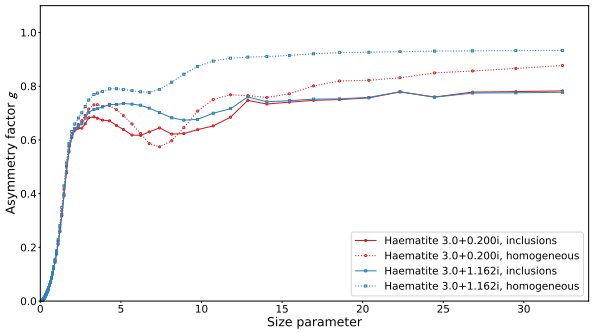

(b) Haematite 6%, goethite 0%

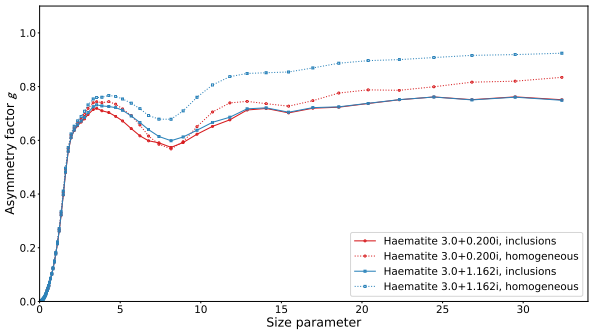

(c) Haematite 2%, goethite 3%

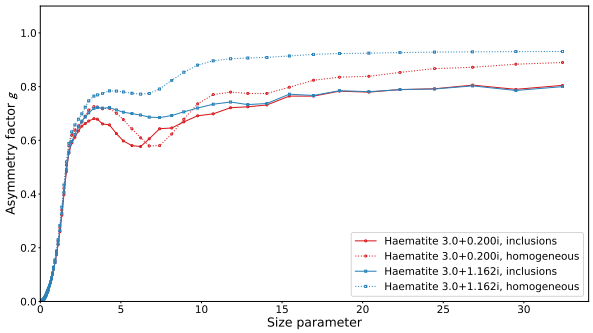

(d) Haematite 6%, goethite 3%

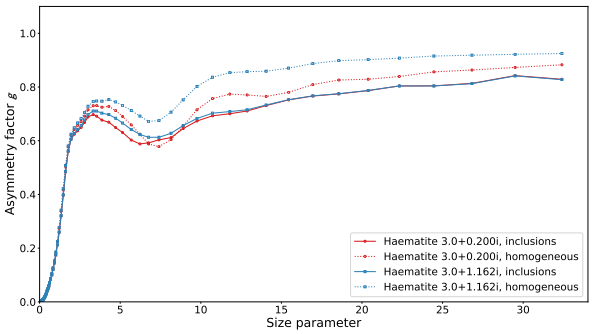

(e) Haematite 2%, goethite 9%

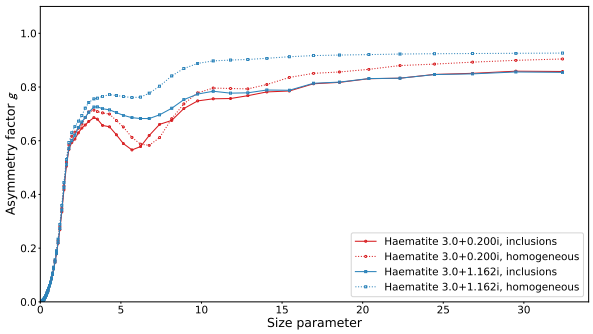

(f) Haematite 6%, goethite 9%

Figure B.17: Asymmetry factor comparison for shape B. Shown is the asymmetry factor for a range of size parameters. The colours indicate the refractive index of haematite (red: $3.0+0.2i$, blue: $3.0+1.162i$), corresponding to different wavelengths, while the line style indicates the mixture strategy: Inhomogeneous mixture (inclusions of one percent volume spheres each) are shown as solid lines, the homogeneous mixtures shown as dotted lines. Shown are six different mixture ratios (a) – (f) of haematite and goethite by volume.

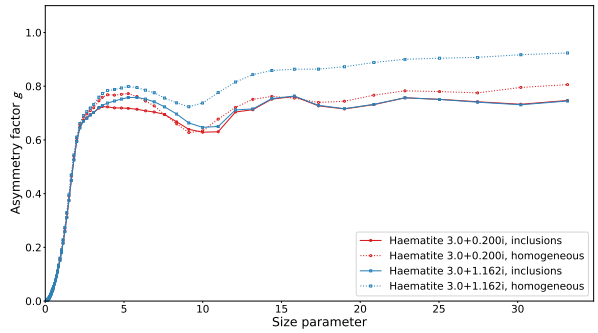

(a) Haematite 2%, goethite 0%

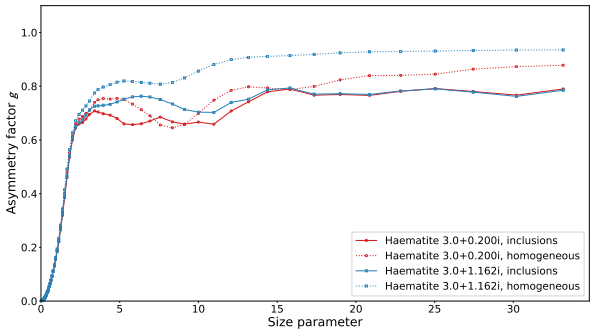

(b) Haematite 6%, goethite 0%

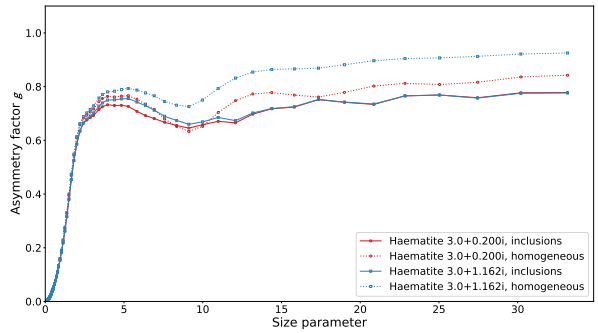

(c) Haematite 2%, goethite 3%

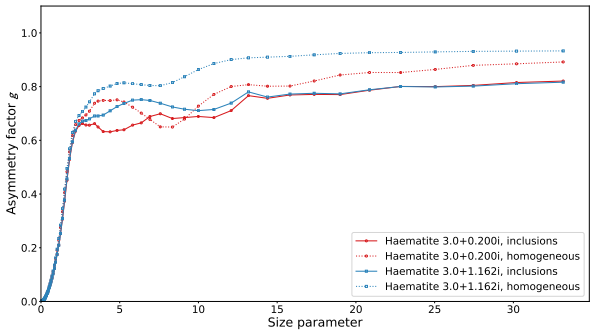

(d) Haematite 6%, goethite 3%

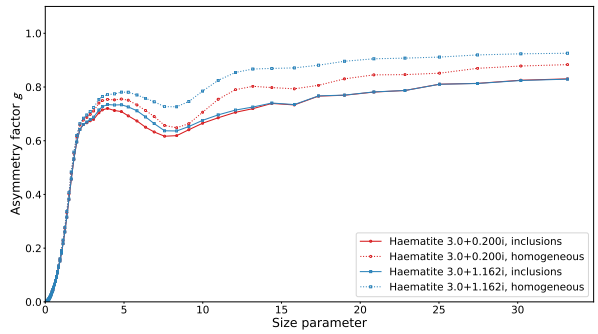

(e) Haematite 2%, goethite 9%

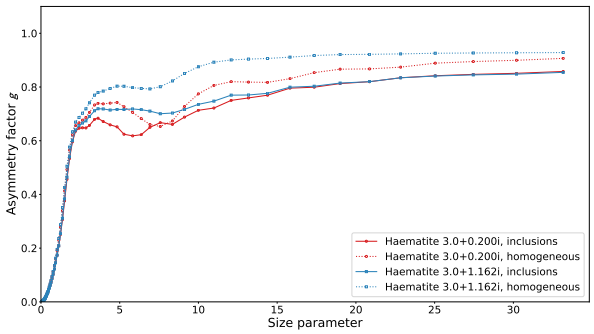

(f) Haematite 6%, goethite 9%

Figure B.18: Asymmetry factor comparison for shape C. Shown is the asymmetry factor for a range of size parameters. The colours indicate the refractive index of haematite (red: $3.0+0.2i$, blue: $3.0+1.162i$), corresponding to different wavelengths, while the line style indicates the mixture strategy: Inhomogeneous mixture (inclusions of one percent volume spheres each) are shown as solid lines, the homogeneous mixtures shown as dotted lines. Shown are six different mixture ratios (a) – (f) of haematite and goethite by volume.

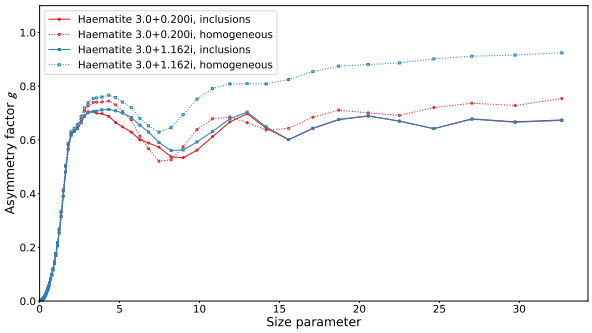

(a) Haematite 2%, goethite 0%

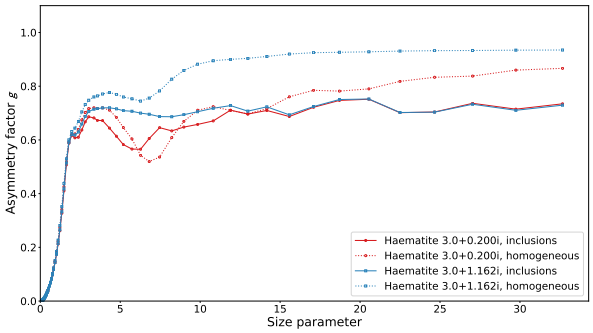

(b) Haematite 6%, goethite 0%

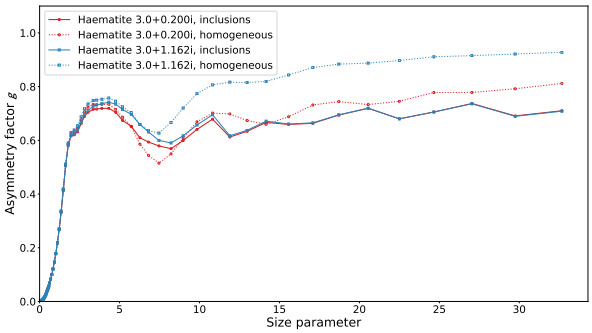

(c) Haematite 2%, goethite 3%

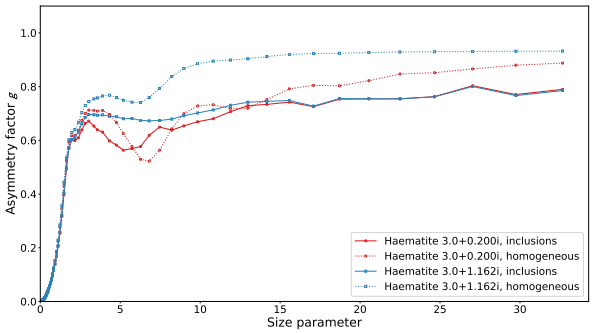

(d) Haematite 6%, goethite 3%

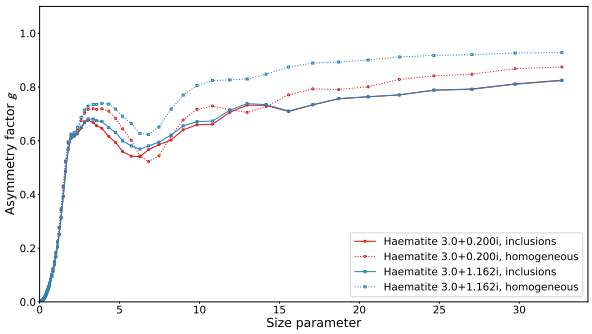

(e) Haematite 2%, goethite 9%

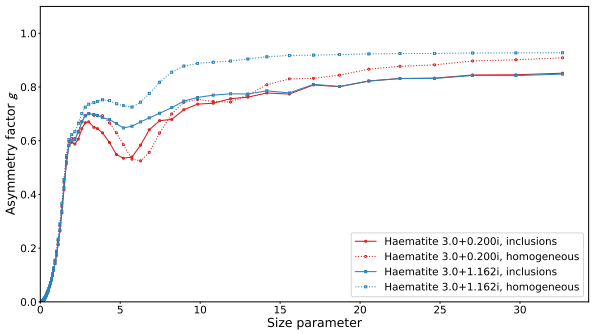

(f) Haematite 6%, goethite 9%

Figure B.19: Asymmetry factor comparison for shape E. Shown is the asymmetry factor for a range of size parameters. The colours indicate the refractive index of haematite (red: $3.0+0.2i$, blue: $3.0+1.162i$), corresponding to different wavelengths, while the line style indicates the mixture strategy: Inhomogeneous mixture (inclusions of one percent volume spheres each) are shown as solid lines, the homogeneous mixtures shown as dotted lines. Shown are six different mixture ratios (a) – (f) of haematite and goethite by volume.

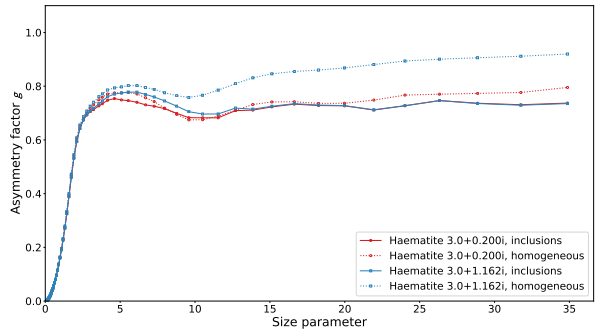

(a) Haematite 2%, goethite 0%

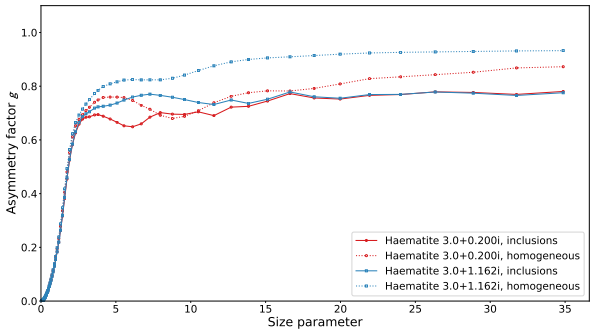

(b) Haematite 6%, goethite 0%

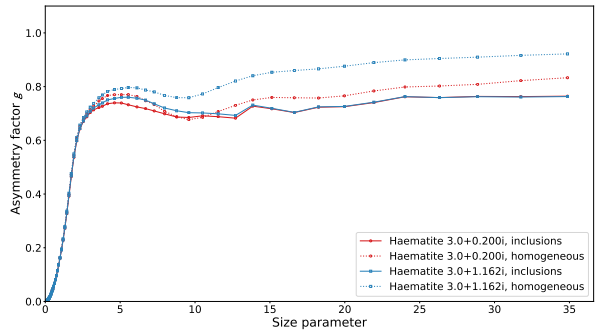

(c) Haematite 2%, goethite 3%

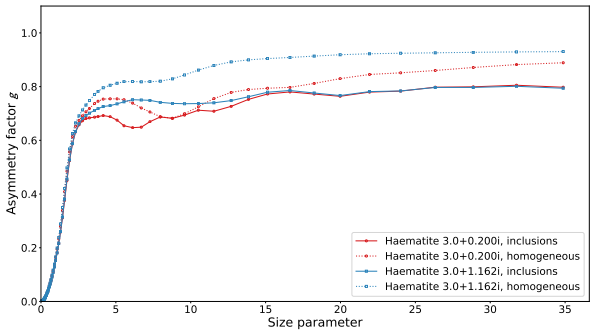

(d) Haematite 6%, goethite 3%

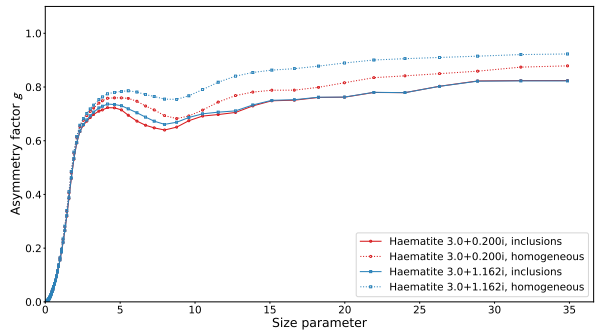

(e) Haematite 2%, goethite 9%

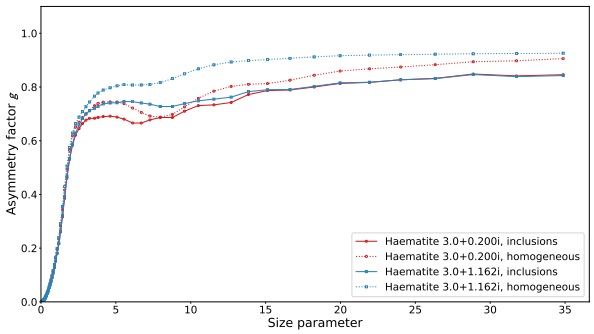

(f) Haematite 6%, goethite 9%

Figure B.20: Asymmetry factor comparison for shape F. Shown is the asymmetry factor for a range of size parameters. The colours indicate the refractive index of haematite (red: $3.0+0.2i$, blue: $3.0+1.162i$), corresponding to different wavelengths, while the line style indicates the mixture strategy: Inhomogeneous mixture (inclusions of one percent volume spheres each) are shown as solid lines, the homogeneous mixtures shown as dotted lines. Shown are six different mixture ratios (a) – (f) of haematite and goethite by volume.